PLASTIC DEFORMATION AND FRACTURE BEHAVIOR OF AL-MG AND AL-CR ALLOYS

PLASTIC DEFORMATION AND FRACTURE BEHAVIOR OF AL-MG AND AL-CR ALLOYS

By

MIKE JOBBA, B. ENG & MGMT

A Masters Thesis
Submitted to the McMaster School of Graduate Studies
in Partial Fulfilment of the Requirements
for the Degree
Masters of Applied Science

McMaster University

Masters of Applied Science (2010)
Department of Materials Science and Engineering

McMaster University
Hamilton, Ontario

TITLE: Plastic Deformation and Fracture Behavior of Al-Mg and Al-Cr Alloys

AUTHOR: Mike Jobba, M.A.Sc, B.Eng. & Mgmt.
SUPERVISOR: M. Niewczas
NUMBER OF PAGES: xviii, 176

ABSTRACT

This research concerns a study of the deformation behavior and dislocation substructure characteristics resulting from plastic flow in single phase Al-Mg (0-4.11at%Mg) and Al-Cr (0-0.36at%Cr) alloys. Tensile tests are performed at 298K, 78K, and 4.2K, and strain rate sensitivity tests are performed at 78K for the Al-Mg alloys, and at 298K and 78K for the Al-Cr alloys. Resistivity measurements are carried out during tensile tests for all alloys deformed at 4.2K. The resulting structures are then studied using SEM and TEM microscopy. Solute strengthening is seen to occur in both systems, along with significant increases in strength and work hardening capacity in all alloys accompanying decreases in temperature. The limit for benefits from solute strengthening appears to lie close to the solubility limit for the Al-Mg system, but no clear limit is observed in the Al-Cr system. Resistivity data seems to indicate that a critical dislocation density is reached before fracture in all Al-Mg alloys studied, but that this critical density decreases with Cr content. Portevin Le-Chatelier (PLC) type instabilities are observed at room temperature in the Al-Mg alloys only, though both systems exhibit adiabatic shearing processes at 4.2K. A dislocation substructure resembling those observed in other Al-Mg alloys is observed, but the Al-Cr alloy dislocation substructure more closely resembles that observed in pure Al. Both substructures are seen to show greater dislocation density, distributed more homogenously over the structure as temperature decreases.

ACKNOWLEDGEMENTS

The author wishes to extend his thanks to his supervisor, Dr. Marek Niewczas, for his guidance and help throughout this study. Additionally, he wishes to thank the Natural Sciences and Engineering Research Council of Canada (NSERC) for their Collaborative Research Grant with GM, which has provided the funding for this research. He would also like to thank his predecessor, Dr. Dong-Yeob Park, for his help during the initial stages of the project, and for his previous work on the subject. Special thanks are also given to Doug Culley, Steve Koprich, Fred Pearson, and Andy Duft for their technical help, and to the many others whose contributions helped make this project possible.

TABLE OF CONTENTS

LIST OF FIGURES

LIST OF TABLES

1 INTRODUCTION

1.1 MOTIVATION

The replacement of steel parts with aluminum equivalents is a growing area of interest in the automotive industry, driven mainly by demand (both from governmental and public sources) for higher-mileage vehicles. This demand makes aluminum, a light material with useful properties in terms of formability, recyclability, and corrosion resistance, an attractive choice for new designs. The use of aluminum in automotive applications has grown for decades, such that in the average automobile the mass of Al used increased from 36.7kg to 145.14kg between the years 1973 and 2007.[1] However, for further replacements to be possible, aluminum alloys with superior properties such as higher tensile strength (~250-950 MPa) must be developed while remaining cost effective.[2]

The 5000 and 6000 series of Al-Mg alloys are currently some of the most popular in terms of use in Automotive body paneling, but a number of material limitations still exist that limit the applicability of the alloys[3]. Thus, additional research is required in order to develop new alloys that can surpass these limitations.

1.2 THE EFFECTS OF MG ON THE AL SYSTEM

Magnesium (Mg) is one of the more common substitutional alloying agents used in Al (and vice versa) for solute strengthening due to their excellent solubility in each other. Furthermore, the addition of Mg to Al alloys hardens the alloy and increases its ductility, due to solid solution hardening.[4] The increases in dislocation pinning during deformation through the addition of Mg are well-established, as is the resulting unstable dislocation motion (serrated flow) characteristic of deformation in Al-Mg alloys.[5] Higher Mg content alloys have been observed to be more likely to exhibit similar plastic instability, such as the PLC effect, and this instability has been observed to increase with Mg content, while being absent in dilute alloys.[6] Increases in work hardening rates accompany additions of Mg to the Al system, and in the case of higher concentrations of Mg, solute drag can disproportionately affect the work hardening characteristics when compared to the effects of solute strengthening.[7] Increases in Mg content can also raise the flow stress experienced by the material during deformation, although the level of increase is highly dependant on strain rate, as well as Mg content.[8] Strain rate sensitivity, however, appears to be relatively unaffected by Mg content above levels of around 2.8at%Mg.[9]

The lowering of stacking fault energy that results due to the introduction of Mg atoms as solutes in the Al network affects the formation of the dislocation substructure during deformation. The addition of Mg causes a noticeable reduction in dynamic recovery for the alloy and facilitates dynamic recrystallization. Cross-slip and climb during deformation are more difficult in the presence of solute atoms, a phenomenon used to explain the reduction in dynamic recovery.[10] In cases where the concentration of Mg is sufficient, Mg addition can also create a more dramatic solute drag effect, which increases with Mg content.

Al-Mg alloys respond slower to age hardening than other more common age-hardenable Al alloys, even at Mg levels far beyond the solubility limit. This response is attributed to a G.P. zone solvus temperature, which is lower than room temperature at these compositions.[11]

1.3 THE EFFECTS OF CR ON THE AL SYSTEM

The thermal stability of the mechanical properties of Al alloys is poor, due to the sensitivity of processes such as grain growth and phase transformation, a sensitivity which rises with temperature. Chromium (Cr) is most commonly used as an additive, along with other transition metals, to stabilize microstructure and mechanical properties at higher temperatures. The formation of Cr-rich particles can retard grain growth and recrystallization, resulting in finer microstructure at higher temperatures, especially as the Cr-intermetallic spheroids do not coarsen during annealing, and do not dissolve into solution due to the low solubility and diffusion coefficient of Cr in Al compared to other alloying elements.[12] The maximum concentration of Cr in Al is limited, however, by the formation of brittle intermetallic phases, which have detrimental effects the mechanical properties the addition of Cr is supposed to improve.[13]

The formation of these insoluble Cr precipitates is highly dependant on quenching conditions, and can have an embrittling effect on the aging behavior of the alloy. Precipitates located close to the grain boundaries can accelerate crack propagation, leading to intergranular branching close to the free surface, and coarser intermetallics can become a dominant factor in the overall fracture toughness. Even trace amounts of Cr can retard G.P. zone formation during quenching, likely due at least in part to the preference of Cr atoms to combine with vacancies.[14] The addition of further elements such as silicon and zirconium, however, can mitigate the quench sensitivity of the alloy and stabilize the sub-grain structure.[15]

The addition of Cr has also been observed to decrease the amplitude of the recovery stage in the 40-80K temperature range, in effect hindering the recombination of interstitials during irradiation.[16] This indicates that the addition of Cr may have the effect of decreasing defect mobility, especially if temperature is decreased, and that this trapping ability increases with Cr content, at least in dilute alloys.

As with the Al-Mg system, Cr in solution in the Al system will raise the flow stress during strain, but unlike the Al-Mg system, it appears this increase in flow stress is independent of strain rate, and additions of Cr to Al-Mg alloys appear to mitigate the influence of strain rate on the flow stresses experienced in the Al-Mg alloys.[17]

1.4 THE PORTEVIN-LeCHATELIER EFFECT

The Portevin Le-Chatelier Effect (PLC Effect) is a form of plastic instability caused by rapid localized plasticity in a sample undergoing constant tensile strain or a consistently rising external stress. Most explanations of the phenomenon describe the PLC Effect as a macroscopic manifestation of dynamic strain aging (DSA), where the sudden breakaway of dislocations pinned by solutes that have diffused into the strain field once sufficient force is available to overcome the strength of the obstacles. Solute atoms are driven to cluster close to the dislocations by interactions with the strain field, which leads to an increasing resistance to further dislocation in the lattice so long as neighbouring solute atoms have sufficient mobility. Clustering can be accelerated by substructural obstacles including grain boundaries, precipitates or forest dislocations, which can arrest dislocation flow for sufficient time for clustering to occur. Thus, high strain rates or similar situations where dislocation arrest time is short are unlikely to exhibit PLC effect behavior. The localized nature of the strains in the PLC effect is thought to be due to a negative strain rate sensitivity (SRS), which itself is caused by DSA. In samples with mobile solutes, the transient strain rate sensitivity is always negative and dependent on solute mobility. Only in samples where the overall strain rate sensitivity is negative (due to a strongly negative transient strain rate sensitivity) are PLC Effects observed.[18] PLC Effects are often characterized by sudden load drops during deformation as well as the formation of narrow deformation bands on the surface of the sample and an audible acoustic emission during each load drop.[19] The PLC Effect, however, only occurs within a certain range of temperature for each alloy, due to differences in activation energy of the process and the effect of the interplay between solute and dislocation mobility in the substructure.

PLC Effects can be denoted by three differing types, A, B, and C. Types A & B are differentiated by type A being a continuously propagating phenomenon, usually observed under a high strain rate during the first stages of deformation, while type B bands propagate more intermittently, usually at lower strain rates and stages of high deformation. Furthermore, type A bands are usually observed to nucleate around areas of stress concentration such as near grips or similar geometric concentrators, while type B bands normally build near a previously active band in an area of un-aged dislocation. Type B bands also propagate with a much smaller average velocity than type A bands due to their intermittent nature, though a single type B band can evolve to saturation in a much shorter time than a type A band, and can grow along the full width of the sample. As a result, type B bands are more efficient in terms of dynamic strain aging. [20] Type C bands are usually observed only at very low strain rates, and are signified by stress drops below the stress-strain curve's undisturbed values. As the strain rate increases, type C bands are less likely to be observed, while type A&B bands become more likely to occur, and can sometimes both be observed at the same strain rate.[21]

1.5 PREVIOUS WORK

Starink & Wang describe the yield strength of a material as being derived from numerous contributions, using the following formula:

$$\sigma_y = \Delta\sigma_{gb} + M\,(\,\Delta\tau_0 + \Delta\tau_{ss} + (\Delta\tau_D{}^2 + \Delta\tau_{ppt}{}^2)^{1/2}) \qquad (1)$$

where σ_y represents the yield strength, $\Delta\sigma_{gb}$ represents the strength contribution due to grain boundaries, M is an orientation factor (specficially, the Taylor factor), $\Delta\tau_0$ represents the intrinsic lattice strength of the material, $\Delta\tau_{ss}$ represents the overall solute strengthening contributions (expressed as the sum of the strengthening due to each individual element relative to their concentration), $\Delta\tau_D$ represents the strengthening in the lattice due to dislocations, and $\Delta\tau_{ppt}$ represents the strengthening due to the contribution of precipitates.[22] Thus, to focus on the effects of solute strengthening, the other contributions must be controlled as much as possible, through a consistent grain size in undeformed (or otherwise dislocation-free) samples, and through compositions that remain in or close to the single phase region.

Although there has already been substantial research focused on Al-Mg alloys, the overwhelming majority has been limited to commercial alloys, rather than the binary Al-Mg system with no other major alloying elements. Furthermore, this research is usually done at room temperature or at elevated temperatures, which makes it difficult to focus on aspects of mechanical behavior such as solute strengthening. At low temperatures, the contributions to strength from the solutes alone are more easily discernable, as many thermally activated processes are suppressed.

In a study of commercial Al-Mg alloys by Park[23], tensile tests were performed in order to study the mechanical behavior of these alloys at temperatures as low as 4.2K. Insight was made into the flow instabilities that occur in such alloys, as well as the temperatures at which they were prevalent. The study also determined the plastic deformation of pure Al was governed by dislocation-dislocation interactions. In addition to direct load/stress measurement, the study also utilized resistivity measurements as a way of relating dislocation density to flow stress during deformation, determining the remarkably high work hardening capacity for the commercial alloys observed at low temperature was due to the kinetics of dislocation storage and recovery, which differ between the different compositions studied.

TEM analyses in the same study by Park[24], as well as the previous work of others on deformed Al-Mg alloys have observed a cellular dislocation structure with planar channels, with high dislocation densities along the walls of the cells. The form of this structure seems to be consistent as alloying content is increased, and the resulting dislocation substructures of differing alloys become even more consistent compared to each other as deformation increases.[25]

Additional areas of focus for studies into the Al-Mg system have included the instabilities observed during deformation, and their relationship to strain rate sensitivity[26], and phase compositions and texturing resulting from deformation[27] [28] or heat treatment[29].

Chromium, however, has been the focus of much less testing in terms of solute strengthening in Al, due to its low solubility in Al and the difficulty of annealing out precipitates. Most research in the area has focused on the use of additional additives, such as Zr, to increase the amount of Cr kept in solution.[30] Other than attempts to increase solubility, significant research into Al-Cr has focused on the characterization of intermetallic precipitates, and the behavior of these precipitates under stress and changes in thermal conditions, in order to assess their effectiveness as thermal stabilizers in the Al system. This has been accomplished mainly through optical and electron microscopy, with a few studies utilizing mechanical testing.

Dislocation density studies on Al-Cr alloys through measurements of resistivity have been carried out before, though the dislocations were introduced through irradiation, rather than physical deformation. Still, the process verifies that changes in resistivity correspond to increases in dislocation/defect density in the Al-Cr system, and that these changes are only accurately observable in the low temperature range.[31]

Saimoto and Diak have argued that the final formability of face-centred cubic (fcc) alloys, such as Al-Cr alloys, is affected by their work hardening processes, and more specifically, by the efficiency of dynamic recovery of dislocation debris during deformation. It has been suggested that dislocation debris can enhance the ductility of an alloy through the higher resistance of debris to dynamic recovery. Similarly, they found that both dynamic recovery and dynamic recrystallization are suppressed by increased presence of alloying elements to the solid solution.[32]

Studies by Bull and Saimoto have shown that the defects contributing to the increased strain rate sensitivity of the material can also be attributed to dislocation debris, and are in fact recoverable. These defects anneal from the structure at about 225 K for pure Al compared to about 350 K for the Al-Cr alloy in their study. The dislocation debris in question was found to include dislocation loops in Al and stacking fault tetrahedra (SFT) in an Al-Cr alloy.[33] It has been argued that in Al-Cr alloys with lower stacking fault energy, three-dimensional

SFT's should be responsible for the increased resistance to dynamic recovery, preventing the movement of dislocations past these defects and eventually softening the material. In the case of pure Al, the material develops planar dislocation loops, which are relatively weak obstacles to dislocation motion, and as a result the pure Al is susceptible to dynamic recovery, resulting in more softening and fracture due to localized deformation. Precision strain rate sensitivity measurements carried out on Cr-rich AA6063 alloys showed that the addition of Cr reduced the stacking fault energy and enhanced the formability of the alloy.[34] The dislocation debris produced in this system during the deformation is more resistant to recovery below 110 °C than debris produced in comparable pure Al or Al-Mg alloys, and the resistance to dynamic recovery of this debris is directly responsible for enhanced ductility of the AA6063 alloy at room temperature. Unfortunately, no other results are available to confirm these findings, either in terms of mechanical properties relating to the relationship between ductility of the material, or regarding the nature of the dislocation debris produced during plastic flow.

As a result, additional systematic studies of deformation behaviour of binary or ternary Al-alloys with different mixtures of alloying elements, combined with TEM studies of the subsequent dislocation substructure will produce useful results to contribute to the fundamental understanding of the influence of various microstructural elements on the formability and limits of plasticity in Al-based systems.

2 METHODOLOGY

2.1 SAMPLE PREPARATION

The Al-Mg samples were cast by dissolving the magnesium (from 99.999% pure pellets) into the aluminum (from 99.999% pure pellets) inside of a graphite crucible using an induction furnace. In the case of the Al-Cr alloys, a vacuum electric arc furnace was used to first create master alloys of Al and Cr (from 99.999% pure granules), which were then combined with additional aluminum in a graphite crucible using an induction furnace, as with the Al-Mg alloys. A high purity (99.9999% pure) aluminum was used for the pure Al samples.

With all alloys, the resulting melt was poured into a brass ingot mold, where they were allowed to solidify, after which the entire mold was placed in a bucket of ice water to quench/cool. The resulting ingots were homogenized in a small furnace for 24 hours at 620°C to remove any concentration gradients or grain size inconsistencies formed during casting. After removal from the furnace, samples were cut from the ingots for Inductive Coupled Plasma (ICP) spectrometry testing, to verify the resulting alloy was of the desired composition. The resulting concentrations of solute in each alloy are given in Table 1.

Table 1: Alloy Compositions

Designation	Solute	Solute Concentration (wt%)	Solute Concentration (at%)
AL	N/A	0%	0%
AM1	Mg	0.45%	0.5%
AM2	Mg	0.97%	1.08%
AM3	Mg	1.88%	2.08%
AM4	Mg	2.81%	3.11%
AM5	Mg	3.72%	4.11%
AC1	Cr	0.35%	0.18%
AC2	Cr	0.09%	0.05%
AC3	Cr	0.16%	0.08%
AC4	Cr	0.70%	0.36%

Once their compositions were verified, the ingots were rolled out to a thickness of around 3.5 mm. The rolled sheets were then machined into a series of tensile samples, with the rolling direction parallel to the direction in which the tensile force would be applied.

After receiving the machined samples, an annealing process was applied to relieve residual stresses in the samples from the rolling/machining process, as well as to produce a homogenized microstructure. For the Al-Mg samples, an annealing study was already completed by previous graduate student Dong Park, and the temperatures required to reach a fully-crystallized, consistent grain size at each solute level were already known. These are given below in Table 2. For each alloy, the annealing time was 10 minutes, and the resulting grain size was 38-40μm.

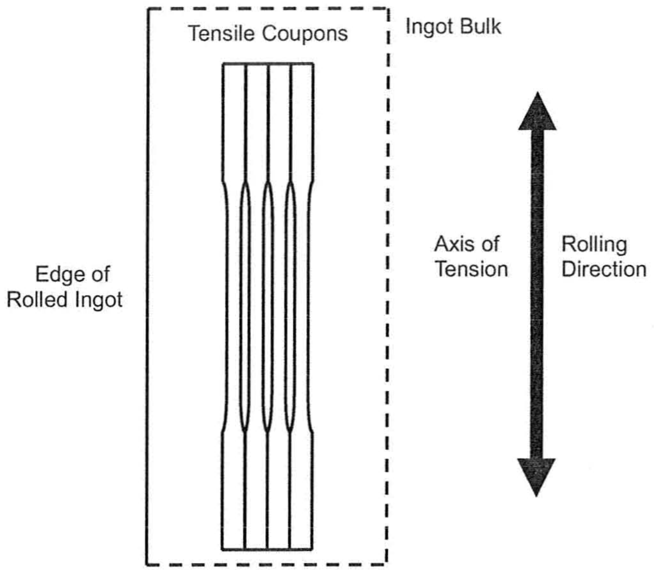

Figure 1: Orientation of Machined Samples

In the case of the Al-Cr samples, however, there was no previous knowledge found regarding annealing behavior of the alloys, necessitating a study. Samples from each solute content were annealed across a range of different temperatures, cold mounted in polymer epoxy and electrochemically etched using Barker's Re-agent. Optical microscopy was combined with a manual calculation of grain size, and it became apparent that it was not possible to anneal samples with grain sizes to match the Al-Mg alloys, while still being fully recrystallized. As a result, two sets of samples were created, one set with a consistent grain size, and another that were fully recrystallized. The details of these samples are given below in Table 2, and for all Al-Cr samples the annealing time was kept constant at 10 minutes.

Table 2: Summary of Annealing Temperatures, Grain Sizes

Designation	Solute Concentration (at% Mg / Cr)	Annealing Temperature (degrees C)	Approx. Avg. Grain Size (μm)
AL	0%	300	40
AM1	0.5%	360	38
AM2	1.08%	360	40
AM3	2.08%	400	40
AM4	3.11%	410	40
AM5	4.11%	450	40
AC1 (consistent grain size)	0.18%	320	60
AC2 (consistent grain size)	0.05%	320	70
AC3 (consistent grain size)	0.08%	320	70
AC4 (consistent grain size)	0.36%	330	50
AC1 (recrystallized)	0.18%	410	117
AC2 (recrystallized)	0.05%	410	118
AC3 (recrystallized)	0.08%	410	117
AC4 (recrystallized)	0.36%	410	108

2.2 TENSILE TESTING

Tensile tests were performed on all alloys at three different temperatures: 298K, 78K, and 4.2K using a custom-built screw-driven single axis tensile test apparatus. For the room temperature tensile tests, the samples were open to the atmosphere, but for the tests at lower temperatures, they were sealed in a chamber where the air was replaced with helium to speed up the cooling process and to limit the condensation of the air inside the chamber. For the 78K tests, this chamber was immersed in a dewar filled with liquid nitrogen, but for the 4.2K tests, a more complicated procedure was necessary. The test chamber was cooled down to 78K through liquid nitrogen immersion, as in a 78K test, but afterwards, the chamber was sealed inside a second, smaller dewar, which was then filled with liquid helium and immersed in the larger liquid nitrogen dewar. This arrangement can be seen below in Figure 2.

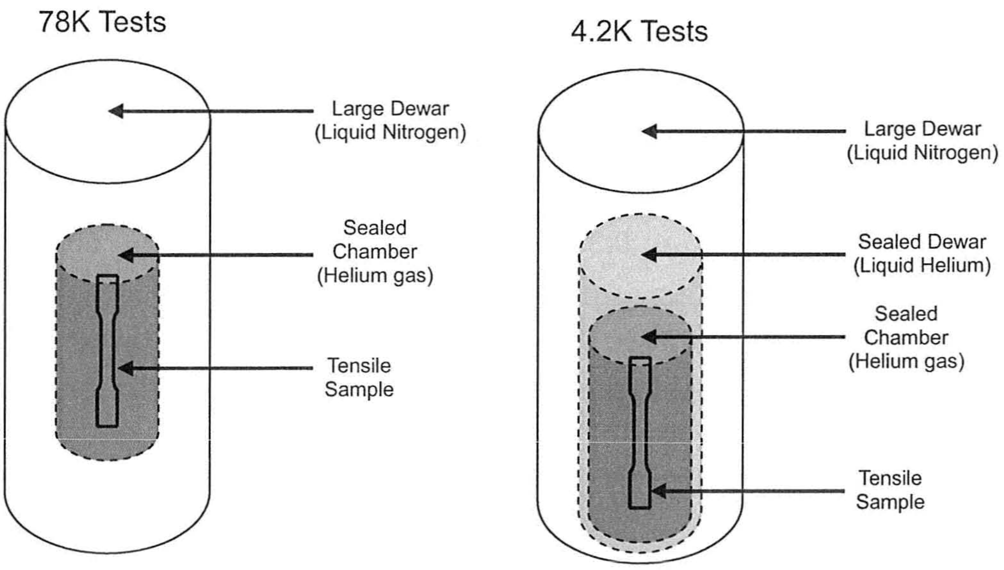

Figure 2: Dewar Arrangements for 78K and 4.2K Tensile Tests

In tests where the resistivity of the sample was also measured, the same apparatus was used. Before the inner vacuum cylinder was sealed, however, copper leads were attached to the tensile sample at the grips of the tensile machine. Copper wires providing the current were soldered to these leads, and additional wires responsible for measuring potential drop across the sample were clipped to the gauge of the sample, which underwent deformation. Resistance was measured during the cooling of the sample in order to verify the connection, so that resistivity could be accurately measured during the tensile deformation. Figure 3 below shows an example of this wiring setup.

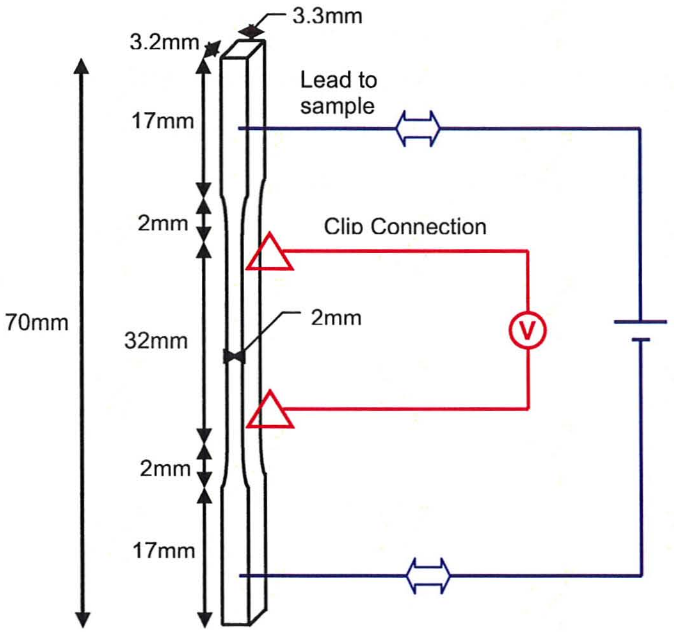

Figure 3: Tensile Sample Dimensions and Electric Connections

Strain rate sensitivity was measured by using an automatic clutch system on the apparatus to decrease the strain rate by a factor of 10, and then restore it to the original value at set time intervals, until the sample failed. The resulting stress drops and rises at these instantaneous changes in strain rate were measured across the deformation of the sample and compared across changes in alloying content through the use of Haasen plot.[35]

2.3 MICROSCOPY & ANALYSIS

2.3.1 SEM

SEM scans were performed using a Philips 515 SEM, focusing on the fracture surfaces and side profiles of selected samples. The samples were cut, either with a saw or an electro-ablative "spark cutter", and 1-3 samples were attached to the same mount using a conducting silver adhesive in order to more quickly switch from observing one sample to the next.

2.3.2 TEM

TEM samples of selected Al-Mg and Al-Cr alloys obtained from the samples taken after fracture and from non-deformed samples were prepared by manually grinding spark-cut slices taken parallel to the tensile direction down to a thickness of ~100μm. Rounded foils with a radius of 3mm were punched from these thinned slices, and these foils were then electropolished in a mixture of 30% nitric acid and methanol at ~238K (-30°C) until they were fully thinned. Figure 4 shows a visual representation of where the foils were cut from the tensile sample.

A Philips CM12 TEM was used to study the microstructure of undeformed and deformed samples from selected alloys deformed at different temperatures, as well as the evolution of the dislocation structure. Bright field and weak beam electron microscopy techniques were used in this process, with weak beam techniques being the dominant method at the highest magnifications.

In addition to the TEM microstructural study, a JEOL JEM-2010F TEM/STEM was employed to analyze the composition of significant features on some of the alloys, and to determine if concentration gradients exist in the areas surrounding grain boundaries.

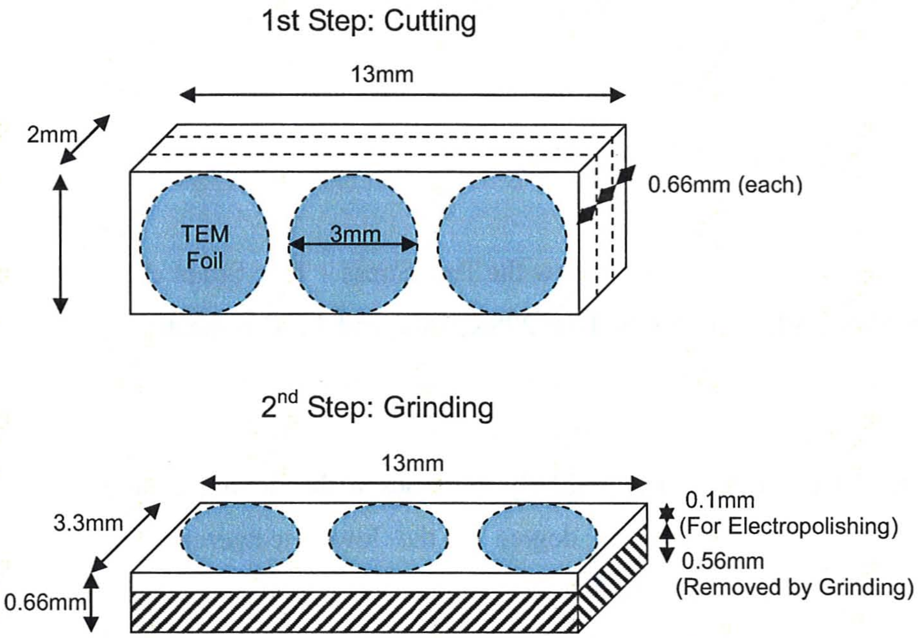

Figure 4: TEM Foil Preparation

3 EXPERIMENTAL RESULTS

3.1 MECHANICAL TENSILE TESTING

3.1.1 AL-MG SYSTEM

Figure 5, Figure 6, and Figure 7 show the True Stress – True Strain characteristics of the 5 Al-Mg alloys in this study at 298K, 78K, and 4.2K, respectively. At room temperature, the strength of the samples visibly and dramatically increases with increasing alloying content. The maximum strain before fracture for the alloys is less than that of pure Al, but similarly increases with alloying content. While these trends continue to some degree at the lower temperatures, there are numerous exceptions. At room temperature, the 3.11at% Mg sample experiences higher stresses than the 4.11at% Mg sample across much of the deformation, but at 78K the 3.11at% Mg sample appears strongest across the entirety of the deformation. Furthermore, the maximum strain before fracture of the sample with the highest Mg content drops significantly lower than any of the other Mg alloy samples, as well as the strain at fracture of the pure Al. While the maximum strain of the samples with Mg content between 0.5-2.08at% stays within a range of around +/- 2% Strain at 78K, and the fracture strain of the 4.11at% is only slightly less, the maximum strain of the 3.11at% sample is substantially larger, at 37% Strain, a value beyond even the pure Al sample. At 4.2K, this wide range of maximum strains disappears, and all alloyed samples fracture within 3% Strain of each other, all lower than the fracture strain of the pure Al sample. Also, at 4.2K the largest strains in the alloys are observed in the 4.11at%, where lower stresses are observed compared to the deformation of the 3.11at% sample.

At 298K, plastic instabilities are visible throughout the plastic deformation regions of all alloyed specimens, while the deformation of the pure Al sample is uniform throughout the entirety of its deformation. These instabilities take the form of serrations, and become more dramatic as the Mg content increases. Furthermore, the instabilities grow in amplitude at higher stresses, especially in the most alloyed samples. These serrations are indicative of the strain aging behavior known as the Portevin-LeChatelier (PLC) effect. At 78K, these instabilities are absent and the deformation is stable and uniform until fracture for all samples. At 4.2K, a different form of plastic instability appears in the alloyed samples, with stress oscillations corresponding to a clearly audible "pinging" noise heard during the test. These oscillations, with significantly greater amplitude than those observed at 298K, begin earlier and earlier as the Mg content increases, and increase in amplitude as stress and strain increase until fracture. All these features of the instabilities correspond to instances of adiabatic shear observed in previous studies[36].

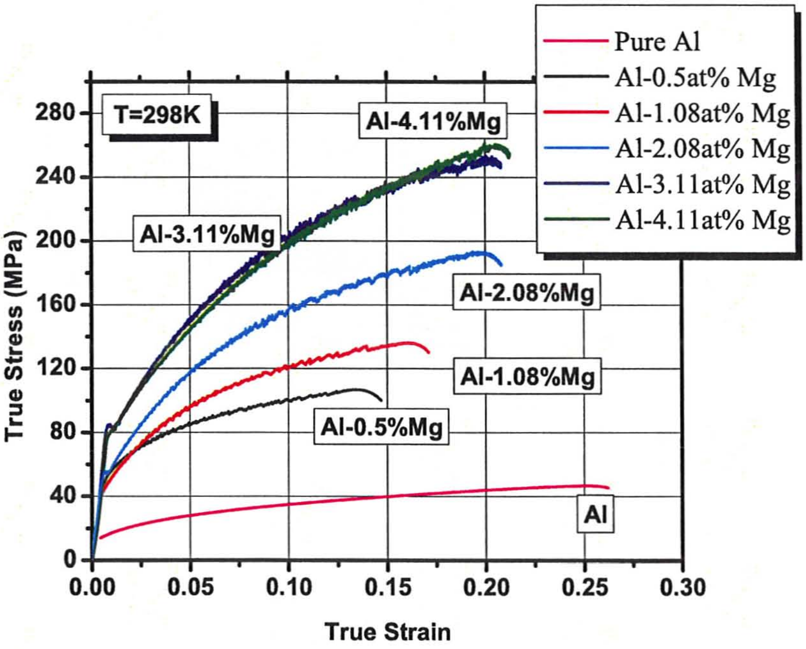

Figure 5: True Stress / True Strain behavior of Al-Mg alloys at 298K

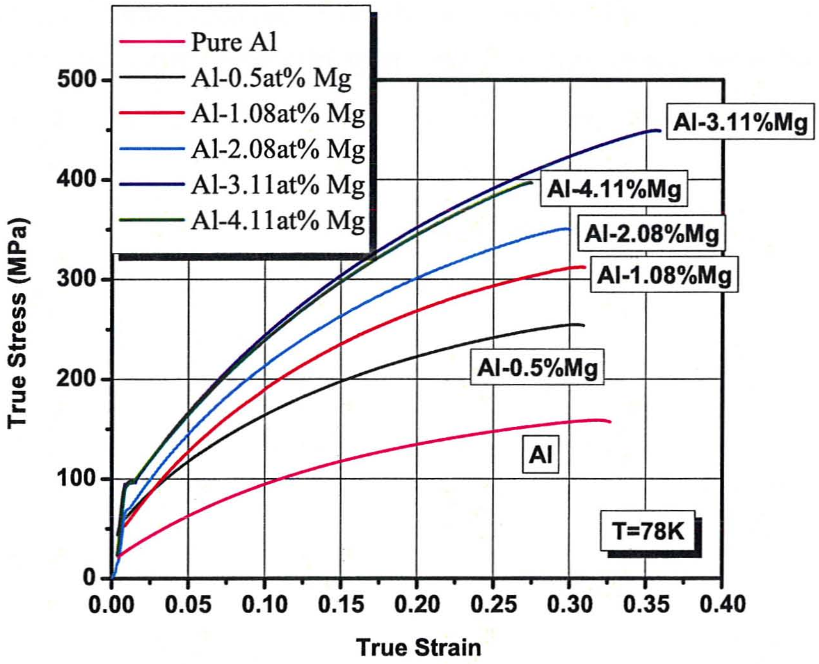

Figure 6: True Stress / True Strain behavior of Al-Mg alloys at 78K

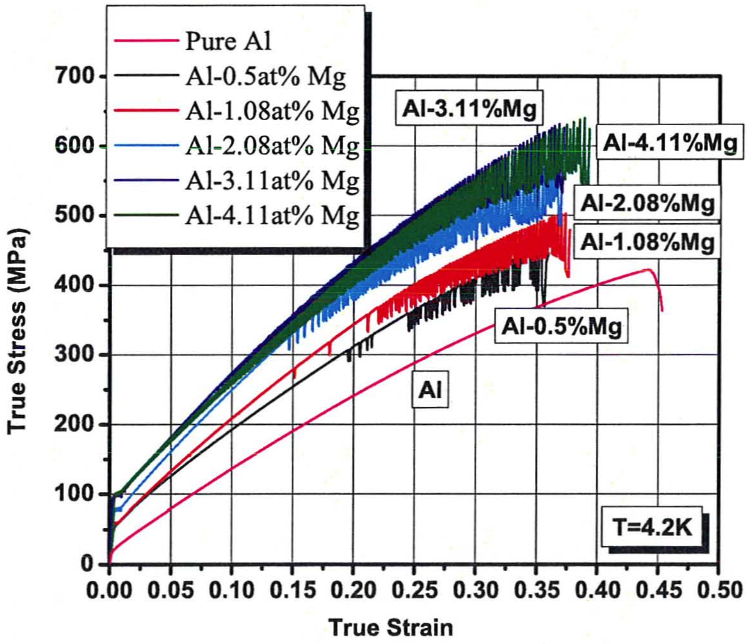

Figure 7: True Stress / True Strain behavior of Al-Mg alloys at 4.2K

As can be seen in the above charts, the decrease in experimental temperature from 298K to 78K results in an increase in flow stress and strain before fracture in all alloys, an increase that is also observed as the temperature is again decreased from 78K to 4.2K. These increases can be more clearly demonstrated by comparing the Stress-Strain curves for individual alloys, as in Figure 8, Figure 9, and Figure 10, in which the difference in the stress amplitude between the plastic instabilities at 298K and 4.2K is also more clear.

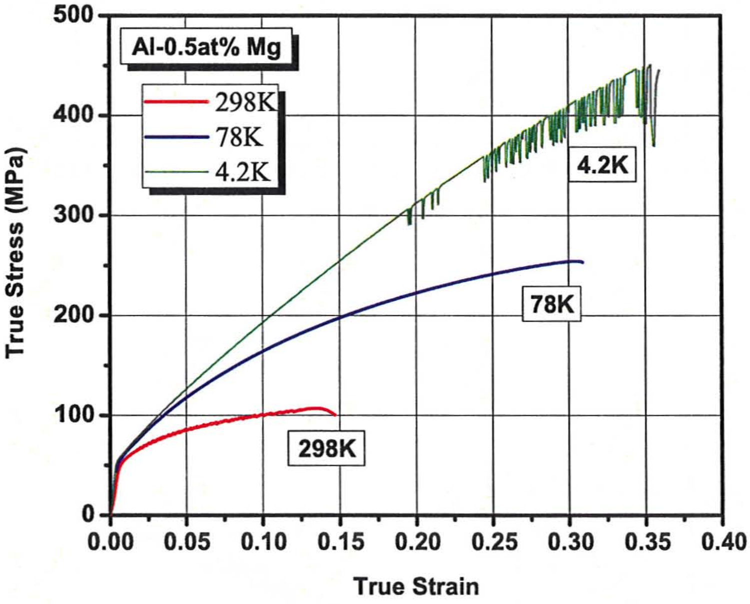

Figure 8: True Stress / True Strain behavior of Al-0.5at% Mg alloy

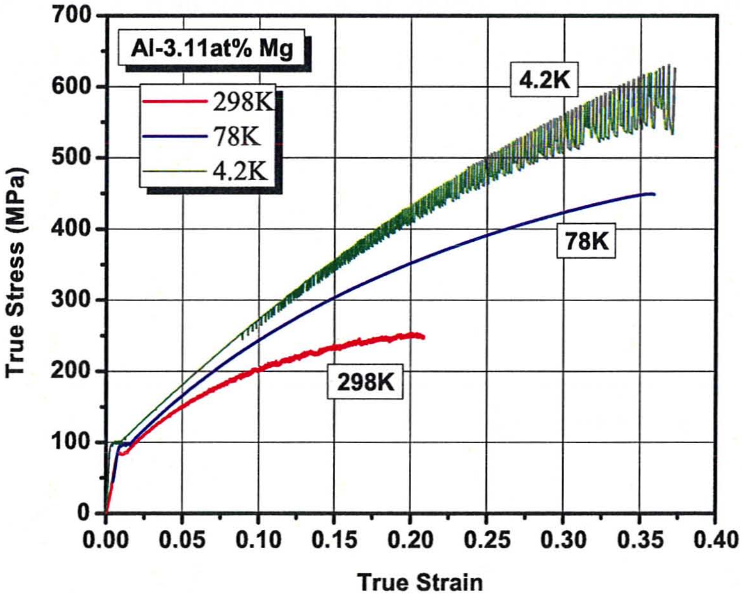

Figure 9: True Stress / True Strain behavior of Al-3.11at% Mg alloy

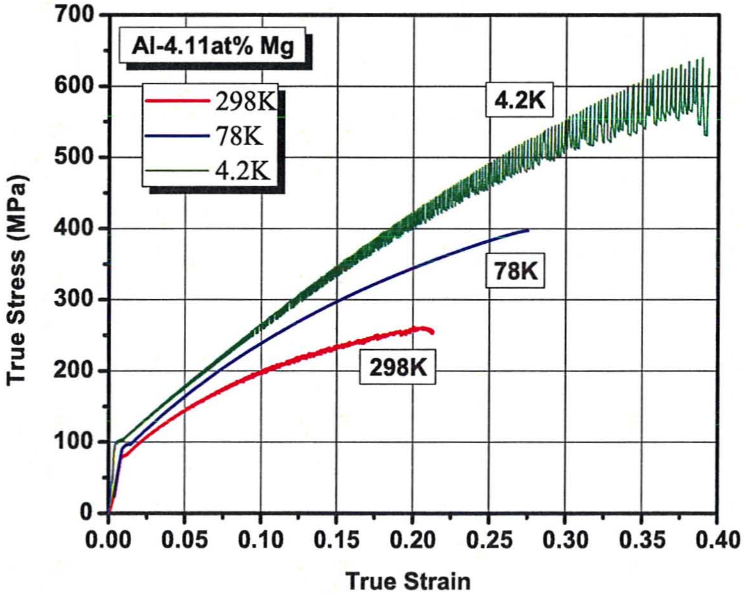

Figure 10: True Stress / True Strain behavior of Al-4.11at% Mg alloy

The maximum stresses observed in the Al-Mg tensile experiments are shown relative to Mg content in Figure 11. As previously stated, the increase in strength observed as experimental temperature is decreased is essentially linear across the 0.5-2.08at% Mg samples, and remains essentially constant in comparing the 298K tests with those at 4.2K. However, at 78K, the 2.08at% and 4.11at% samples experience a smaller increase in strength compared to other alloys, and the 3.11at% sample increases in strength significantly more than expected.

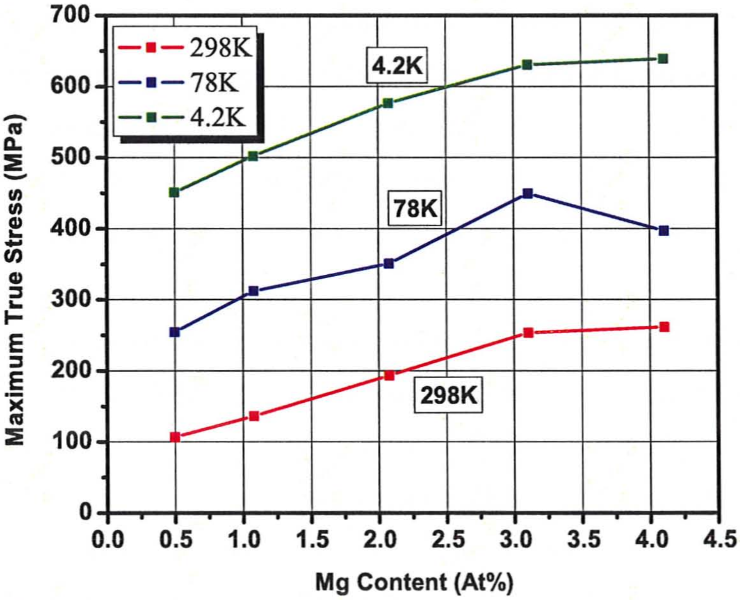

Figure 11: Maximum True Stress vs. Mg Content for Al-Mg alloys at 298K, 78K, and 4.2K

3.1.2 AL-CR SYSTEM

Figure 12, Figure 13, and Figure 14, show the True Stress – True Strain behavior of the fully recrystallized Al-Cr samples at 298K, 78K, and 4.2K, respectively. Much as with the Al-Mg samples, the Al-Cr alloy samples exhibit increased flow stresses as Cr content increases, generally higher than those observed in the pure Al sample. However, these increases in stress are relatively minor compared to the Al-Mg system, to a maximum of around 80MPa at 298K for the Al-Cr alloys, compared to roughly 260MPa for the Al-Mg alloys. In terms of strain behavior at room temperature, however, the Al-Cr alloys studied differ from the Al-Mg alloys, with each Al-Cr alloy having at least the same strain before fracture as the pure Al sample, and with the 3 lowest Cr content alloys experiencing significantly more deformation before fracture than the pure Al. Also of significance is that the maximum strains before failure appear to decrease at Cr concentrations above 0.08at%, such that at 0.36at% Cr there is no improvement over the Pure Al.

Again similar to the Al-Mg alloys studied, the decrease in experimental temperature coincides with significant increases in stresses observed across all alloys. Comparing the Al-Cr alloys to each other, the sample with the lowest Cr content (0.05at%) shows the smallest increases in strength, and is slightly weaker than pure Al at 78K, and significantly weaker than pure Al at 4.2K until the strain where pure Al begins to fail. In terms of strain, the 0.05at% Cr sample fails at a slightly higher deformation than the pure Al at 78K, and at 4.2K, fails at a noticeably higher strain than not only the pure Al, but the other Al-Cr alloys. At these high strains, the 0.05at% sample also exhibits the highest stresses observed at 4.2K. The higher Cr content samples show increasing stress with increasing Cr content at 78K, and again at 4.2K, though at that temperature the 0.18at% Cr and 0.36at% Cr samples show stresses that are nearly equivalent. At 78K, the maximum strains observed for the 0.08at% and 0.18at% Cr are roughly equivalent, but the maximum strain observed for the 0.36at% Cr sample is larger than any other alloy, and shows the greatest increase compared to its performance at room temperature for the Al-Cr alloys studied. At 4.2K, the maximum strains for the 0.08at%-0.36at% samples are within a more narrow range, with the 0.36at% Cr sample failing before the 0.018at% Cr sample, but after the 0.08at% Cr sample.

Deformation at 298K and 78K is uniform and homogenous for all alloys studied, showing no signs of the plastic instabilities (PLC effect) observed in the Al-Mg system. At 4.2K, however, the Al-Cr samples all exhibit the same kind of instabilities as observed in the Al-Mg samples, including the "pinging" noise accompanying each stress oscillation. It is likely the same, or a similar type of adiabatic shearing occurring during these tensile tests. As with the Al-Mg samples, the amplitude of these oscillations increases with stress and Cr content, and the level of deformation at which they begin to occur constantly (as opposed to intermittently) decreases with increasing Cr content.

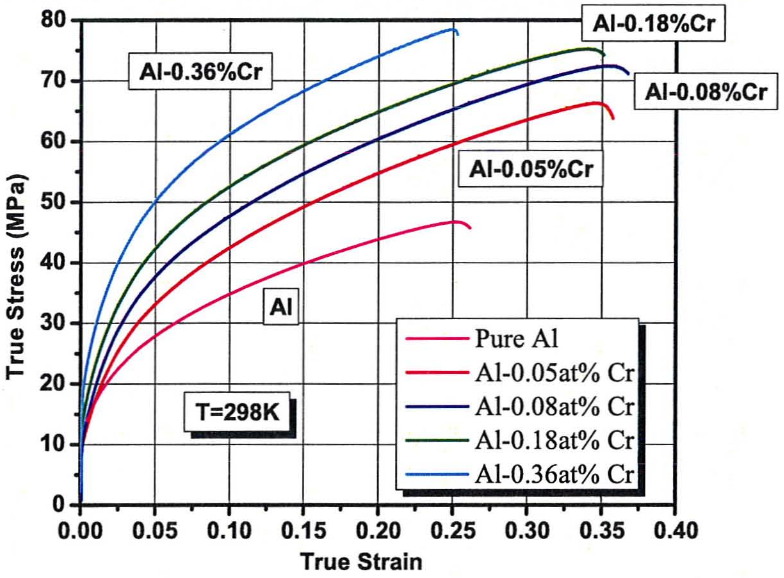

Figure 12: True Stress / True Strain behavior for Recrystallized Al-Cr alloys at 298K

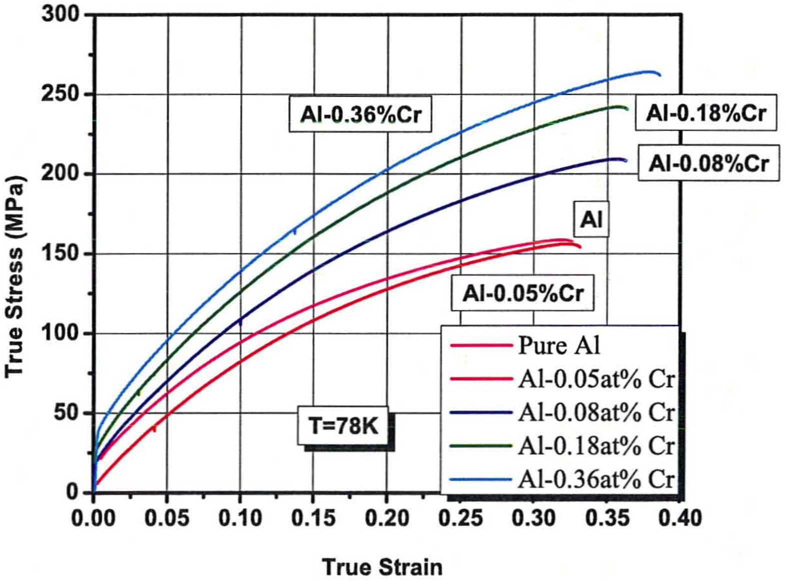

Figure 13: True Stress / True Strain behavior for Recrystallized Al-Cr alloys at 78K

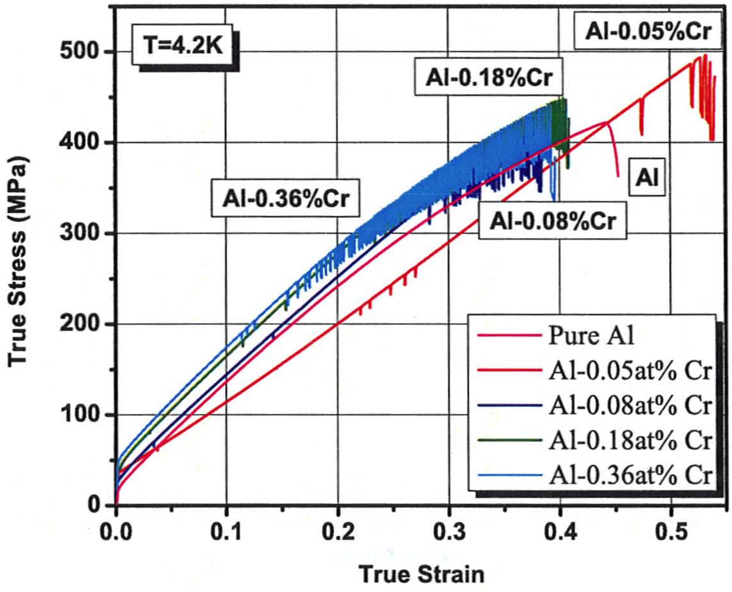

Figure 14: True Stress / True Strain behavior for Recrystallized Al-Cr alloys at 4.2K

Comparing the True Stress – True Strain curves for the 0.05at% Cr (Figure 15), 0.18at% Cr (Figure 16), and 0.36at% Cr (Figure 17) samples, the previously mentioned increases in strength and ductility resulting from decreased temperature again become more clear. More importantly, they better show the differences in the stress and strain levels at fracture between the different alloy samples. The decrease in ductility in the 0.05at% Cr sample in cooling from 298K to 78K is visible, as is the huge comparative increase in both ductility and strength observed during the test performed at 4.2K. Conversely, in the 0.36at% sample, the more significant increase in ductility and strength occurs moving from 298K to 78K, with only slight increases in ductility at 4.2K, though there is still an increase in strength. The 0.18at% Cr sample shows the most gradual and consistent increases in strength and ductility across all three temperatures for the Al-Cr alloys in this study.

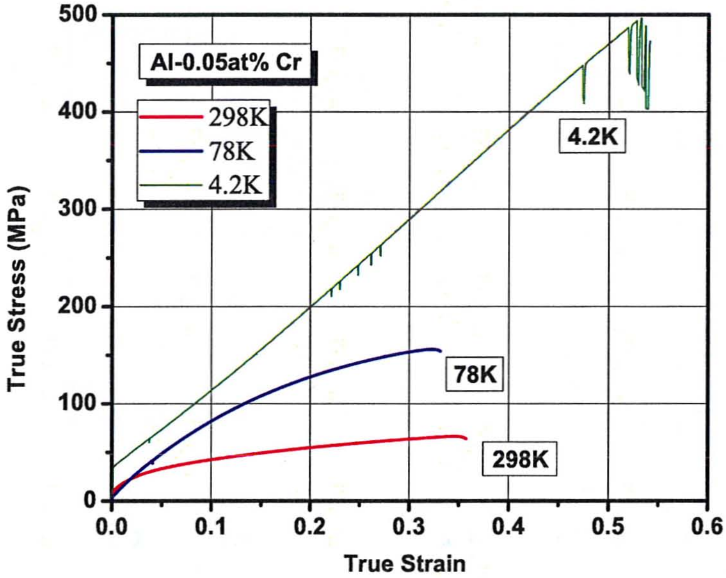

Figure 15: True Stress / True Strain behavior of Recrystallized Al-0.05at% Cr alloy

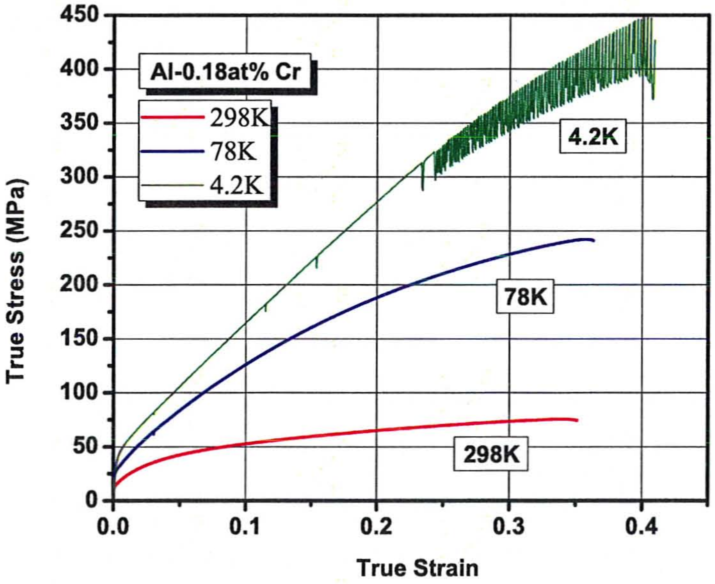

Figure 16: True Stress / True Strain behavior for Recrystallized Al-0.18at% Cr alloy

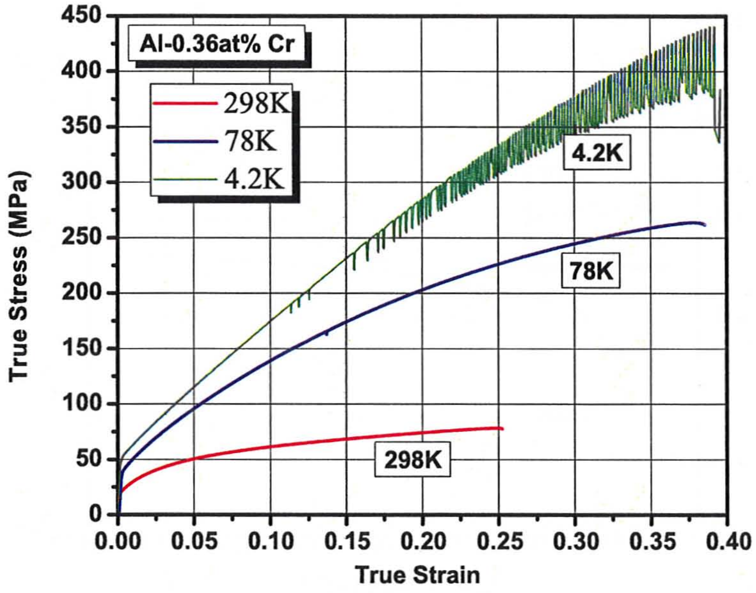

Figure 17: True Stress / True Strain behavior for Recrystallized Al-0.36at% Cr alloy

The relationship between maximum observed stress and Cr content for tensile tests at each temperature can be seen in Figure 18. As with the Al-Mg system, the increase in maximum stress as temperature decreases occurs across all alloys, though from the chart it appears the 0.18at% and 0.36at% Cr samples are strengthened more at 78K than the lower Cr-content samples. Moving from 78K to 4.2K the 0.05at% Cr sample is disproportionately strong compared to the other alloys. The 0.36at% Cr sample appears to show the greatest increase in maximum stress between 298K and 78K, and another increase comparing the tests at 78K and 4.2K, but the increase in maximum stress observed for 0.36at% sample moving from 78K to 4.2K is slightly lower than the 0.18at% Cr sample.

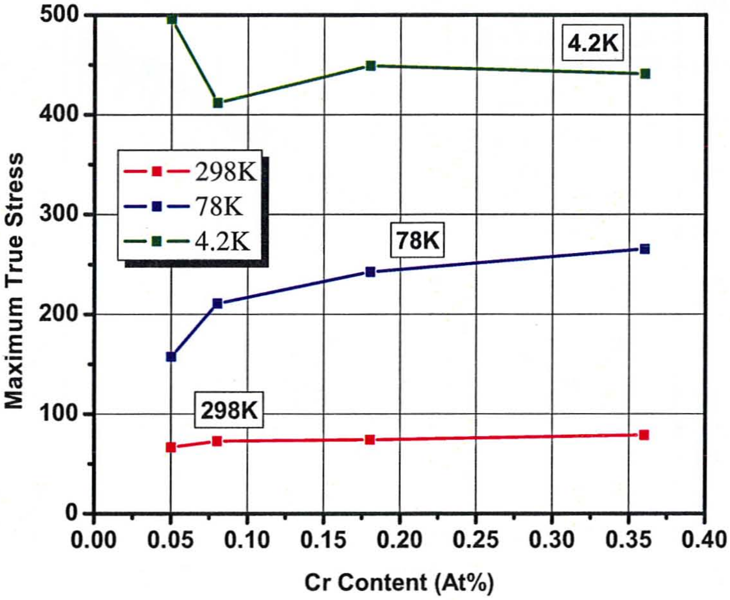

Figure 18: Maximum True Stress vs. Cr content for recrystallized Al-Cr alloys at 298K, 78K, and 4.2K

The True Stress – True Strain results for the partially recrystallized, smaller-grained Al-Cr samples can be seen in Figure 19 (298K results), Figure 20 (78K results), and Figure 21 (4.2K results). The results are similar to the fully recrystallized samples, with a few notable differences. At 298K, the samples show less evidence of increased ductility, especially the 0.18at% and 0.36at%, which both fail at far lower strains than the pure Al. The increases in strength observed with increased alloying content are also smaller than in the fully recrystallized samples, especially in the 0.05at% and 0.08at% Cr samples.

At 78K, these two low Cr samples experience much lower increases in ductility than their recrystallized counterparts, failing at lower strains than the pure Al, with the 0.08at% Cr sample failing at an even lower strain than the 0.05at% Cr sample. Unlike the recrystallized sample test for the 0.36at% Cr sample at 78K, the sample fails at a lower strain than the pure Al, and does not exhibit the same increases in strength as the recrystallized sample. As at 298K, the strengths of any smaller-grained samples at 78K is lower than if it were fully recrystallized.

At 4.2K, the behavior of the partially recrystallized samples is most comparable to being fully recrystallized. The strengths and maximum strain are roughly the same for each sample, except the 0.05at% sample, which fails at roughly the same strain as the other alloys, instead of continuing to deform and harden in the fully recrystallized case. The adiabatic shearing behavior of the lower grain size alloys is equivalent to the recrystallized samples as well.

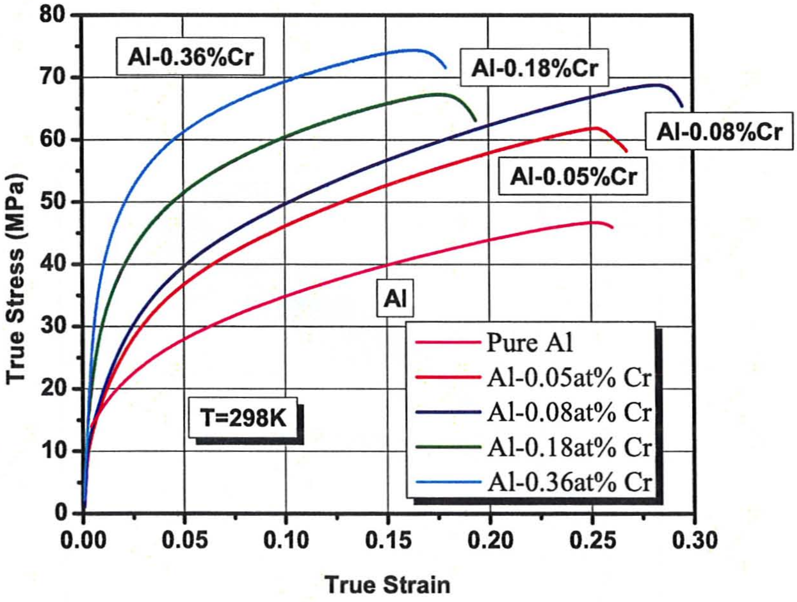

Figure 19: True Stress / True Strain behavior for Partially Recrystallized Al-Cr alloys at 298K

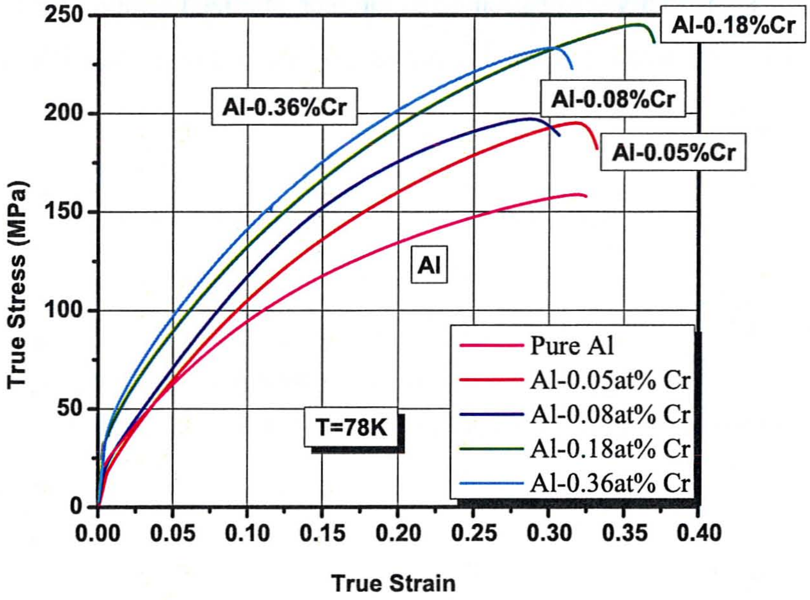

Figure 20: True Stress / True Strain behavior for Partially Recrystallized Al-Cr alloys at 78K

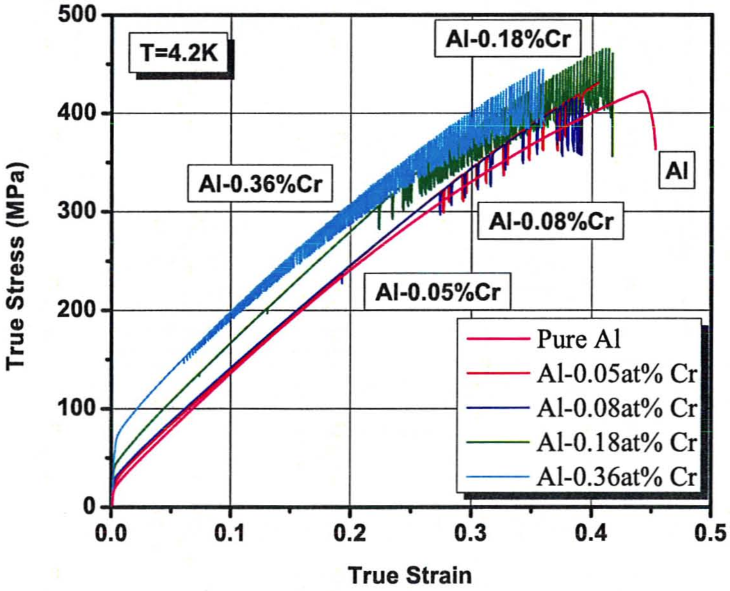

Figure 21: True Stress / True Strain behavior for Partially Recrystallized Al-Cr at 4.2K

3.2 3.2: WORK HARDENING RESULTS

3.2.1 3.2.1: AL-MG SYSTEM

Figure 22, Figure 23, and Figure 24 show the work hardening rate plotted as a function of the True Stress for tests performed at 298K, 78K and 4.2K. The huge increase in work hardening capacity for all Mg alloys compared to pure Al is clear at all temperatures, where even the weakest alloy has an initial work hardening rate almost three times larger than pure Al at 298K. The initial work hardening rates at 298K also increase with alloying content, although the initial work hardening rate for the 4.11at% Mg sample is less than that of the 3.11at% Mg sample. The work hardening capacities similarly increase with Mg content, with the capacity of the 3.11at% Mg sample being greater than that of the 4.11at% Mg alloy, though the work hardening rate of the 3.11at% Mg sample decreases more rapidly than for the 4.11at% Mg sample until the stress reaches around 125MPa, at which point the work hardening behavior of the two alloys becomes nearly identical. Across the entire test, the work hardening rates appear to decrease more slowly than that of the lower Mg content alloys. It is also observed that the decrease of the work hardening rate becomes more and more erratic at higher stresses for each alloy, and that for the higher Mg content alloys, this erratic region encompasses more of the test. The magnitude of the "scattering" of work hardening rates is also much larger for the higher Mg content alloys, though this could be due to the higher stresses involved in their deformation and failure. It is likely that this instability is a reflection of the plastic instabilities (PLC effect) previously mentioned in this report. In contrast, the work hardening profile of the pure Al sample show none of these instabilities, and has an exponential character, as opposed to the more logarithmic character observed in the profiles of the alloys.

At 78K, the work hardening rates of the alloys remain higher than that of Pure Al, though the difference is not as large (a factor of 1.75 for the 0.5at%Mg alloy, as opposed to a factor of 3 at 298K). Again, the 3.11at% and 4.11at% Mg samples exhibit very similar work hardening behavior, with the work hardening rates of the 3.11at% Mg sample slightly higher at a given stress than the 4.11at% Mg sample. The work hardening rate in the 3.11at% test at 78K decreases at a uniform rate until stress reaches roughly 450MPa, while the work hardening rate of the 4.11at% sample "drops off" at around 400MPa. The initial work hardening rate of the 2.08at% Mg sample is noticeably higher than that of the higher Mg content alloys, but decreases more quickly, such that the work hardening rate reaches zero at a stress consistent with the trend set by the other alloys. The work hardening behavior of the alloys at 78K is also more uniform and consistent than at 298K, and more similar to that of the pure Al profile, which at this temperature shares the logarithmic shape of the alloys.

At 4.2K, while the work hardening behavior of the pure Al remains uniform, for the alloys it becomes even more unstable than at 298K, most likely due to the adiabatic shearing effects mentioned earlier. Again, an increased initial work hardening rate for the alloys is observed compared to pure Al, with that initial work hardening rate increasing with alloying content up to 3.11at% Mg, which shows a larger initial rate than the 4.11at% Mg alloy. Due to the instabilities, it becomes more difficult to accurately compare the work hardening behavior of the alloys, but for the majority of the deformation, the work hardening rates of the 2.08-4.11at% Mg alloys appear to be similar to each other, with the 2.08at% Mg sample having larger work hardening rates than the 4.11at% until around 300 MPa, where a rapid drop occurs for a short period of time. Similarly, the 3.11at% exhibits larger rates than the 4.11at% Mg sample, up to around stresses of 450 MPa, at which point the work hardening rates begin to drop more rapidly than the 4.11at% Mg sample. It is also observed that although the work hardening profiles of the tests remain a logarithmic shape across the higher stresses, during the initial deformations (and thus, at the highest work hardening rates), the profiles take on a more exponential shape, even for the pure Al sample, which then flows into the logarithmic profile.

The work hardening behavior of the 2.08at% Mg sample, the 3.11at% Mg sample, and the 4.11at% Mg sample relative to stress are shown in Figure 25, Figure 26, and Figure 27. The increase in work hardening capacity is clearly visible as temperature is decreased in all three alloys, as is the large level of instability at 4.2K. Though the absolute maximum work hardening rate at 4.2K is much higher than at 298K or 78K for the 3.11at% Mg and 4.11at% Mg alloys, at the point where the work hardening rates "level off" into a more consistent plot the work hardening rate is almost the same across all three temperatures. It is difficult to accurately compare how close the work hardening rates for the 2.08at% Mg, 3.11at% Mg and 4.11at% Mg are, due to the instabilities present, but the three alloys appear to have similar work hardening rates throughout the deformation, though the 3.11at% Mg alloy appears to have the highest work hardening rates and the slowest decrease at a given stress, and the two remaining alloys alternating between having the 2nd and 3rd highest work hardening rates at a stress of around 325 MPa.

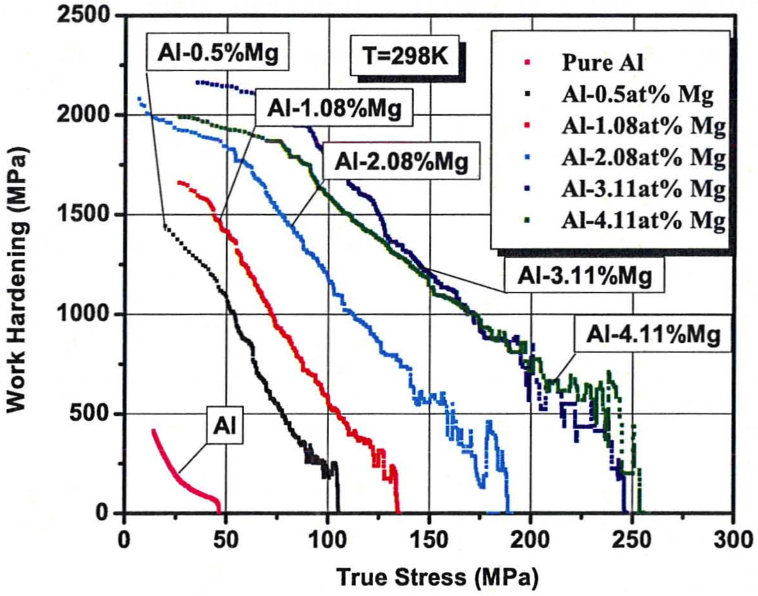

Figure 22: Work Hardening rate vs. True Stress for Al-Mg alloys at 298K

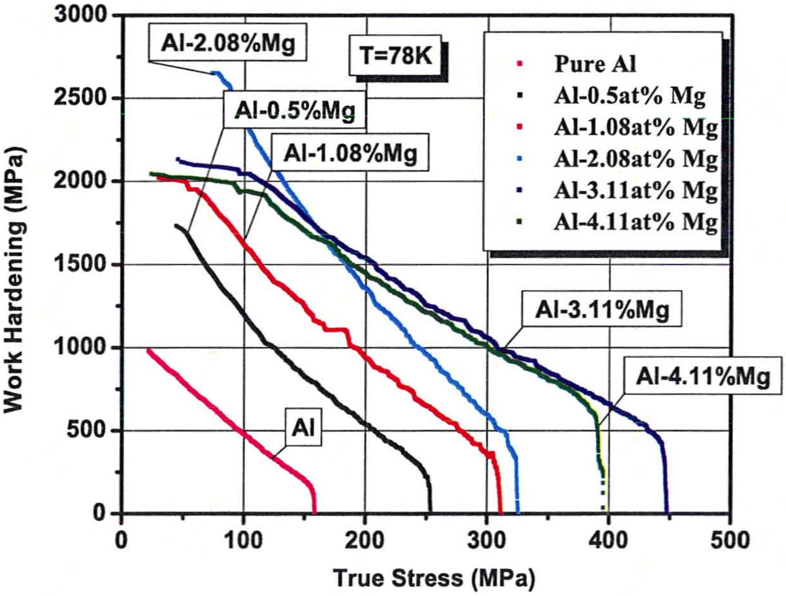

Figure 23: Work Hardening Rate vs. True Stress for Al-Mg alloys at 78K

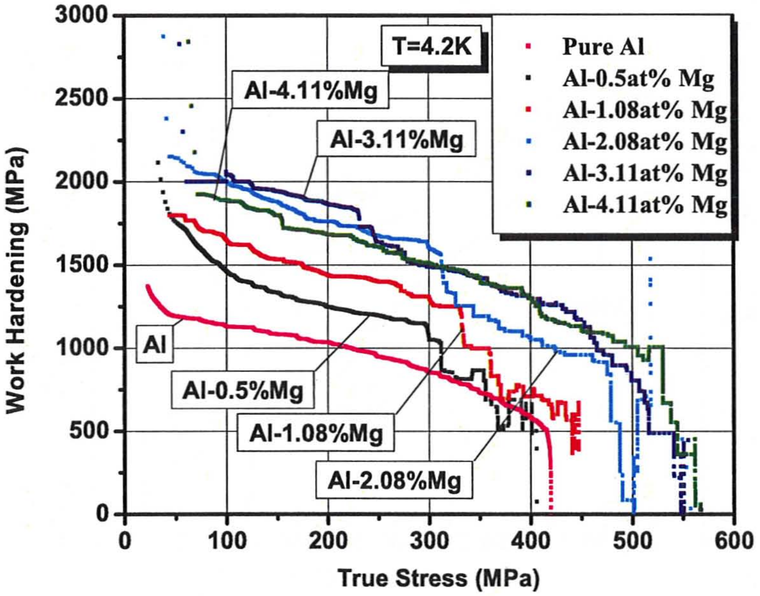

Figure 24: Work Hardening Rate vs. True Stress for Al-Mg alloys at 4.2K

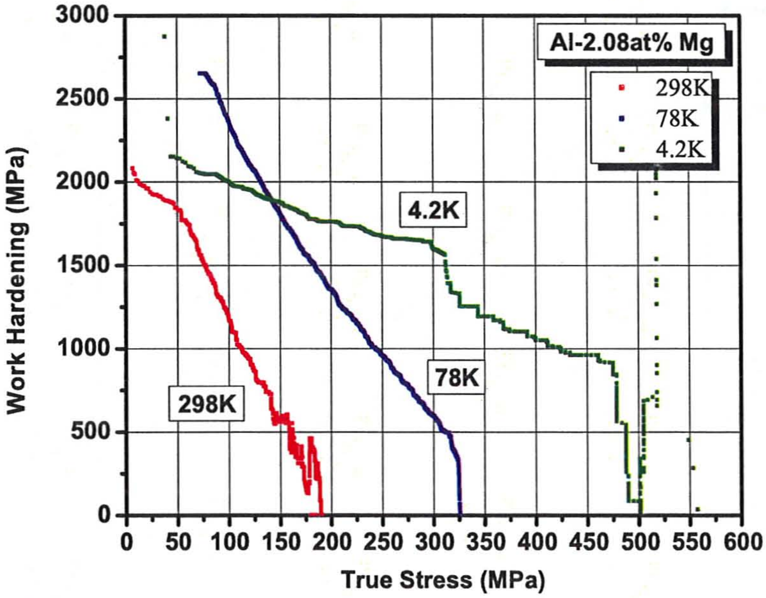

Figure 25: Work Hardening Rate vs. True Stress for Al-2.08at% Mg alloy

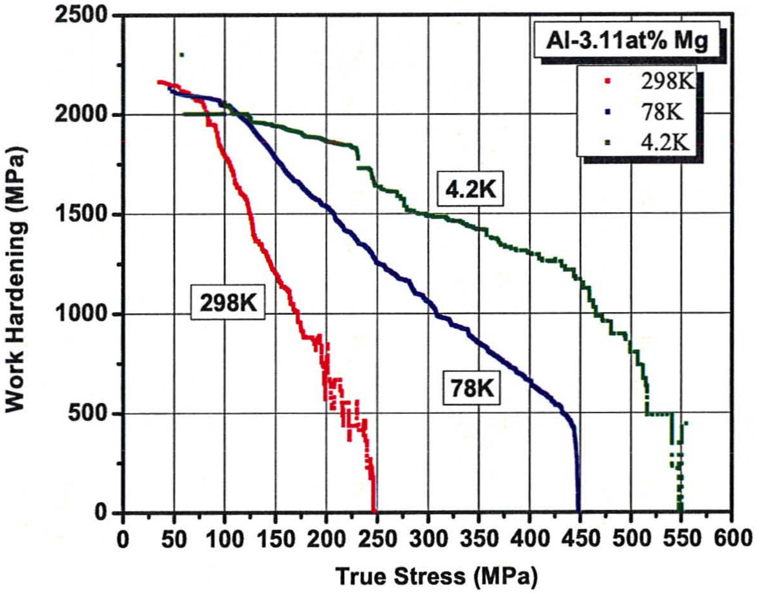

Figure 26: Work Hardening Rate vs. True Stress for Al-3.11at% Mg alloy

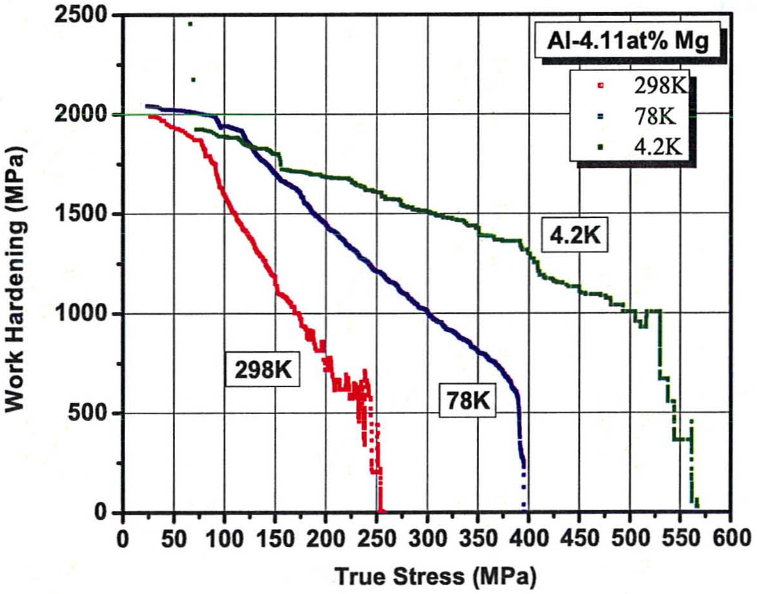

Figure 27: Work Hardening Rate vs. True Stress for Al-4.11at% Mg alloy

3.2.2 3.2.2: AL-CR SYSTEM

As in the Al-Mg system, an increase in alloying content results in a general increase in initial work hardening rate and overall work hardening capacity for the alloys studied. Figure 28, Figure 29, and Figure 30 show the plot of Work Hardening Rate vs. True Stress across 298K, 78K, and 4.2K for the recrystallized samples. At 298K, all of the alloys exhibit larger initial work hardening rates and work hardening capacities than the pure Al sample, and both parameters are observed to increase with Cr content. Similarly, the rate at which the work hardening rate decreases appears to be lower in the alloyed samples, as their curves show a slightly lower slope than that of the pure Al. Unlike the Al-Mg alloys, the work hardening rate of the Al-Cr alloys decreases at a more exponential rate at 298K (rather than logarithmic) until it reaches a point where a rapid drop occurs. The stress at which this drop occurs increases with increasing Cr content, though after 0.08at% Cr, the benefits observed from each increase seem to diminish.

At 78K, the 0.05at% Cr sample exhibits a lower initial work hardening rate and work hardening capacity than the Pure Al sample, which parallels the stress behavior observed in Figure 28. The initial work hardening rate of the 0.18at% Cr sample is larger than that of the 0.36at% Cr sample, though after a rapid decrease in work hardening rate in the 0.18at% Cr sample, the two high Cr alloys show roughly equivalent work hardening rates until stress reaches roughly 125 MPa, at which point the two profiles begin to diverge such that the 0.18at% Cr sample shows higher work hardening rates at the same stresses and "drops off" at a higher stress than the other alloys at 78K. Again, the benefits in work hardening capacity and rate due to higher Cr content seem to diminish after 0.08at% Cr.

Similar to the Al-Mg 4.2K test, the Al-Cr 4.2K results show a large degree of instability in the alloyed samples, which makes an attempt to draw conclusions from them more difficult. The work hardening rates in the pure Al sample drop in a clear, consistent trend, and the stress at which the work hardening rate suddenly drops in the pure Al is higher than all but the 0.05at% Cr sample, which has the lowest Cr content. The initial work hardening rate for the 0.05at% Cr sample is slightly higher than that of the 0.08at% Cr sample, which is almost the same as that of the pure Al sample. The initial work hardening rate of the 0.18at% Cr sample is slightly higher than that of pure Al, but the 0.36at% Cr sample has a much higher initial rate, almost 60% larger than the initial rate of the closest sample. The work hardening rates of the 0.36at% Cr sample decrease quickly and more steadily than the other samples, however, exhausting the work hardening capacity of the sample at the lowest observed stresses at 4.2K, though very close to the exhaustive stress of the 0.08at% Cr sample. The work hardening profiles of the alloys also vary the most at this temperature, possibly due to the instabilities. The work hardening rate of the 0.18at% Cr alloy decreases quickly, then plateaus, then drops again at around 300 Mpa, where it erratically decreases until the work hardening rate reaches 0. The results from the 0.08at% Cr sample take a similar shape, but continue to decrease, rather than leveling off, and begin to drop at a higher stress, around 350 MPa, but then sharply drop, reaching 0 at a lower stress than all but the 0.36at% Cr sample. Lastly, the 0.05at% Cr sample has a profile roughly equivalent to that of the 0.08at%, though with a sharper rate drop at the beginning due to the higher initial rate, though the work hardening rate only begins to drop more sharply at around 375MPa instead of 350MPa, and then returns to a more gentle slope shortly after, such that the work hardening rate is around 750 MPa when fracture occurs.

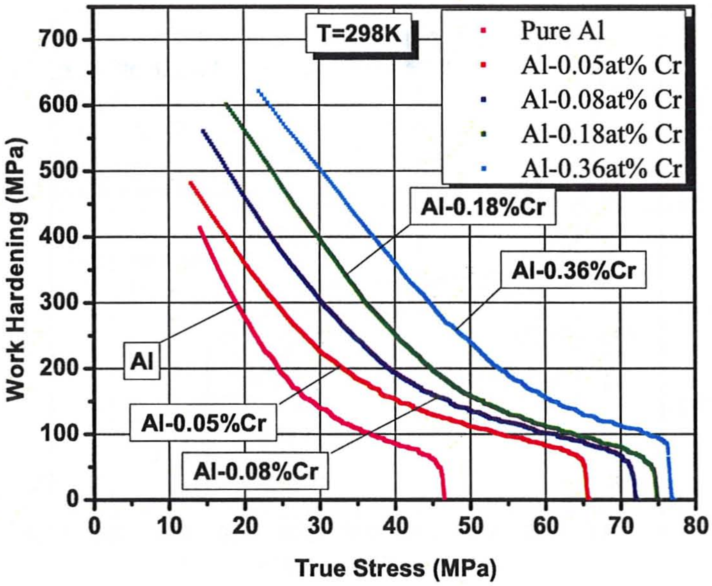

Figure 28: Work Hardening Rate vs. True Stress for Recrystallized Al-Cr alloys at 298K

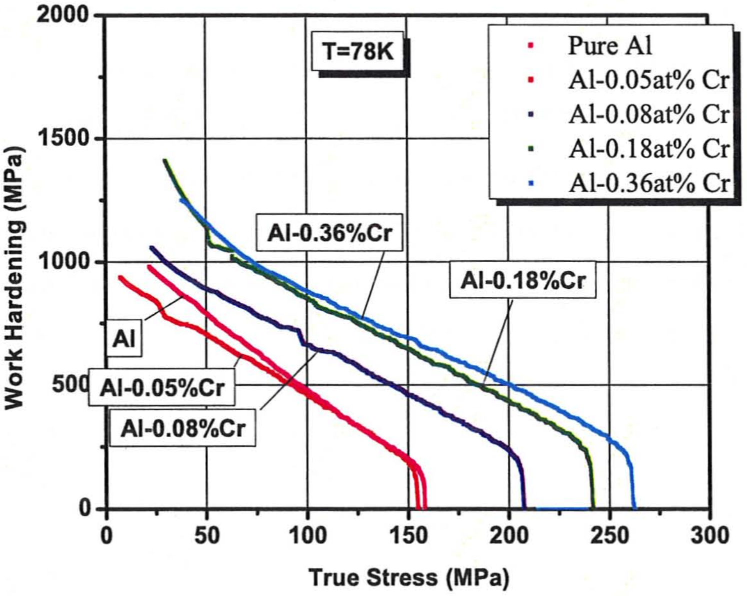

Figure 29: Work Hardening Rate vs. True Stress for Recrystallized Al-Cr alloys at 78K

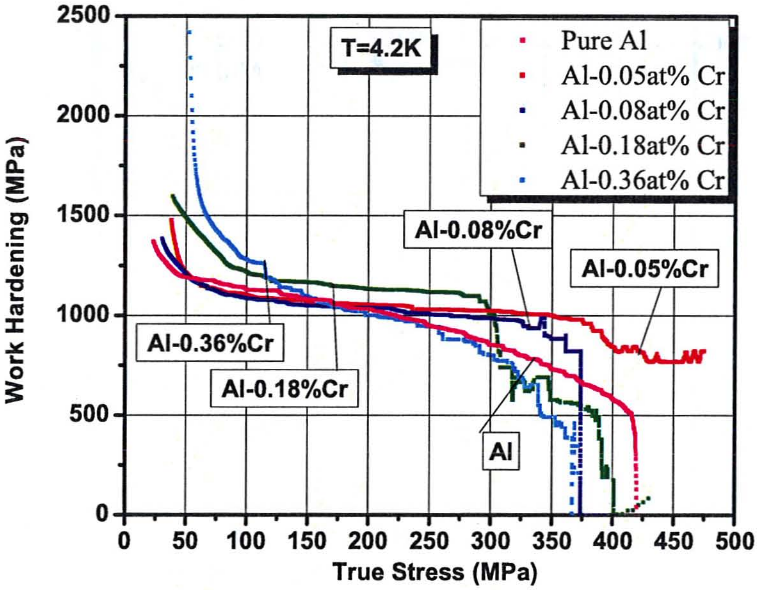

Figure 30: Work Hardening Rate vs. True Stress for Recrystallized Al-Cr alloys at 4.2K

The Work Hardening Rate vs. True Stress behavior of the 0.05at% Cr, 0.18at% Cr, and 0.36at% Cr samples relative to temperature can be seen in Figure 31, Figure 32, and Figure 33. The increase in initial work hardening rate and work hardening capacity as a result of decreased temperature is more clearly visible, as are the instabilities present at 4.2K. For the 0.05at% Cr sample, the seemingly large work hardening capacity remaining at the fracture, almost 25% larger than the initial work hardening rate at 298K, is also visible.

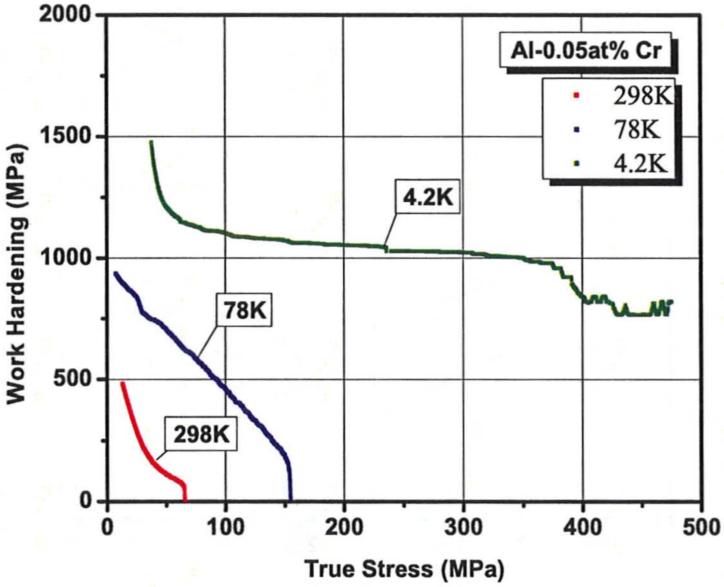

Figure 31: Work Hardening Rate vs. True Stress for Recrystallized Al-0.05at% Cr alloy

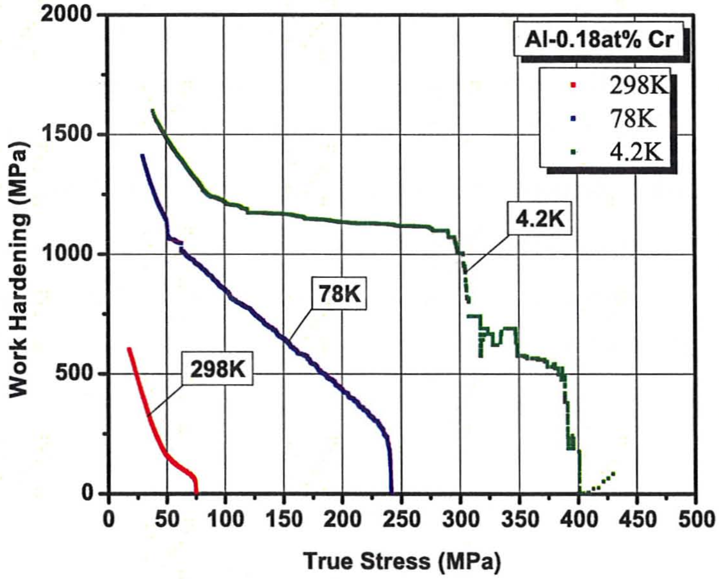

Figure 32: Work Hardening Rate vs. True Stress for Recrystallized Al-0,18at% Cr alloy

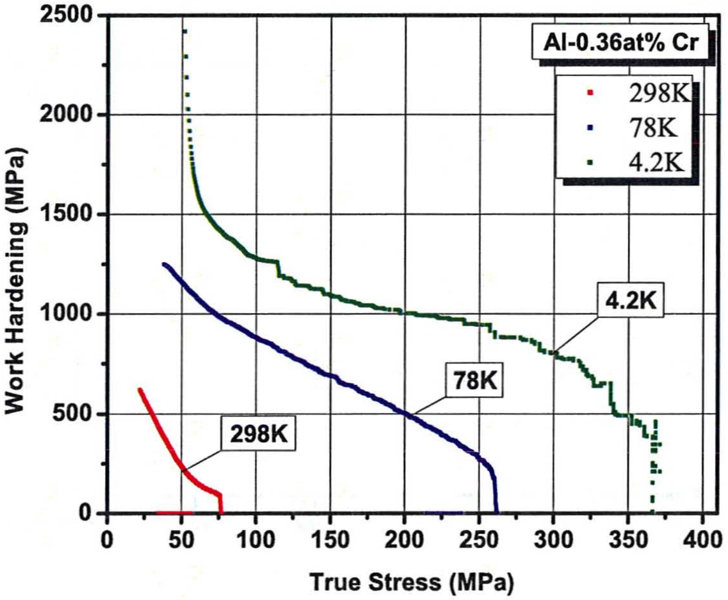

Figure 33: Work Hardening Rate vs. True Stress for Recrystallized Al-0.36at% Cr alloy

Comparing the work hardening results of the recrystallized samples to results from the partially recrystallized samples, shown in Figure 34, Figure 35, and Figure 36, the trend of increased initial work hardening rates and capacities with increased solute content generally hold true, though at 298K the partially recrystallized samples exhibit much higher initial work hardening rates, especially the two higher Cr content alloys. The work hardening rates decrease much more quickly than in the fully recrystallized samples (again, especially the two higher Cr content alloys), though they reach a work hardening rate of 0 at around the same stresses as the partially recrystallized samples, though in the partially recrystallized samples the 0.18at% Cr sample reaches this rate at a lower stress than the 0.08at%Cr sample, rather than at a higher stress.

At 78K, the 0.05at% Cr sample shows significantly improved work hardening properties over pure Al, as opposed to the lower capacity observed in the recrystallized sample. Larger initial work hardening rates compared to the recrystallized samples are again observed in the smaller-grained samples, as are the more rapid decreases of their work hardening rates. Though the 0.36at% Cr sample shows the highest work hardening rates at a given stress for the partially recrystallized samples at this temperature throughout the majority of its deformation, its work hardening rate also decreases the most quickly, such that the work hardening rate becomes lower than those of the 0.18at% Cr sample at around 230MPa, and the work hardening rate reaches 0 at a slightly lower stress than the 0.18at% Cr sample. The 0.36at%Cr sample also shows some kind of minor instability at around 150 MPa, though this instability appears to have no effect on the general trend of decrease in work hardening rate.

At 4.2K, the work hardening behavior of the partially recrystallized samples is closest to that of the fully recrystallized samples. The stresses at which the 0.08-0.36at% Cr samples reach a work hardening rate of 0 is slightly higher than in the recrystallized samples, but other than this, the behavior is very similar in all samples. A high initial work hardening rate and rapid decrease of hardening rate is obersered in both 0.36at% Cr samples, and the 0.05%at Cr and 0.08at% Cr samples have lower work hardening rates than the pure Al for a segment of their deformation in both fully and partially recrystallized samples. The high work hardening rate observed in the 0.05at% sample at the fracture is also apparent in both cases.

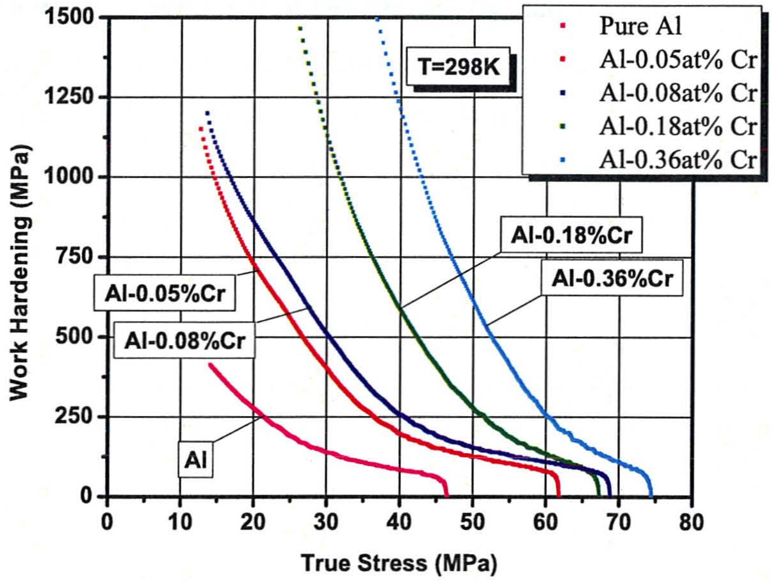

Figure 34: Work Hardening Rate vs. True Stress for Partially Recrystallized Al-Cr alloys at 298K

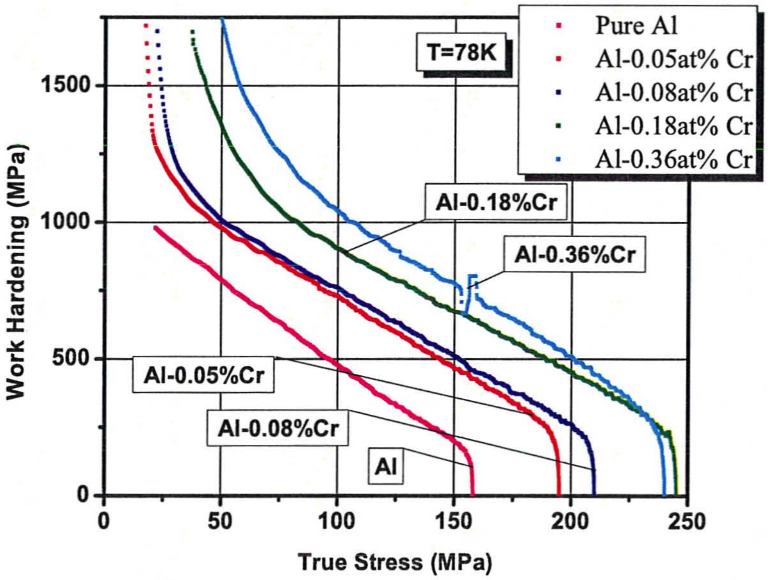

Figure 35: Work Hardening Rate vs. True Stress for Partially Recrystallized Al-Cr alloys at 78K

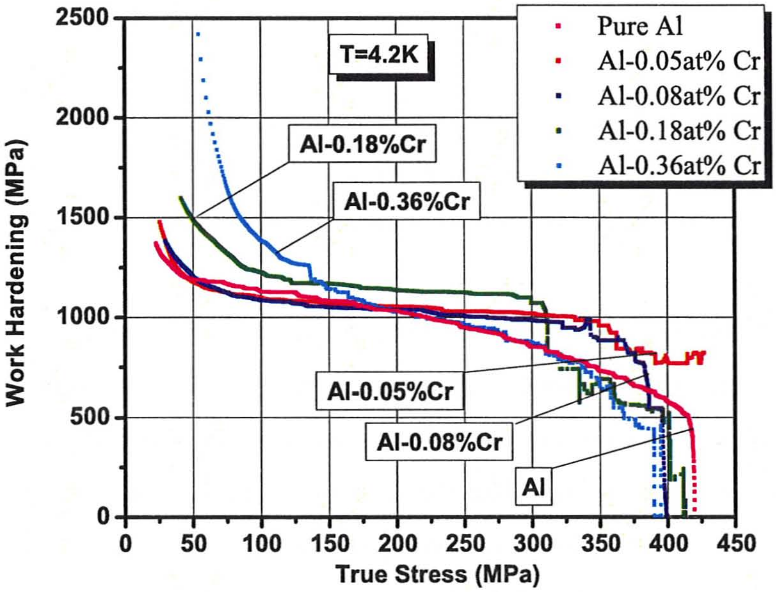

Figure 36: Work Hardening Rate vs. True Stress for Partially Recrystallized Al-Cr alloys at 4.2K

3.3 3.3: RESISTIVITY RESULTS

3.3.1 3.3.1: AL-MG SYSTEM

Due to excessive signal noise arising from phonon scattering, resistivity changes above the level of background noise present for the Al-Mg samples were only observed at 4.2K. Figure 37 and Figure 38 show the evolution of resistivity relative to True Strain and True Stress for the Al-Mg samples. These results agree with previous studies, in that the resistivity of the Al-Mg alloys is observed to rise more quickly at a roughly parabolic rate, and to larger limits than the pure Al[37]. Also observed is an increase in scattering in the alloys compared to the pure Al, and an even higher level of scattering in the higher Mg content alloys. This scattering "noise" prevents the collection of resistivity data for the Al-4.11at% Mg alloy except at high stresses where the resistivity changes exceed the scattering noise. Scattering also becomes more apparent for all other alloys except the Al-0.5at% Mg sample as stresses increase. This increase in scattering is possibly affected by the adiabatic shearing effect mentioned previously.

Relative to strain, the decrease of the resistivities of the Al-Mg alloys with increased Mg content becomes less apparent, as both the pure Al sample and Al-0.5at% Mg sample fail to fit the trend. These two samples, especially the pure Al sample, have lower resistivities than the Al-0.5at% Mg alloy at low strains, and their resistivities rise at a slower rate compared to the other alloys, such that at failure, the Al-0.5at% Mg alloy has a lower resistivity than all other alloys except the Al-4.11at% Mg alloy, and the pure Al sample has the lowest resistivity at that same strain. Comparing the samples using stress, however, there is a much more consistent trend observed between the samples. Resistivity rises more slowly with increased alloying content, and occurs across all alloys, as well as the pure Al sample. At lower stresses, resistivity changes for the 2.08-4.11at% Mg alloys are obscured by background scattering, and the stresses at which these changes are not detected increases with Mg content. As in Figure 37, scattering in the resistivity measurements is more prevalent in the higher Mg content alloys, and at higher stresses. The alloys also all seem to reach roughly the same resistivity before failing, around 1.5×10^{-7} Ω·cm, with the exception of the Al-0.5at% Mg sample, which fails earlier, and only reaches a resistivity around 1×10^{-7} Ω·cm. All the alloys fail at a lower resistivity than the pure Al sample.

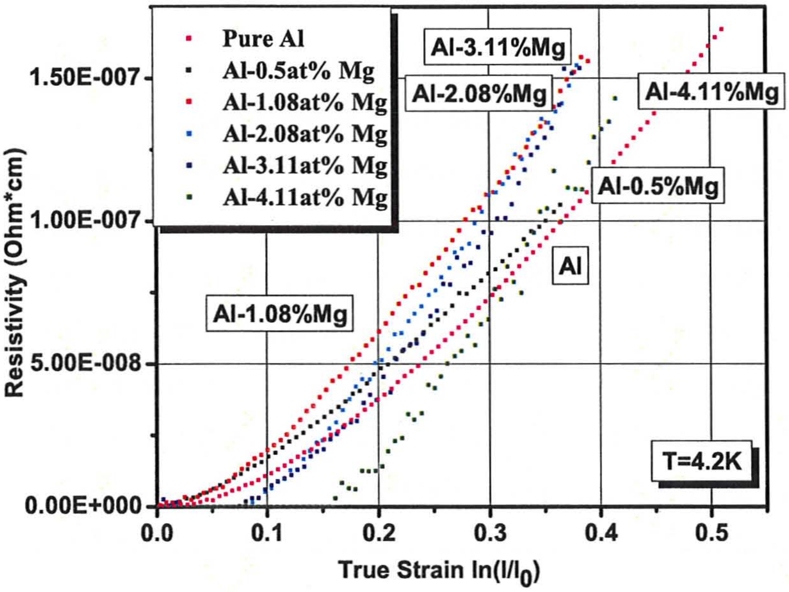

Figure 37: Resistivity vs. Strain data for Al-Mg alloys

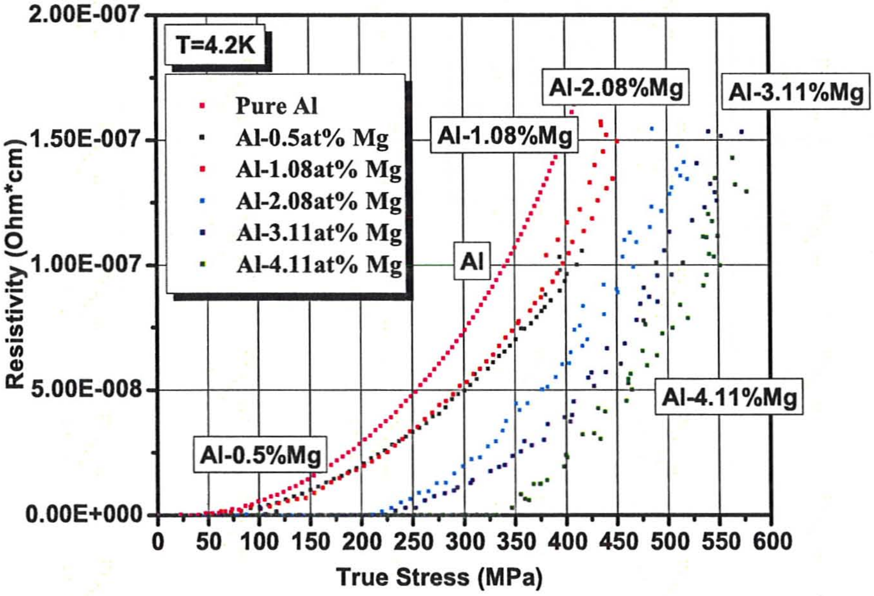

Figure 38: Resistivity vs. Stress data for Al-Mg alloys

3.3.2 3.3.2: AL-CR SYSTEM

As in the Al-Mg system, excessive scattering prevents the collection of resistivity data at temperatures above 4.2K for the Al-Cr samples, and even then excessive solute scattering obscures the results of some samples. For the fully recrystallized samples, the resistivity vs. the True Strain and True Stress are shown in Figure 39 and Figure 40. As with the Al-Mg samples, the fully recrystallized Al-Cr alloys show a decrease in resistivity at a given strain or stress as the alloying content increases, though at very low stresses and strains the reverse is true. Solute scattering of resistivity data obscures the results for the Al-0.36at% Cr sample except at very high stresses/strains. Unlike the Al-Mg alloys, all the Al-Cr samples reach different resistivities before failing, and these final resistivities decrease as Cr content increases.

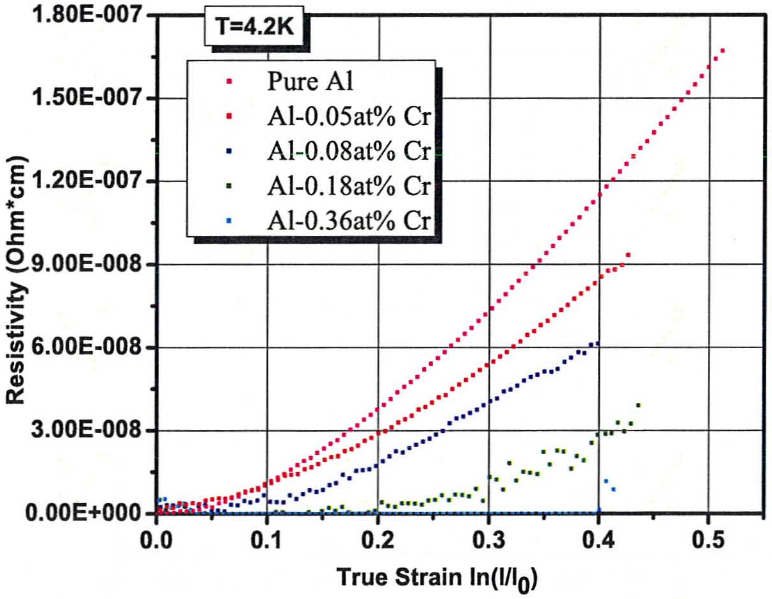

Figure 39: Resistivity vs. Strain data for Recrystallized Al-Cr alloys

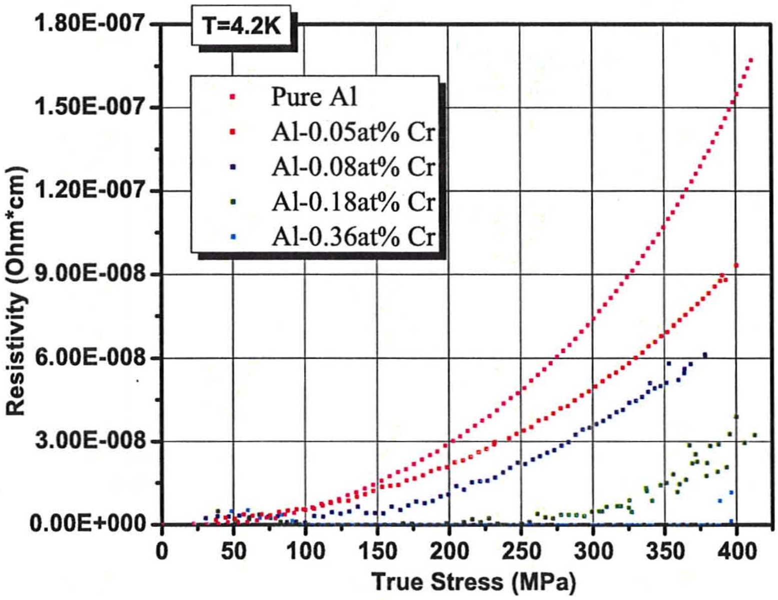

Figure 40: Resistivity vs. Stress data for Recrystallized Al-Cr alloys

In the case of the partially recrystallized samples, seen in Figure 41 and Figure 42, the resistivity data for the Al-0.18at% Cr and Al-0.36at% Cr samples is completely overshadowed by the effects of solute scattering. As with the recrystallized alloys, the resistivities at a given stress or strain decrease with increasing Cr content, and are lower than the pure Al. As with the Al-Mg alloys, both partially recrystallized Al-Cr alloys fail at roughly the same resistivity, although this may be because their compositions are so close, as it is impossible to compare this value to the final resistivities of the higher Cr content alloys. The resistivity of the Al-0.05at% Cr sample appears to rise more slowly as stress and strain increase, compared to the Al-0.08at% Cr alloy, whose rate of increase appears close to that of pure Al.

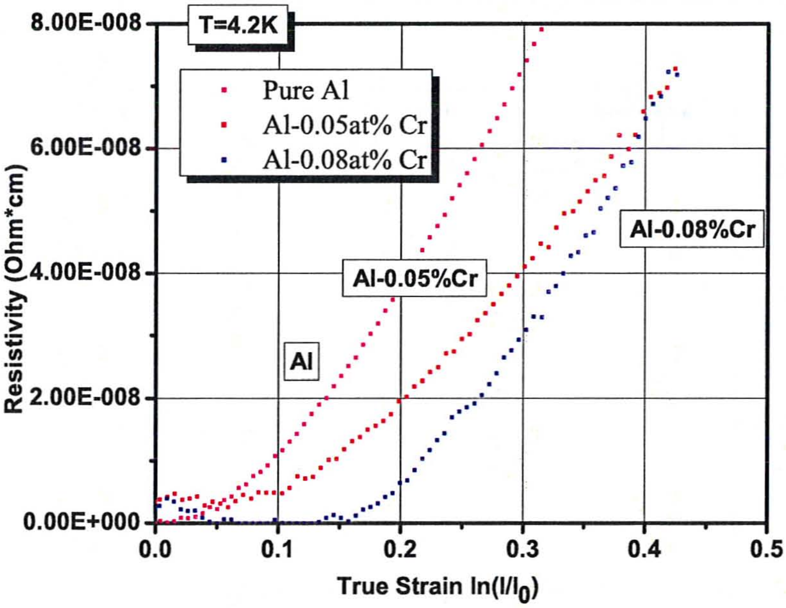

Figure 41: Resistivity vs. Strain data for Partially Recrystallized Al-Cr alloys

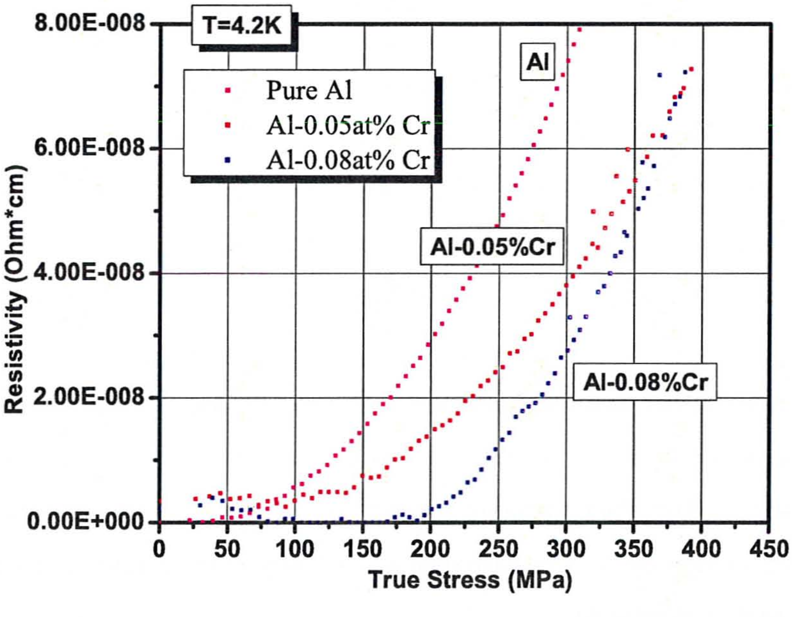

Figure 42: Resistivity vs. Stress data for Partially Recrystallized Al-Cr alloys

3.4 3.4: STRAIN RATE SENSITIVITY

3.4.1 3.4.1: AL-MG SYSTEM

Due to the large instabilities present during the deformation of the Al-Mg alloys at 298K and 4.2K, strain rate sensitivity measurements were only performed at 78K. A Haasen plot created from the stress drops during these strain rate sensitivity measurements is shown in Figure 43, plotting $\Delta\sigma/T\Delta\ln\varepsilon'|_{T,\Sigma}$ vs. $(\sigma - \sigma_y)$, where $\Delta\sigma$ is the drop in stress observed as strain rate changed, T is temperature, ε' is the strain rate and Σ is a structural factor, while $(\sigma - \sigma_y)$ is the stress observed immediately before the change in strain rate. The plot represents the change in stress relative to the strain rate changes at a given temperature as a function of the drop in stress of the alloys.

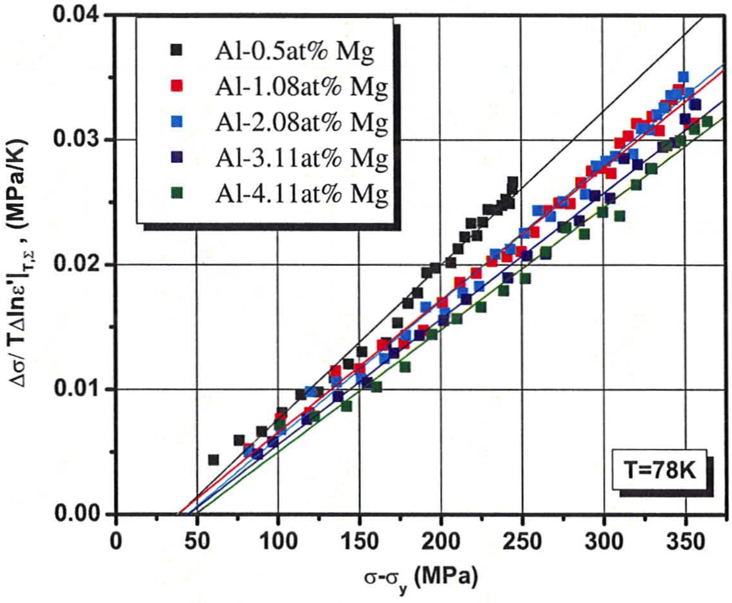

Figure 43: Haasen Plot from Strain Rate Sensitivity Tests for Al-Mg samples at 78K

Figure 43 shows that the slope for each alloy, and thus the Strain Rate Sensitivity, decreases with increasing Mg content, most noticeably as the content increases past 0.5at% Mg.

3.4.2 3.4.2: AL-CR SYSTEM

As the instabilities due to the PLC effect were not present in the Al-Cr samples at room temperature, strain rate sensitivity measurements were performed at both 298K and 78K. The instabilities due to adiabatic shearing at 4.2K, however, made accurate strain rate sensitivity measurements for the Al-Cr alloys impossible at that temperature. Figure 44 shows a Haasen plot similar to that in the previous section for the tests performed at 298K, while Figure 45 shows a plot generated from the 78K results. Again, the drop in stress during the cycle is used as the basis of the calculations in these figures.

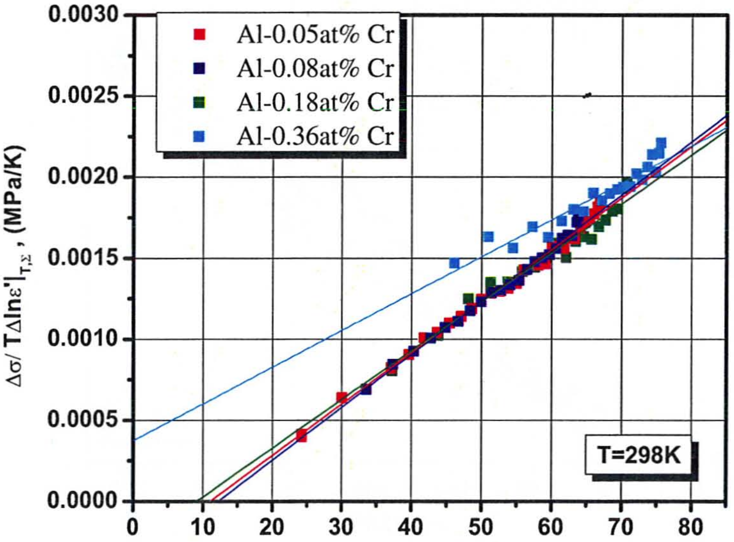

Figure 44: Haasen Plot from Strain Rate Sensitivity Tests for Al-Cr samples at 298K

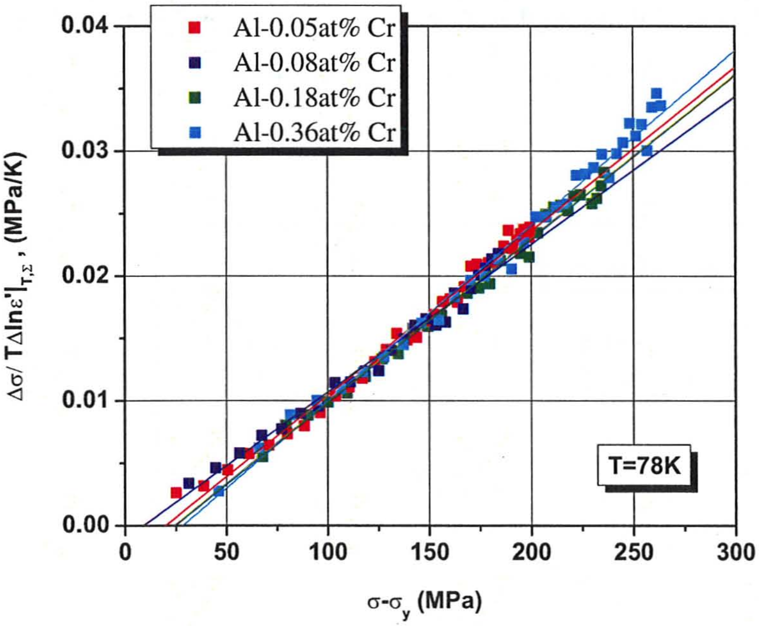

Figure 45: Haasen Plot from Strain Rate Sensitivity Tests for Al-Cr samples at 78K

At 298K in this system, the strain rate sensitivities for the 0.05at% Cr-0.18at% Cr alloys are quite close, with the 0.05at% Cr and 0.08at% Cr samples exhibiting nearly the same sensitivity, though slightly smaller for the 0.08at% Cr. The 0.18at% Cr is slightly more sensitive than the two lower Cr content alloys. The 0.36at% Cr sample exhibits a much higher sensitivity to strain rate, especially at low stress. At high stresses approaching failure, however, the slopes, and thus the sensitivities, appear to converge due to the differences in y-intercept.

At 78K, the sensitivities are far more uniform across the 4 alloys. The intercepts of the 0.18at% Cr and 0.36at% Cr samples are slightly lower than the lower Cr content alloys, and the intercept of the 0.08at% Cr sample is slightly larger than the 0.05at% Cr alloy. In comparing the sensitivities of a given alloy at 298K and 78K, however, significantly higher sensitivities to strain rate are observed at 78K. Also, while there is a drop observed between 0.05at% Cr and 0.08at% Cr, the remaining samples show an increase in sensitivity with increasing Cr content, as can be seen below comparing Figure 46 with Figure 47.

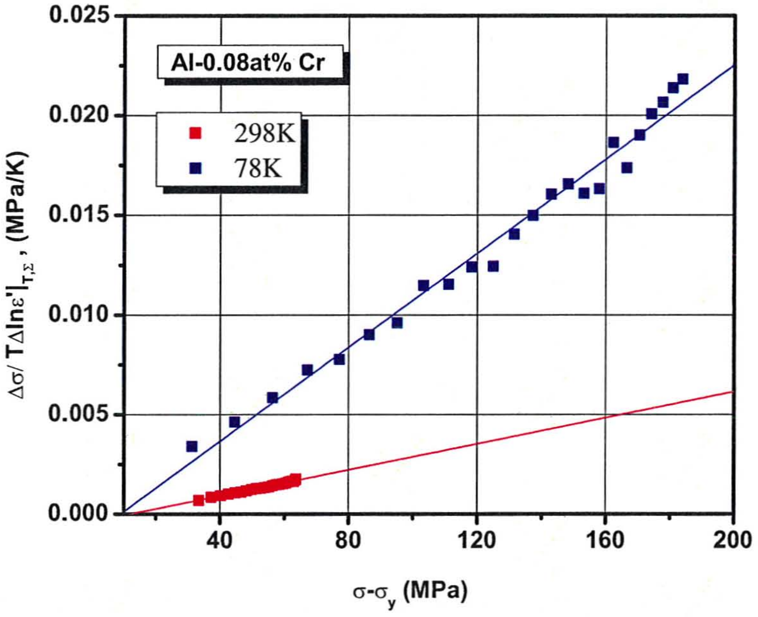

Figure 46: Haasen plot results for strain rate sensitivity tests for Al-0.08at% Cr sample

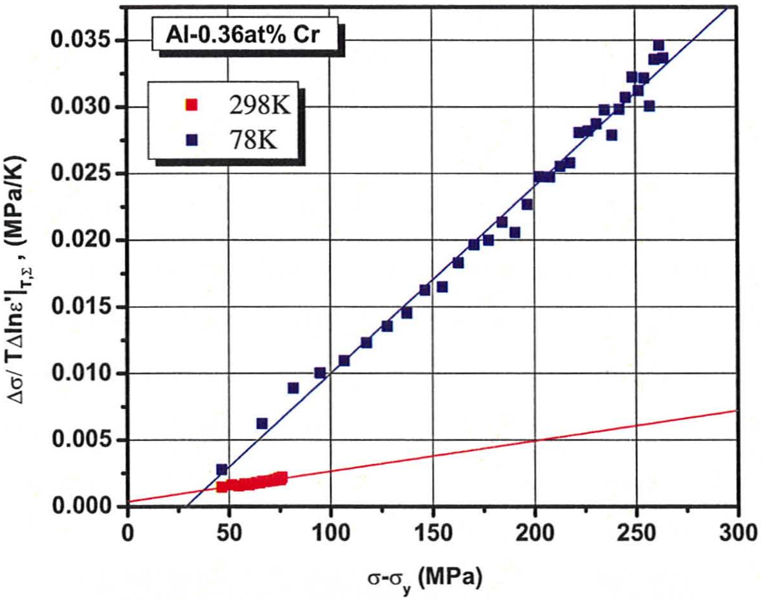

Figure 47: Haasen plot results for strain rate sensitivity tests of Al-0.36at% Cr alloy

3.5 SEM MICROSCOPY

3.5.1 AL-MG SYSTEM

3.5.1.1 FRACTURE SURFACE

SEM observations of the fracture surfaces of selected Al-Mg samples are given in Figure 48 - Figure 65. For the 298K fracture surfaces at low magnification, a heavily dimpled fracture surface indicative of a ductile fracture is clearly visible. In comparing the 0.5at% Mg sample to the 3.11at% Mg and 4.11at% Mg samples, however, the fracture surfaces still show signs of ductile fracture, but the dimpling in the high Mg samples is far finer and more uniform, lacking the large voids observed in the 0.5at% Mg sample. The 4.11at% Mg sample also shows indication of cleavage which points to a fracture mode that is at least partly more brittle.

At higher magnifications, the finer dimpling of the higher Mg content samples is even more apparent. Particles are not readily apparent on the fracture surfaces of the samples, which indicates that particles are not an initiation point for the majority of the dimples, and thus, failure is not dominated by particle presence. In the cases where "particles" are observed at the centre of a dimple, as in Figure 49, EDX analysis indicates the composition of these particles is no different than that of the bulk material.

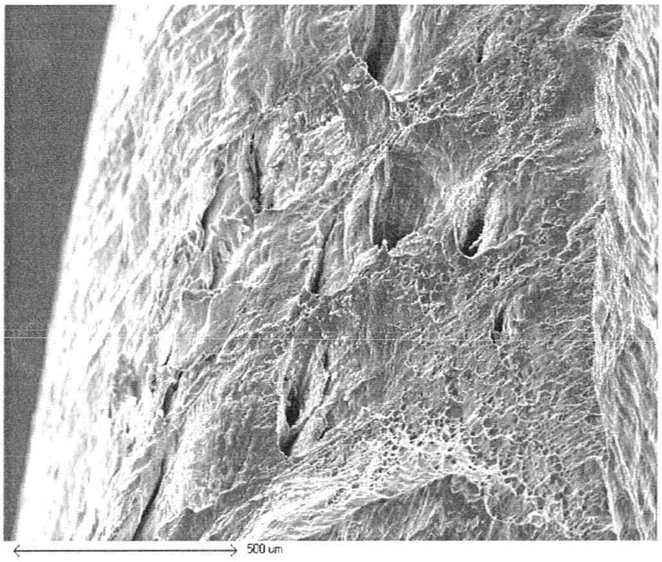

Figure 48: Fracture surface of 0.5at% Mg sample, 298K test, 78x magnification

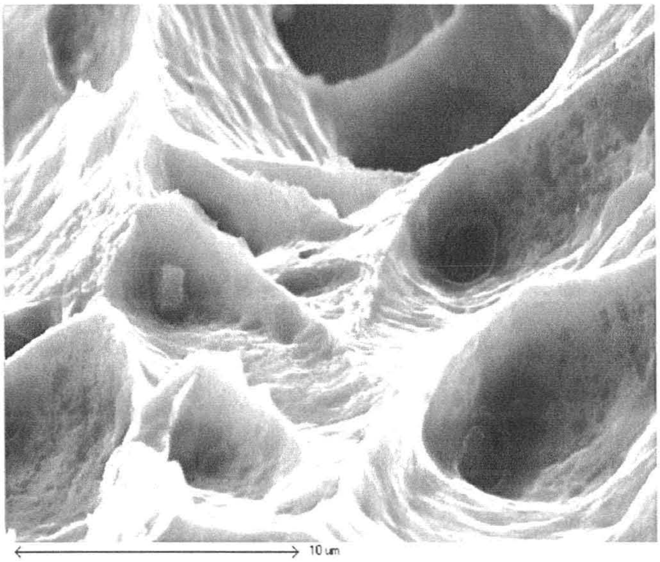

Figure 49: Fracture surface of 0.5at% Mg sample, 298K test, 5000x magnification

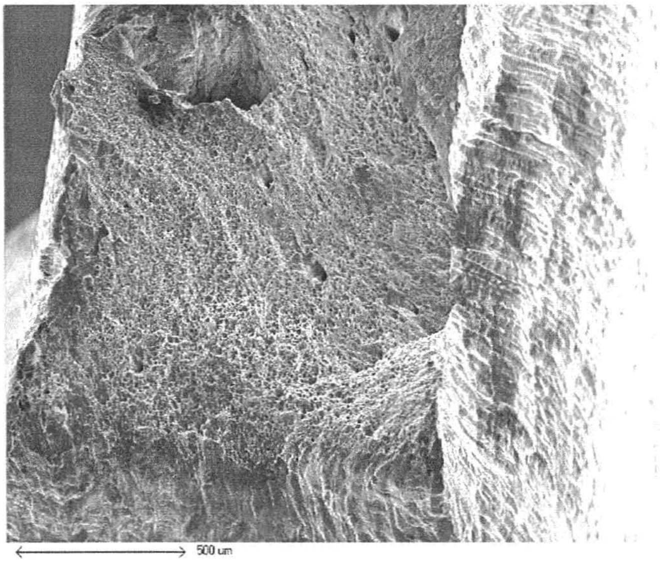

Figure 50: Fracture surface of 3.11at% Mg sample, 298K test, 60x magnification

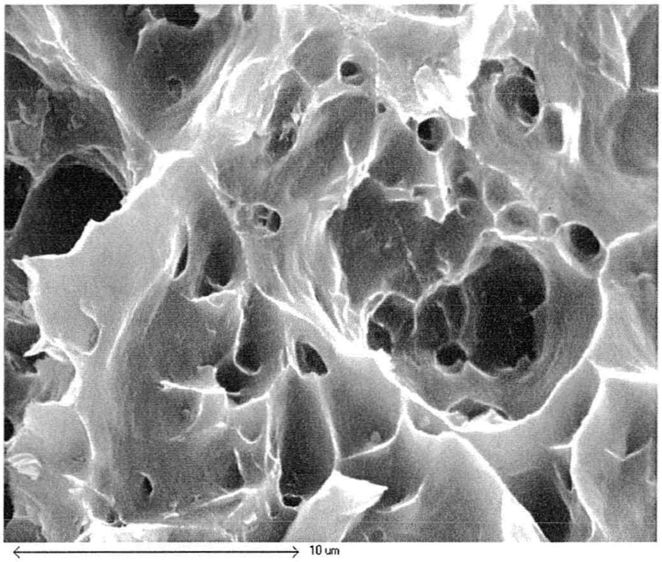

Figure 51: Fracture Surface, 3.11at% Mg, 298K test, 5000x magnification

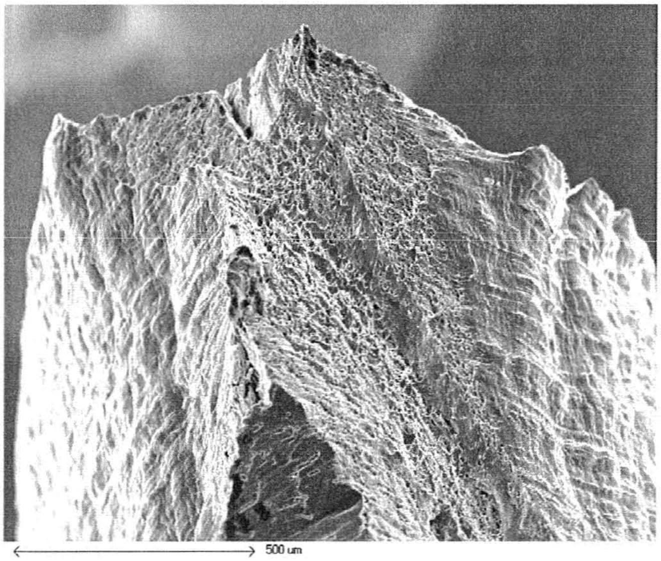

Figure 52: Fracture Surface, 4.11at%Mg sample, 298K test, 85x magnification

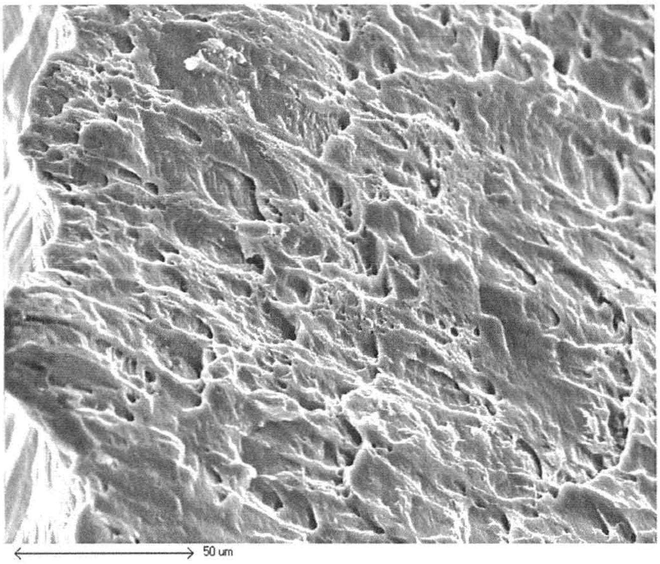

Figure 53: Fracture Surface, 4.11at%Mg alloy, 298K test, 625x magnification

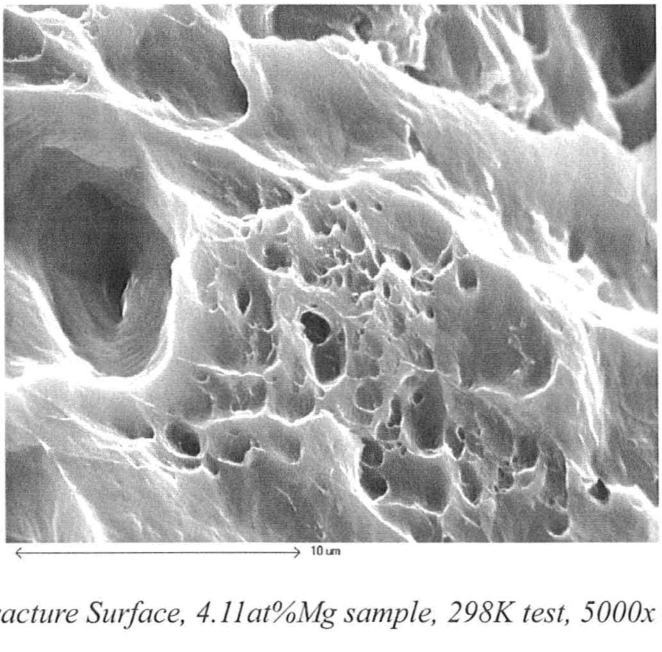

Figure 54: Fracture Surface, 4.11at%Mg sample, 298K test, 5000x magnification

Additional trends become apparent at lower temperatures, shown in figures Figure 55 to Figure 60 for 78K and Figure 61 to Figure 65 for 4.2K. In comparing the fracture surfaces at 298K to the fracture surfaces observed for the same alloys deformed at 78K, the 78K fracture surfaces appear to have a finer surface, with smaller voids, indicative of a less ductile fracture. This is especially apparent in the 0.5at% Mg sample. At higher magnification, this refinement of average dimple size is visible in clearer detail. Crystalline "particles" are again visible in the centres of a few dimples, this time in the 4.11at% Mg sample, seen in Figure 60, and again, EDX analysis indicates the particle has the same composition as the bulk material.

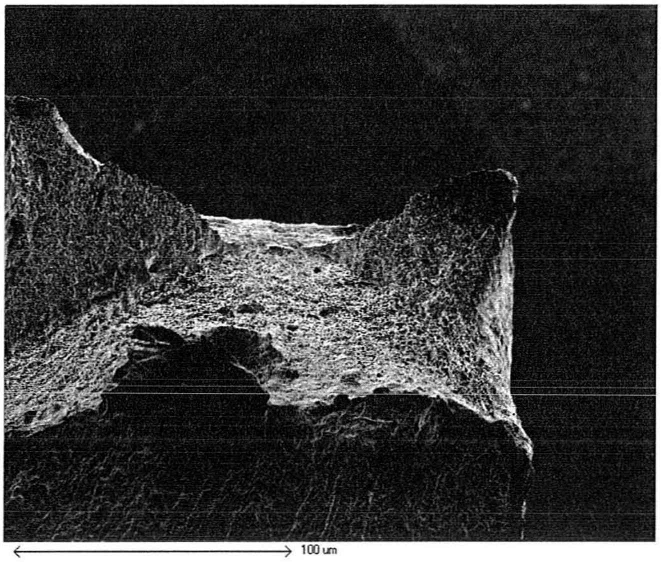

Figure 55: Fracture Surface for 0.5at%Mg sample, 78K test, 48.6x magnification

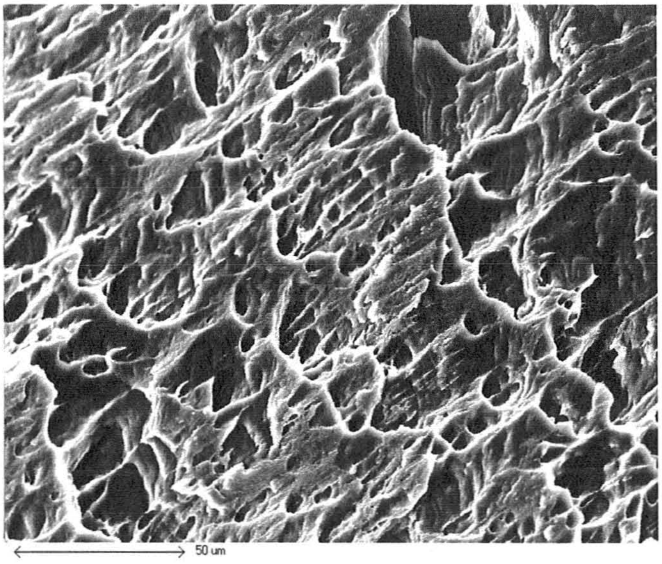

Figure 56: Fracture Surface for 0.5at%Mg sample, 78K test, 600x magnification

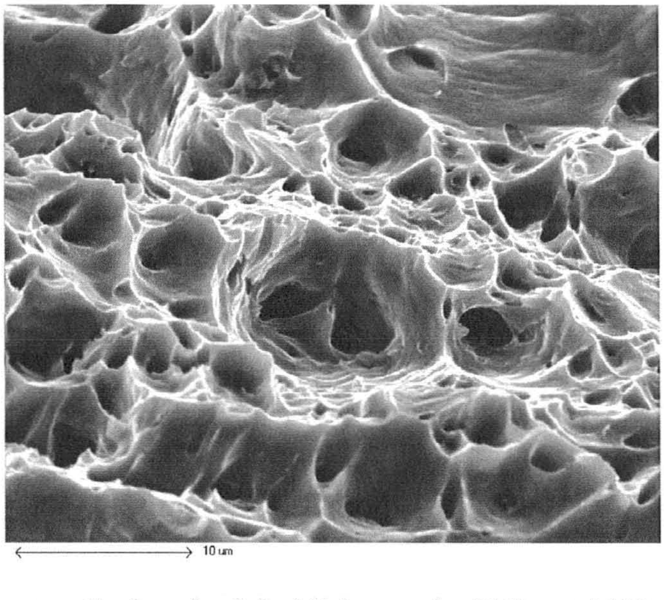

Figure 57: Fracture Surface for 0.5at%Mg sample, 78K test, 3100x magnification

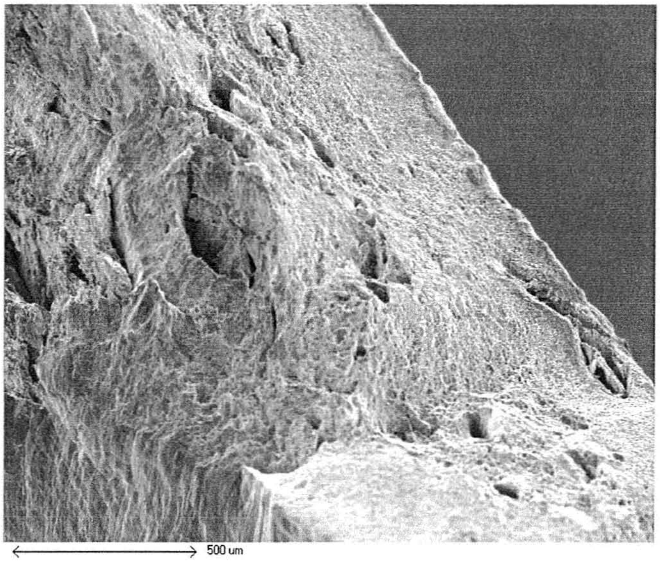

Figure 58: Fracture Surface for 4.11at%Mg sample, 78K test, 65.5x magnification

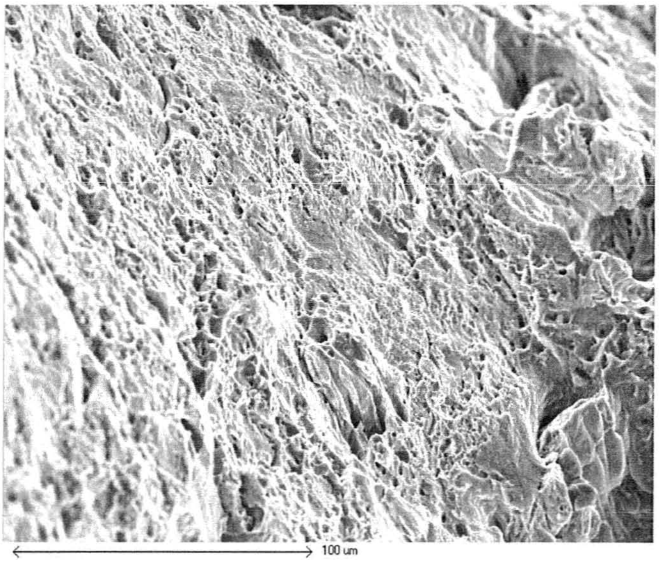

Figure 59: Fracture Surface for 4.11at% Mg sample, 78K test, 526x magnification

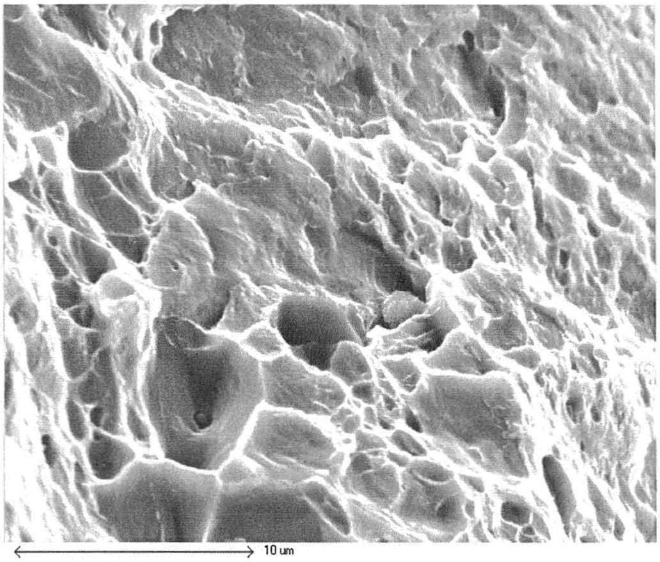

Figure 60: Fracture Surface for 4.11at%Mg sample. 78K test, 4200x magnification

After deformation at 4.2K, the 1.08at% Mg sample shows a fracture surface that appears flatter and with less voids than at higher temperatures, and is shown in Figure 61. At higher magnifications, however, shown in Figure 62 and Figure 63, it becomes apparent that the space between the voids visible at low magnification is filled with a large number of extremely tiny dimples. Some texturing is also visible at higher magnification, which EDX reveals may be caused by the segregation of minor impurities including Fe.

The extremely fine dimpling of the fracture surface is even more apparent in the 4.11at% sample when deformed at 4.2K. As can be observed in Figure 64 and Figure 65, the surfaces are covered with tightly packed, uniform voids between larger dimple features that are too small to be observed with the naked eye. There is almost no space or elongated material visible between these tiny voids, which intersect and nearly overlap each other in places. This fracture surface texture makes EDX analysis impossible, though no particles, precipitates, or other potential initiators of failure were observed.

Figure 61: Fracture Surface for 1.08at% Mg sample, 4.2K test, 44.4x magnification

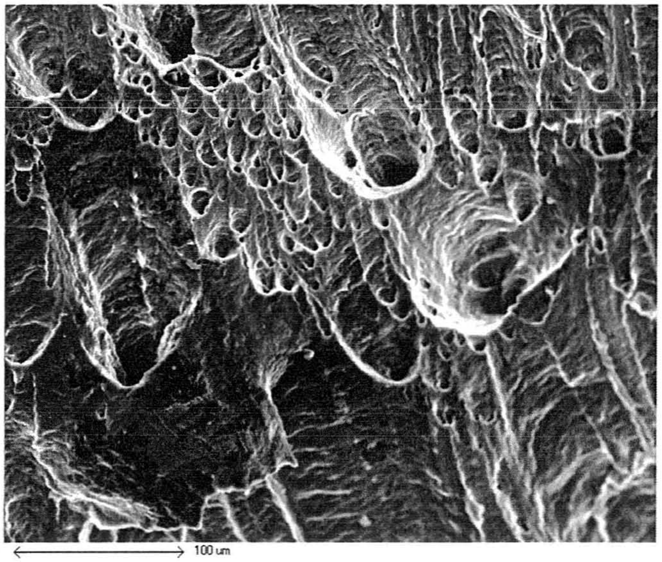

Figure 62: Fracture Surface for 1.08at%Mg sample, 4.2K test, 300x magnification

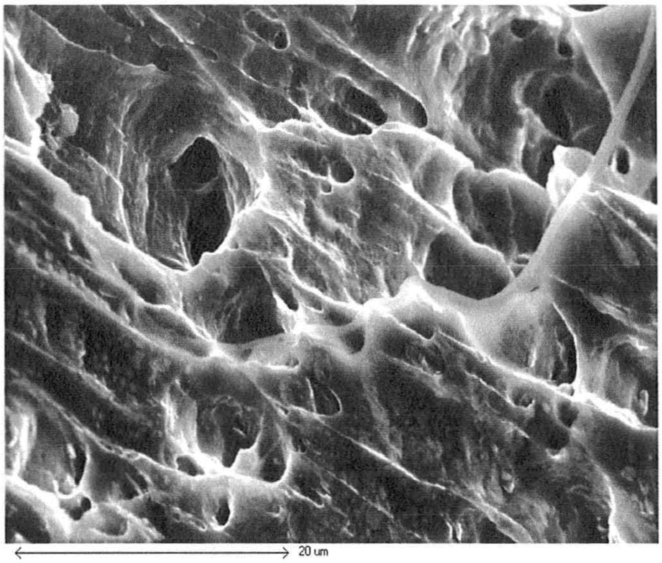

Figure 63: Fracture Surface for 1.08at% Mg sample, 4.2K test, 2400x magnification

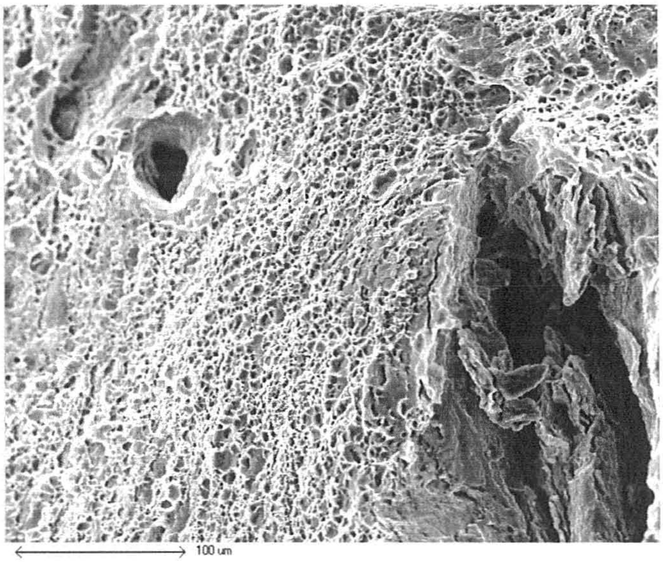

Figure 64: Fracture Surface for 4.11at% Mg sample, 4.2K test, 300x magnification

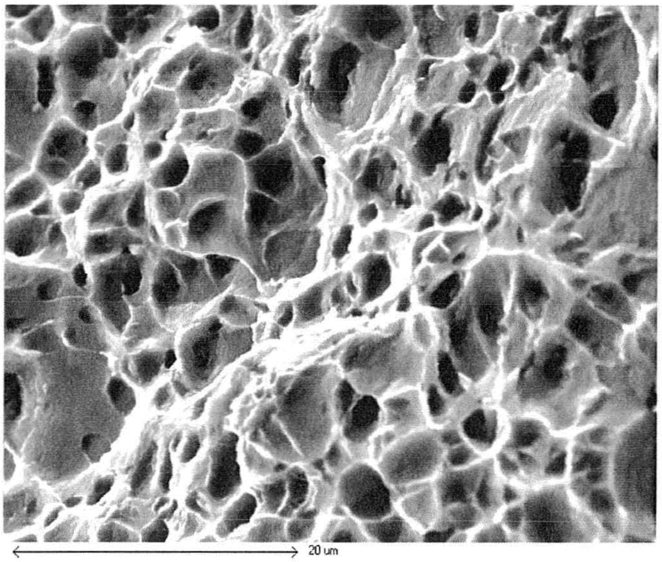

Figure 65: Fracture Surface for 4.11at% Mg sample. 4.2K test, 2500x magnification

3.5.1.2 SIDE PROFILE

As the Al-Mg samples deformed during testing, a surface texture developed, and was observed to be especially rough in the 4.11at% Mg sample, appearing wavy and dimpled to the naked eye. The 298K test sample of the 4.11at% Mg was placed in the SEM microscope along its side, and is shown in Figure 66. The striations on the surface are visible even at low magnifications, running parallel to the tensile direction, and as magnification is increased, more detailed, finer striations are visible within these bands. These bands appear to run between grains for the most part, but regions of mismatched grains occur, showing no bands in their interiors, and appearing to have no effect on the band patterns in the grains around them. These misoriented grains are most prevalent close to the edge of the sample, and EDX analysis shows no difference in their composition compared to the area around them.

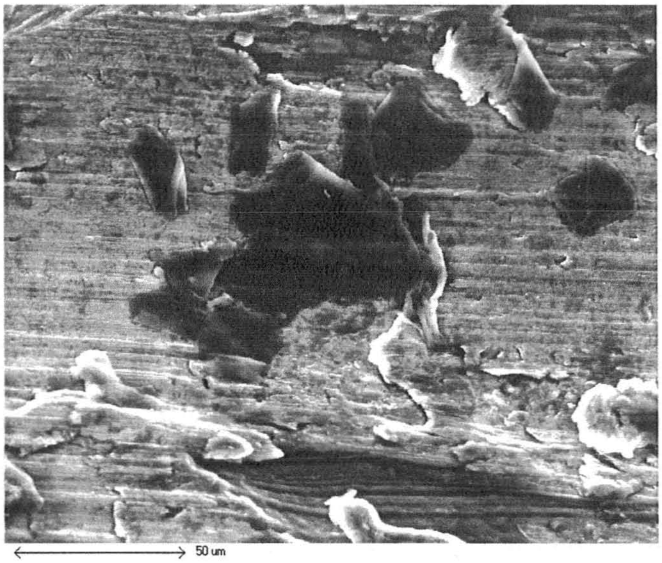

Figure 66: Side Profile, 4.11at% Mg deformed sample, 298K test, 600x magnification

At 78K, surface textures, much like fracture surfaces, are finer. In the 0.5at% Mg sample, the same type of bands parallel to the tensile direction as in the 298K samples are visible, shown in Figure 67. These bands again move across the surface independent of most features, though some mismatched grains are visible. It is possible these bands are texture patterns from the machining process, but there are, however, zones of bands moving roughly perpendicular to the tensile direction. These cross-bands do not cover the entirety of the surface, but the different zones appear to run nearly parallel to each other. These cross-bands, however, appear to be more affected by surface topography, rounding in some areas.

The 4.11at% Mg sample deformed at 78K displays a surface texture much finer than at 298K. The visible bands, however, do not run parallel to the tensile direction, but at an angle to it in two different directions, that come together to form a line of chevrons pointing towards the fracture. These chevrons are visible in Figure 68, as is the line of large horizontal voids where the chevron lines intersect. Much as with the other bands, at higher magnifications the chevrons are resolved into zones of even finer chevrons, and at high magnifications, extremely fine cracks are visible in many of these chevrons, as in Figure 69. Particles are visible on the surface, containing levels of solute/impurities as high as 5.32at%Si, 4.06at%Mg, and 1.53at%K, according to EDX measurements. These particles do not appear to act as initiation points for the formation of either type of crack, however.

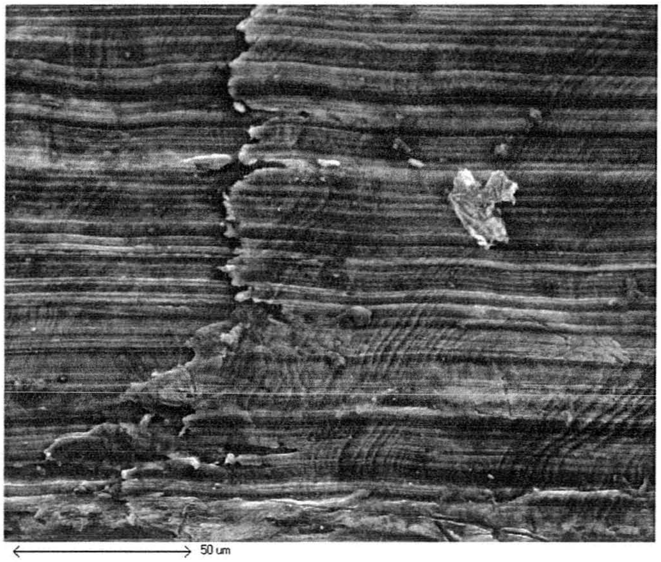

Figure 67: Side Profile for 0.5at% Mg deformed sample, 78K test, 625x magnification

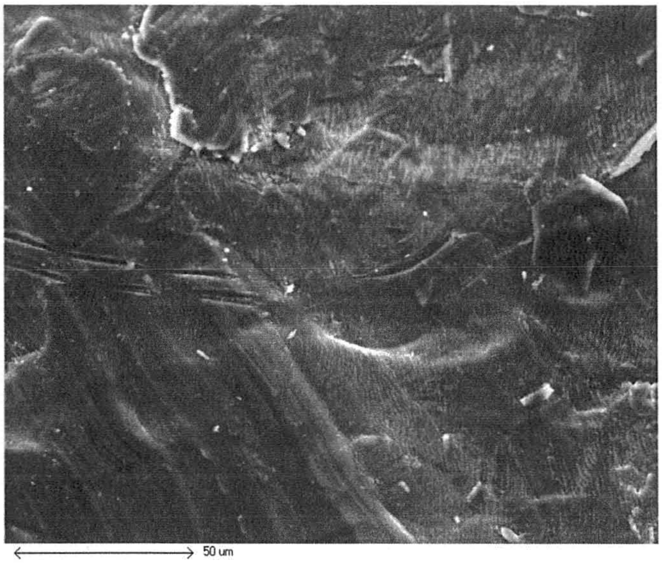

Figure 68: Side Profile for 4.11at%Mg deformed sample, 78K test, 625x magnification

Figure 69: Side Profile for 4.11at%Mg deformed sample, 78K test, 5000x magnification

3.5.2 AL-CR SYSTEM

Comparing the fracture surface of the fully recrystallized 0.36at% Cr sample deformed at 4.2K to the Al-Mg samples, the fracture surface appears coarser, with numerous large voids, as seen in Figure 70. Upon higher magnification, the surface appears most similar to that of the 1.08at% Mg sample deformed at 4.2K, with the majority of the surface between the larger voids being covered by zones of tiny, densely packed voids, as seen in Figure 71. Figure 72, however, shows these tiny voids are much larger than in the Al-Mg samples, and as in the Al-Mg samples, a few of the voids appear to have some particle at their centre. As the 0.36at% Cr sample is slightly outside the solubility limit, this may be a precipitate or impurity, as EDX results were inconsistent and inconclusive. Still, the particles seemed to indicate a higher level of Cr than present in the bulk material, though as these voids are much smaller than others in the same area with no visible particles it is unlikely that the particles contribute heavily towards the failure of the sample.

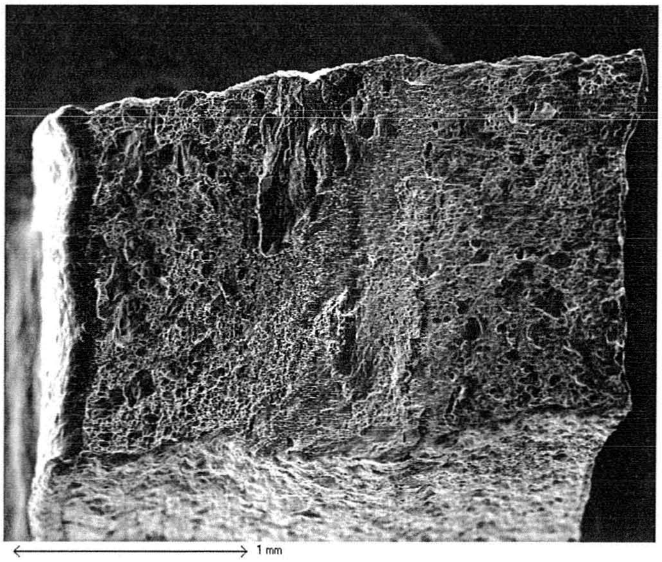

Figure 70: Fracture Surface of 0.36at% Cr sample, 4.2K, 40.8x magnification

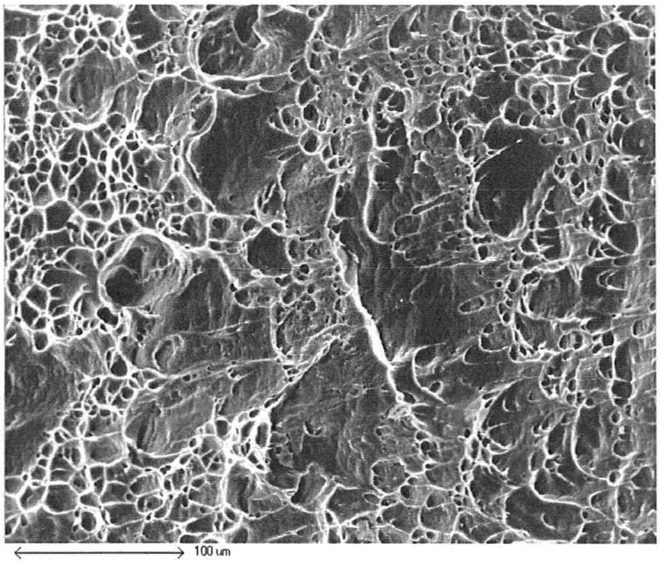

Figure 71: Fracture Surface for 0.36at% Cr sample, 4.2K test, 300x magnification

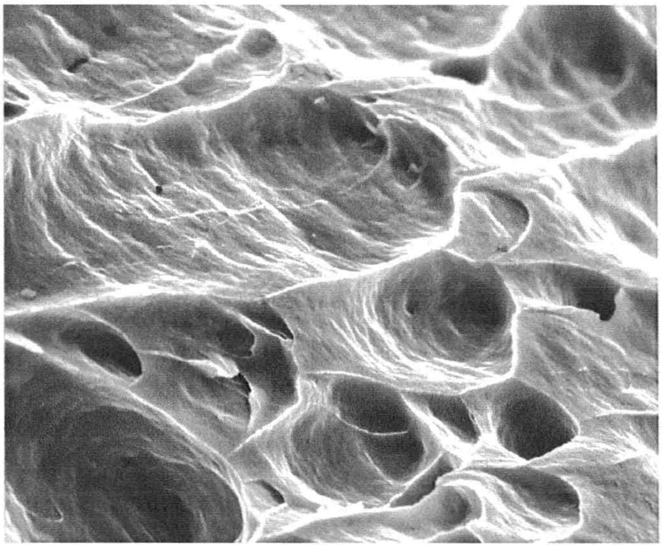

Figure 72: Fracture Surface for 0.36at% Cr sample, 4.2K test, 2500x magnification

3.6 *TEM ANALYSIS*

3.6.1 AL-MG SYSTEM

3.6.1.1 MICROSTRUCTURE

The highest Mg content alloy, the Al-4.11at% Mg sample set, was prepared and observed under TEM microscopy. In the case of the undeformed sample, a fully recrystallized structure was observed, with large, homogenous grains throughout, and no indication of residual directionality. This structure can be seen in Figure 73. Precipitates are present throughout the sample, both inside the grains and along the grain boundary, and there does not appear to be preferential segregation of the precipitates to either area. These precipitates are tiny relative to the grains, around 1.25μm in diameter, and appear to be evenly distributed throughout the sample.

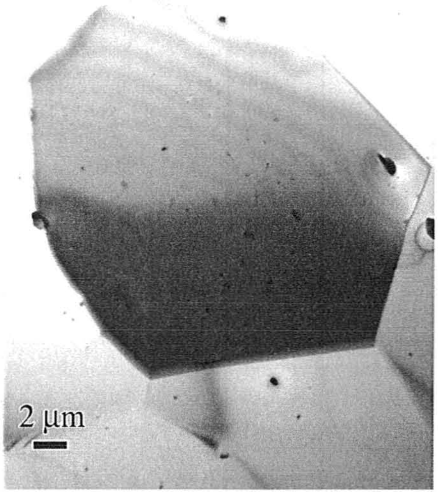

Figure 73: TEM image, Al-4.11at% Mg undeformed sample, 3000x magnification

When the alloy is deformed at 298K, however, the microstructure changes drastically. Figure 74 shows the resulting structure of the Al-4.11at% Mg alloy after deformation, and the evolution of the substructure from the undeformed sample is apparent. As in previous studies of Al-Mg alloys[38], there is significant grain refinement, resulting in a network of subgrains and dislocation cells. After deformation, the subgrains have an average diameter around 0.3μm, more than 100x smaller than the average grain size before deformation. The cell walls appear most deformed, indicating a higher dislocation storage density, though this storage along boundaries appears to be distributed evenly throughout the sample. The cell walls appear chaotic, creating bent and twisting cells with no preferred orientation of the subgrains, parallel to the tensile direction, for example.

At higher magnifications, it is still observed that dislocations appear evenly distributed throughout the sample, with dislocation lines arranged with no preferred direction or location throughout the bulk of the sample. There does, however, appear to be increased dislocation density in the areas around precipitates, as seen in Figure 75. Dislocations are not observed inside the precipitates, but there appears to increased dislocation at the boundaries between precipitates and the alloy, compared to the rest of the matrix. These dislocations appear to arrange themselves in lines and loops perpendicular to this boundary.

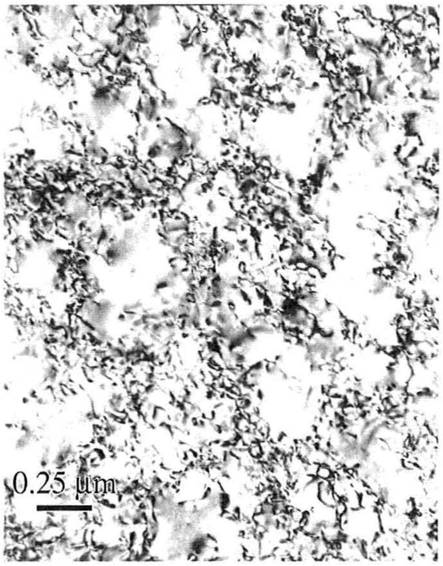

Figure 74: TEM Image, Al-4.11at% Mg 298K sample, 35,000x magnification

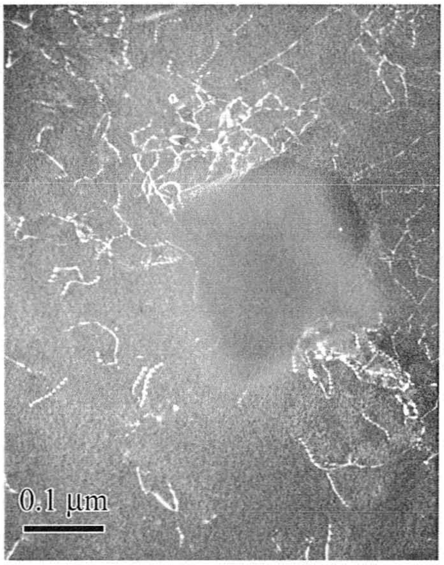

Figure 75: TEM Image, Al-4.11at% Mg 298K sample, 125,000x magnification

When the same alloy is deformed at 78K, the structure re-arranges itself in a different manner. While the Al-4.11at% Mg 78K sample still shows evidence of dynamic recrystallization into a substructure of dislocation cells and cell walls, the end result shows a preferential direction, with elongated cells running in parallel, most likely with the tensile direction. Though overall cell size is slightly larger, on average around 0.5μm thick, tiny subgrains are visible in the marbled texture of the cell walls, as small as 0.1μm in diameter. The cell walls are much thicker, at many places thicker than the cells they surround, and again appear to be more randomly oriented and deformed than the cells. The boundaries with the dislocation cells are more distinct at 78K than at 298K, with less of the apparent diffusion into each other. Precipitates are again visible, and appear segregated to the cell walls throughout the sample.

Observing the cell walls at higher magnification, the cell boundaries are the location where dislocation storage in the 78K sample most occurs. Tightly packed dislocation lines run across the boundary, occasionally branching off or forming loops, as seen in Figure 77. Dislocation lines are present outside of this boundary, and dislocation storage overall appears denser than in the sample of the same alloy deformed at 298K, with additional, longer dislocation lines throughout the image. The dislocation lines outside the boundary run parallel to it, or in some cases, towards it, which is likely another example of the previously mentioned directionality of the microstructure.

Figure 76: TEM Image, Al-4.11at% Mg 78K sample, 13,000x magnification

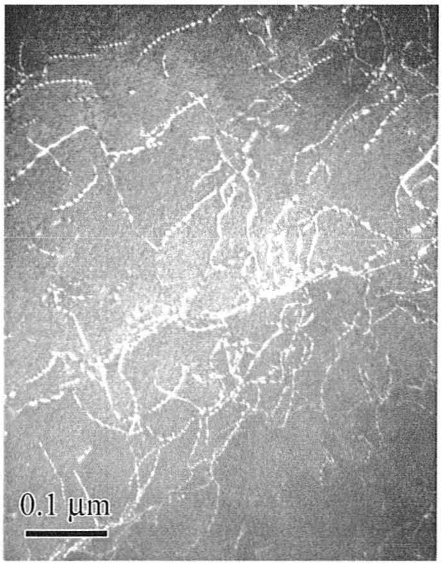

Figure 77: TEM Image, Al-4.11at% Mg 78K sample, 125,000x magnification

The growth of cell walls relative to the dislocation cells themselves is even more apparent when the Al-4.11at% Mg sample is deformed at 4.2K, shown in Figure 78. As in the 78K sample, the elongated cells run in a common direction, but in the 4.2K sample these cells are smaller. Average cell thickness is only around 0.29μm, and the thick cell walls split the cells into several shorter cells, as opposed to the long cells seen when the deformation temperature is 78K. The interiors of the cells appear more deformed than those observed at higher temperatures, and no subgrains are visible. Precipitates are visible, and are evenly dispersed throughout both the cells and cell walls, though they are tiny (an average diameter around 0.1 μm).

Observations of the cell walls at higher magnification show that, when deformed at 4.2K, they remain the primary storage location for dislocations, and store a far higher density of dislocations than observed at higher temperatures. As seen in Figure 79, the dislocations are extremely densely packed, arranging themselves into tight, intersecting loops as small as 0.06μm wide, such that a network of cell-like dislocation loops develops, running through the cell wall. Dislocation lines are also observed inside the cells, and though cell dislocation storage appears denser than at higher temperatures, the dislocation lines and half-loops are small, and seem randomly dispersed and oriented.

Figure 78: TEM image, Al-4.11at% Mg 4.2K sample, 22,000x magnification

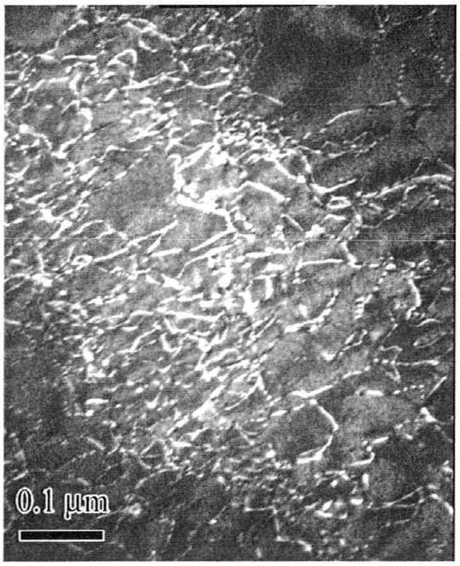

Figure 79: TEM Image, Al-4.11at% Mg 4.2K sample, 125,000x magnification

3.6.1.2 EELS/INCA COMPOSITION

To better determine the composition of the sample at specific locations, additional EDX testing was performed using a JEOL TEM system, the results of which were processed using INCA software. Analysis focused on precipitates observed in the system, in order to properly characterize their composition, and on grain boundaries, to determine if any segregation of solutes was present in the immediate area.

Numerous precipitates of varying shapes are observed during the EDX analysis of the Al-4.11at% Mg alloy, and are present after deformation at 298K and 78K. These precipitates can be classified into two types: Si-O precipitates, and Fe-Ni precipitates. The Si-O precipitates, most likely SiO_2, are more common, and form rectangular or rounded crystals, whereas the Fe-Ni precipitates take the shape of long, needle-like precipitates, and are composed of some Fe-Ni phase, possibly γ, with what appears to be around only 9.5at% Ni content. It also appears that although the Si and Fe impurities remain confined to the precipitates (and likely were never brought into solution during the original casting of the samples, given their melting points), there is Ni in solution throughout the sample, or at least the region surrounding the Fe-Ni precipitates.

Examples of both precipitate types can be seen in Figure 80, and the dotmaps representing the relative compositions of Al, Mg, Si, O, Fe, and Ni can be seen in Figure 81.

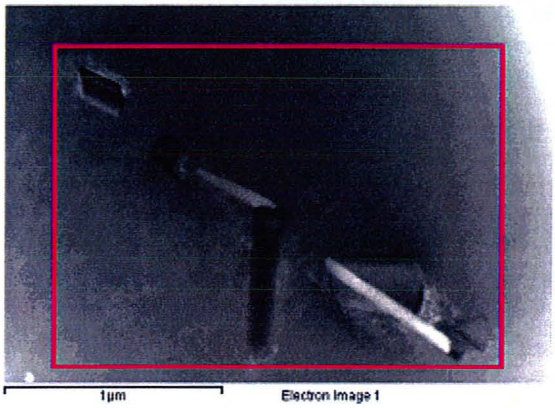

Figure 80: Area of EDX Precipitate Analysis, Al-4.11at% Mg sample, 298K test

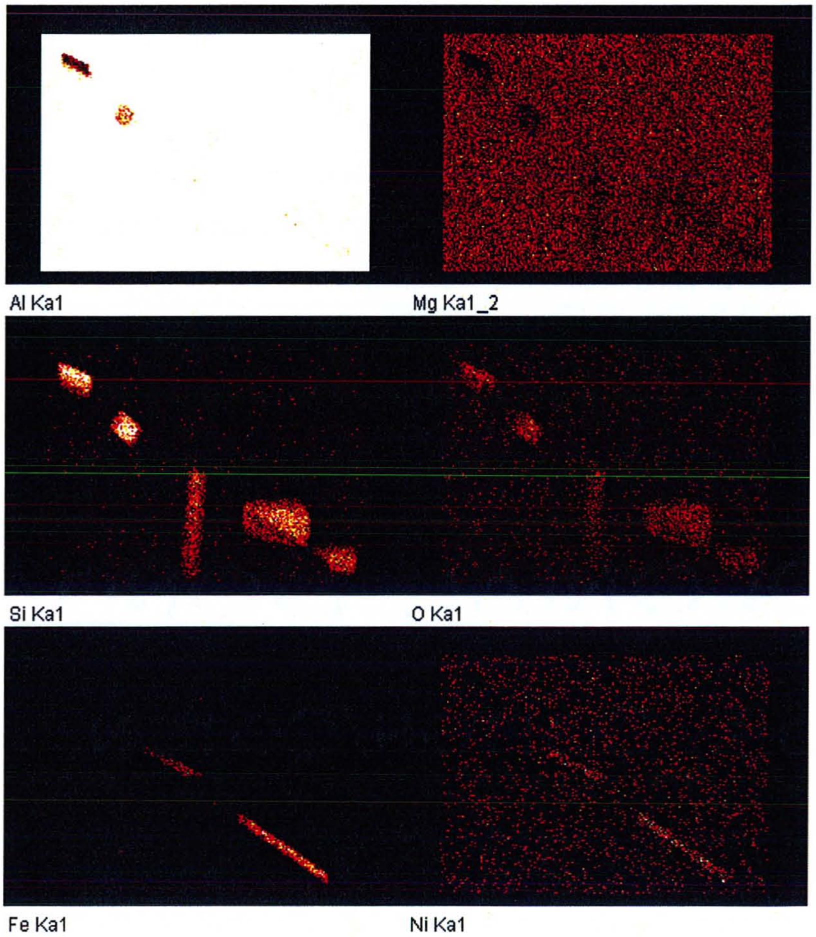

Figure 81: EDX Precipitate Analysis Dotmaps, Al-4.11at% Mg sample, 298K test, Al, Mg, Si, O, Fe, Ni contents

Analysis of the grain boundaries at multiple locations in samples deformed at both 298K and 78K showed no evidence of solute segregation or of any concentration gradient present at the grain boundaries. The relative contents of Al, Mg, and impurities such as O and Si are constant across the grain boundary, as shown in Figure 83, in all observed instances.

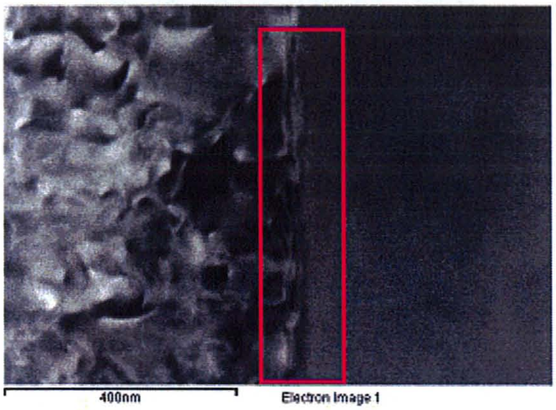

Figure 82: Area of EDX Grain Boundary Analysis, Al-4.11at% Mg sample, 298K test

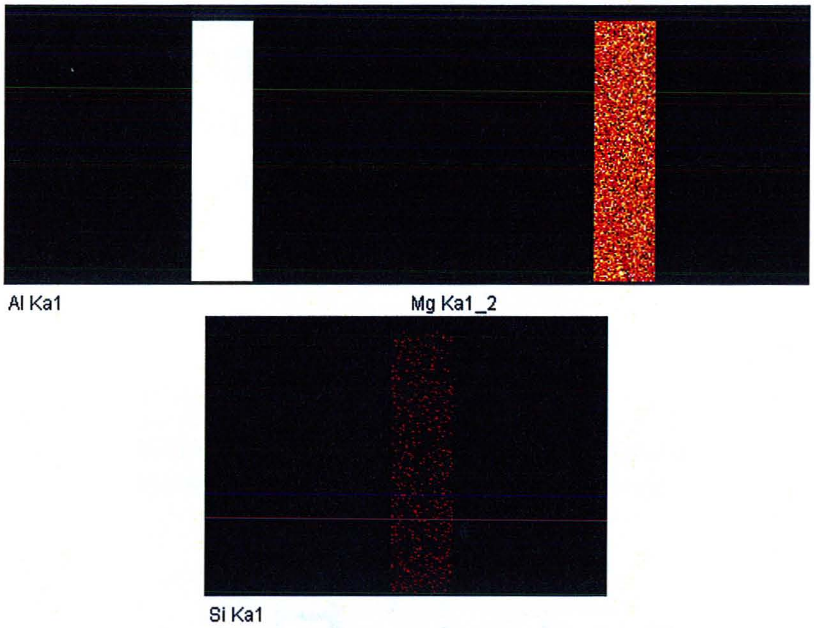

Figure 83: EDX Grain Boundary Analysis Dotmaps, Al-4.11at% Mg sample, 298K test, Al, Mg, Si contents

3.6.2 AL-CR SYSTEM

3.6.2.1 MICROSTRUCTURE

Upon observing the undeformed sample of the Al-0.36at% Cr alloy under TEM, it became apparent that the sample had not been completely recrystallized during annealing. Though there were numerous regions where recrystallization was complete, some areas were composed of numerous grains, on average around 1μm wide, still slightly elongated and aligned with each other as a result of the rolling process. This microstructure can be seen in Figure 84, where two large recrystallized grains intersect with a non-recrystallized region at a triple junction. The recrystallized grains are homogenous, and appear to have similar orientations to surrounding recrystallized grains, unlike the smaller subgrains in the non-recrystallized regions. There are also no precipitates observed in the homogenous interior of the grain, though what appears to be a precipitate will infrequently occur along a grain boundary. Such a precipitate, as well as its effects on the surrounding grains, can be seen in Figure 85, which acts as a visual confirmation of the grain boundary strengthening occurring in the sample. The discovery of these non-recrystallized regions led to the development and testing of the second series of fully recrystallized Al-Cr samples.

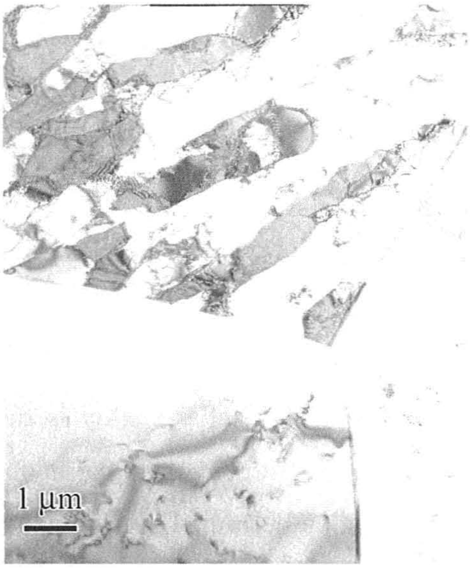

Figure 84: TEM Image, Al-0.36at% Cr undeformed sample, 8,000x magnification

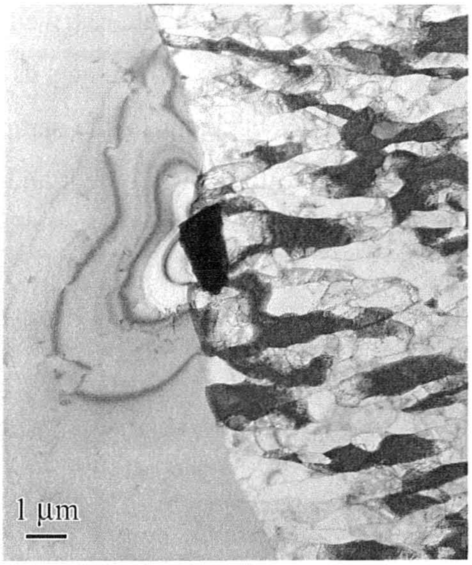

Figure 85: TEM Image, Al-0.36at% Cr undeformed sample, 6,300x magnification

As a fully recrystallized sample of the alloy is deformed at 298K, the resulting structure is significantly different than those observed in the Al-Mg system. Whereas the Al-Mg sample deformed homogenously in all directions at 298K, the Al-0.39at% Cr sample develops a structure of elongated, parallel grain regions instead of dislocation cells, which can be seen in Figure 86. These grain regions represent significant grain refinement compared to the undeformed sample, and are, on average, around 4µm thick. Furthermore, the interiors of these grain regions appear to be composed of networks of small sub-grains, each around 0.4µm in diameter. The regions are separated by thicker grain boundaries than those surrounding the subgrains, and the misorientation between adjoining grain regions would seem to indicate it is likely high energy grain boundaries that separate them.

Focusing on one of these high energy boundaries between two grain regions at a higher magnification, we see that they are the primary storage site for dislocations, as seen in Figure 87. The majority of dislocations are arranged along the boundaries in tightly packed, highly ordered dislocation loops. Though dislocation lines are present inside the grain regions, they are usually limited to a few small dislocation lines, or less dense clusters of dislocations branching off of the grain boundary, as seen in Figure 88.

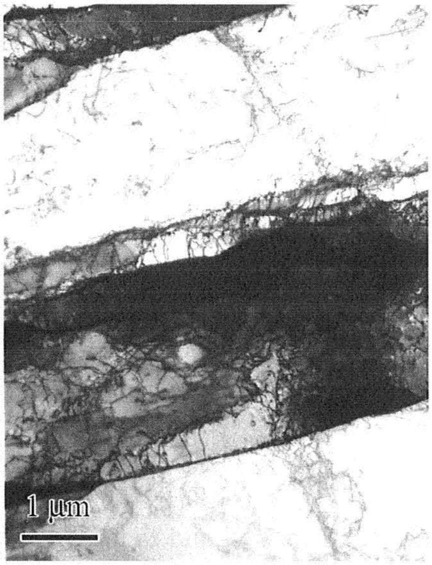

Figure 86: TEM Image, Al-0.36at% Cr 298K sample, 13,000x magnification

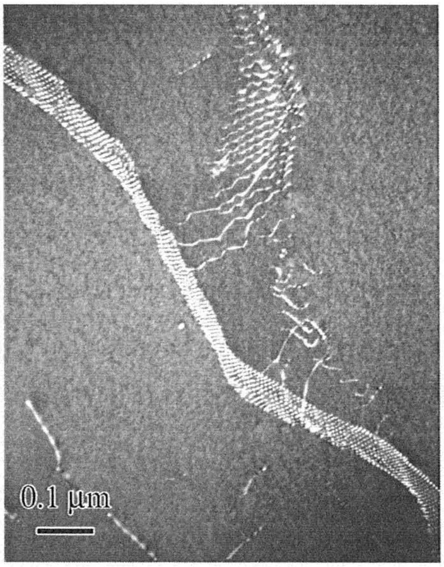

Figure 87: TEM Image, Al-0.36at% Cr 298K sample, 100,000x magnification

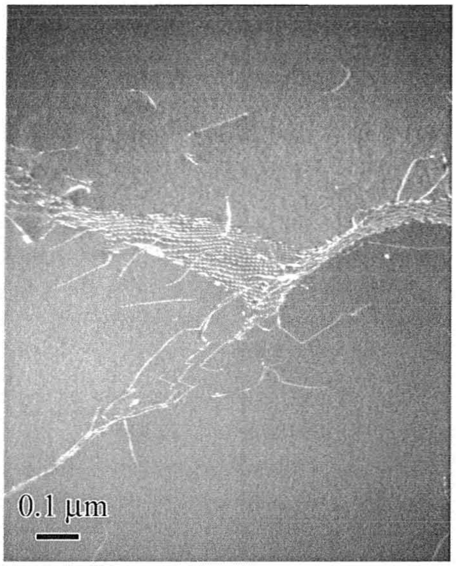

Figure 88: TEM Image, Al-0.36at% Cr 298K sample, 75,000x magnification

When the alloy is cooled to 78K and then deformed, the result is a finer microstructure for the Al-0.39at%Cr alloy. As can be seen in Figure 89, a series of elongated, parallel grains still develop, but they are much thinner, on average 0.4μm thick, a reduction by a factor of 10 compared to the 298K sample. The misorientation between adjoining grains persists, resulting in the same "zebra" pattern, but the separations between grain regions blur into each other at numerous locations, possibly due to the small size. Also of note is that the sample is split into multiple intersecting regions of parallel grains, as opposed to a single region of larger grains, all oriented in the same direction. Subgrains inside the grain regions are still visible, but remain roughly the same size as observed at 298K, meaning a single grain is usually as wide as the entire grain region, as can be seen in Figure 90.

At higher magnifications, there is denser dislocation storage throughout the sample compared to that at 298K, seen in Figure 91. Furthermore, while high-energy boundaries remain the primary storage location, there is increased branching of dislocation lines perpendicular to the boundaries, along with numerous unattached dislocation lines throughout the sample, most running along the same direction as those branching off the boundary. Even the dislocations stored along the boundary arrange themselves into closely packed parallel dislocation lines, each running perpendicular to the direction of the boundary.

Figure 89: TEM Image, Al-0.36at% Cr 78K sample, 17,000x magnification (A)

Figure 90: TEM Image, Al-0.36at% Cr 78K sample, 17,000x magnification (B)

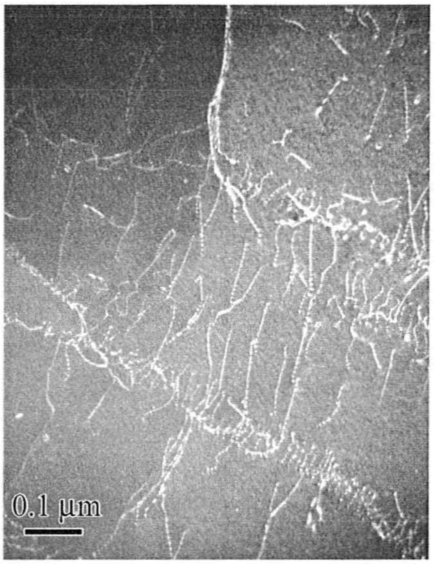

Figure 91: TEM Image, Al-0.36at% Cr 78K sample, 100,000x magnification

Deformation of the same Al-Cr alloy at 4.2K results in similar behavior to that observed at higher temperatures, though the overall structure appears even more deformed. Again, an arrangement of elongated subgrains develop, running in parallel, shown in Figure 92. The average subgrain thickness of around 0.39μm is almost the same as the thickness observed at 78K. Misorientation of adjacent grains seems less drastic than at higher temperatures, indicating the stronger development of preferred orientations, and an alternating deformation texture can be observed across numerous grains. The interiors of the grains regions, seen in Figure 93, seem devoid of further grain refinement, unlike at the higher deformation temperatures, and appear to posess highly discretized, highly deformed boundaries.

Dislocation density is higher than in the previous samples deformed at 298K and 78K throughout the sample, and especially at the boundaries. The boundaries are the main obstacles and primarly location sites for the storage of dislocations, as shown in Figure 94. At this temperature, the alloydevelops a substructure characterized by closely packed dislocation loops, most only around

0.08μm in diameter, connected to each other in a network of intersecting dislocation cells that runs along the boundary. Aside from the boundaries, dislocation lines and occasionally, loops, run throughout the sample, some arranged in seemingly random directions, but most appearing to run in roughly the same direction as the boundary.

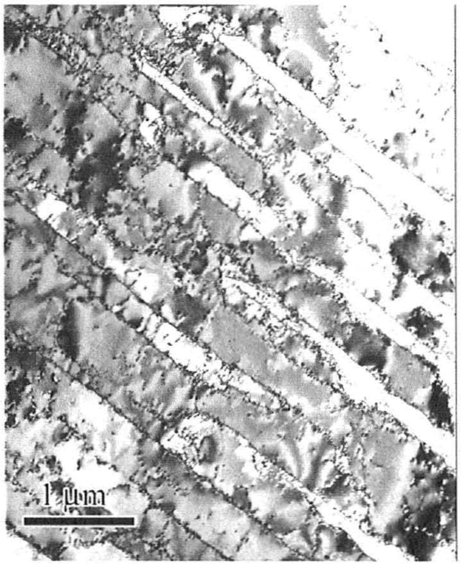

Figure 92: TEM Image, Al-0.36at% Cr 4.2K sample, 17,000x magnification

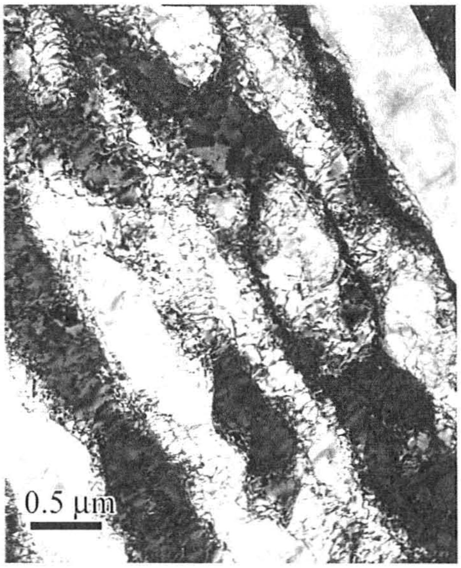

Figure 93: TEM Image, Al-0.36at% Cr, 4.2K sample, 22,000x magnification

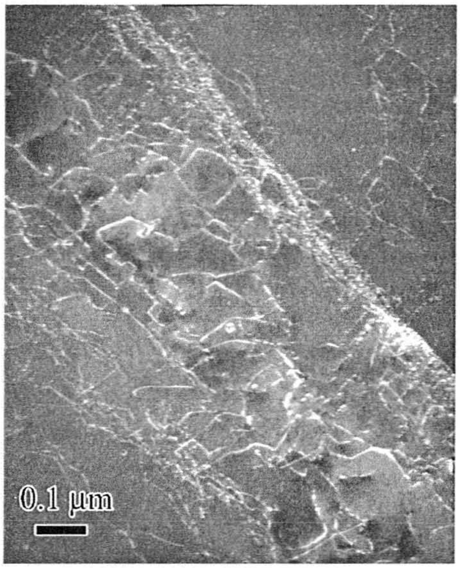

Figure 94: TEM Image, Al-0.36at% Cr, 4.2K sample, 75,000x magnification

3.6.2.2 EELS/INCA COMPOSITION

An undeformed sample of Al-0.36at% Cr alloy was also subjected to EDX analysis in the same manner as the Al-Mg subjects. No precipitates were observed during the analysis (again, verifying their rarity in the microstructre seen during TEM analysis), so analysis focused on grain boundaries, to determine if any concentration gradients were present. As in the Al-Mg system, no such gradients are present, nor is the segregation of any solute materials towards the grain boundaries observed. Impurities such as Si, Ni, and Fe are still present, but are evenly dispersed throughout the area of analysis.

The grain boundary, and the corresponding dotmaps for Al, Cr, and Si can be seen in Figure 96.

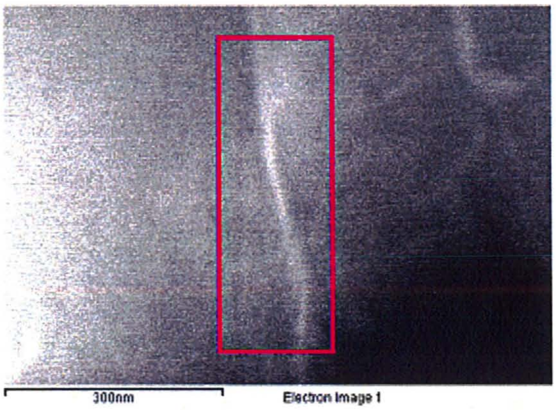

Figure 95: Area of EDX Grain Boundary Analysis, Al-0.36at% Cr undeformed sample

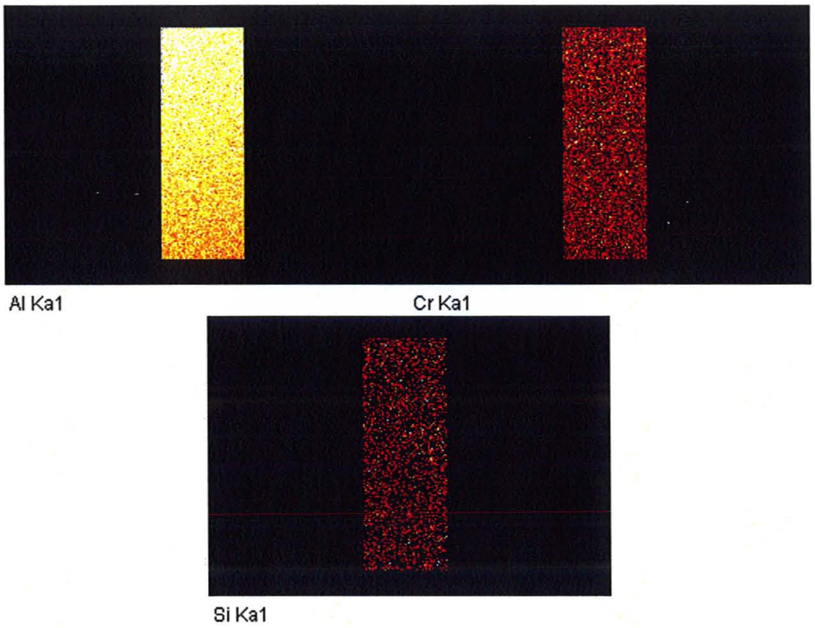

Figure 96: EDX Grain Boundary Analysis Dotmaps, Al-0.36at% Cr undeformed sample, Al, Cr, Si contents

The Al-0.36at% Cr sample was also subjected to EELS analysis, in order to more accurately determine composition, especially in terms of Cr. The analysis, however, was unable to accurately quantify the Cr content of the sample, due to the low levels of Cr, but was able to re-verify that there was no concentration gradient of Cr across or around the grain boundaries.

4 DISCUSSION

4.1 AL-MG SYSTEM

There is a clear increase in the strength of the Al-Mg alloys as the Mg content is increased, visible across all three deformation temperatures in this study. This is understandable, and expected, as the solute strengthening effect of Mg in Al is well documented. The increase in strength likely corresponds to an increased concentration of Mg atoms dissolved into the Al matrix, which then resist the movement of dislocations. It follows that the diminished benefits observed in the Al-4.11at% Mg sample are due to that concentration being outside the single phase boundary for Mg in Al, and thus, the capacity to capitalize on further strength increases through Mg insertion into the matrix has already been exceeded. The precipitates observed in the Al-4.11at% Mg alloy could also contribute to this diminished strengthening compared to earlier increases in Mg content, and though no conclusive evidence was found linking the precipitates to the nucleation of voids during fracture, it is possible that the precipitates weakened the samples in more indirect ways, such as promoting regions of stress concentration, as observed in Figure 75. The strength increases and eventual weakening through Mg addition is also easily visible in the plot of the maximum observed true stress vs. the Mg content of the individual alloys, shown in Figure 11.

In terms of ductility, a similar trend of increases are observed, and can be seen in the form of Figure 97, which shows the elongation before fracture (relative to strain) of the alloys plotted as a function of Mg content. Increases in elongation before fracture are most noticeable at room temperature, and the effect of increasing Mg content appears to become less pronounced as temperature decreases. Across all temperatures, however, the benefit ends once a certain concentration of Mg is reached. At room temperature, no further benefits to ductility are observed after around 2.08at% Mg, after which ductility remains roughly the same as Mg is added. At 78K, the elongation before fracture increases steadily until 3.11at% Mg, at which point it drops sharply. Finally, at 4.2K, ductility remains roughly constant after 1.08at% Mg, rising slightly in the case of the 4.11at% Mg sample. In general, however, the addition of Mg to the pure Al system results in a ductility lower than that of pure Al, most likely by producing locations where solute hardening is more prevalent, leading to failure. This reduction in ductility is mitigated as solute content is increased, in essence evening the effects of hardening over the entire sample and bringing the ductility of the alloy closer to that of pure Al. Once the solubility limit of Mg in Al is reached, however, this homogenization can no longer be realized, and if precipitates are present (as observed during TEM analysis), these could also contribute to the embrittlement of the alloy. It is difficult, however, to determine the exact effects on the ductility of Al-Mg system at 298K and 4.2K, however, due to the plastic instabilities present at these temperatures. It is most likely that these phenomena contribute directly to the failure of the sample, and as their effects are observed to become more dramatic as the alloying content is increased (at both 298K and 4.2K) it becomes increasingly likely that fracture occurs prematurely, obscuring a true picture of the alloy's ductility. This is likely evidenced by the elongation of the alloyed samples being closest to that of pure aluminum at 78K, the temperature where no such instabilities occur.

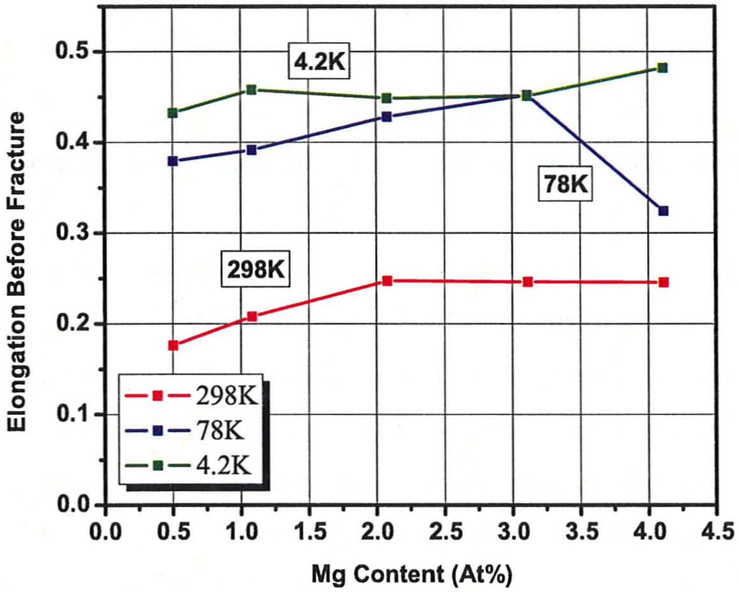

Figure 97: Elongation Before Fracture vs. Mg Content

These plastic instabilities are identical in behavior to those observed in previous studies. At 298K, the instabilities observed in all alloy samples are almost certainly due to the Portevin-Le Chatelier (PLC) effect, more specifically a B-type PLC effect, as the instabilities are characterized by continuous oscillations. These oscillations, readily occurring across the majority of the plastic flow region, match those observed in other Al-Mg alloys[39]. As such oscillations occur when a dislocation core is able to break free from the restriction of its movement due to solute segregation, it is understandable why the amplitude of the oscillations (and thus, the change in plastic flow) increases with Mg content, as there would be a greater concentration of Mg in solution to segregate, and a larger subsequent restriction on dislocation movement to "break free" from. The PLC effect appears suppressed at 78K for all alloys, however, most likely due to insufficient energy for solute segregation at this temperature.

At 4.2K, the instabilities observed are best explained by the presence of adiabatic shearing. Again, the oscillations in load and stress match those observed in previous studies, as does the "pinging" sound accompanying each shearing[40]. The inability of the alloys to effectively dissipate heat generated during deformation by the movement of dislocations leads to localized heating in the sample, which then creates a softer, preferred path for localized shearing. The results indicate that increasing the alloying content of Mg causes this shearing to occur earlier in the deformation, and can also increase the drop in load/stress that coincides with it. This is likely due to a decreased ability in the higher Mg-content alloys to dissipate heat, possibly due to decreased thermal conductivity. As with the PLC effect, the instabilities attributed to adiabatic shearing are not observed in the pure Al sample at 4.2K, indicating, as observed in previous studies, a better dissipation of heat during deformation and slip events.

Due to the instabilities in plastic flow at 298K and 4.2K, it is difficult to accurately analyze work hardening data, as the work hardening data is even more sensitive to these instabilities than the load/stress data. It appears, however, that the Considere criterion is met in tests for each alloy at all temperatures, that is, that work hardening capacity is completely exhausted before fracture occurs. This would indicate that fracture occurs due to necking, which matches not only cursory observations of the fractured samples, but the fracture surface micrographs, which indicate fracture was not particle-stimulated. The amount of necking, obviously, is dependant on the alloying content, as well as temperature. An increase in Mg content is also usually associated with an increase in initial work hardening rate, with the exception of the Al-4.11at% Mg sample at 298K and 78K, and the Al-3.11at% Mg sample at 78K. This is likely due to, in the majority of the samples, the increased amount of Mg present in the matrix acting as a resistor to the movement of dislocations, especially at the beginning stages of the tensile deformation. Once the Mg content of the sample is beyond the maximum solubility in the matrix, Mg-rich areas or precipitates could function instead as a concentrator for dislocations, prematurely hardening areas of the sample.

For the Al-Mg system, the rate of decrease in work hardening appears to be affected only in the higher (>2.08at% Mg) alloys. At 298K, the work hardening factors of the alloy samples and pure Al appear to decrease at roughly the same rate (that is, they have roughly the same slope over the majority of the plastic deformation region), with the exception of the Al-4.11at%Mg sample, whose work hardening appears to decrease at a slightly slower rate, despite its lower initial work hardening rate. This would be indicative of a situation where the addition of Mg to the system has negligible effects on recovery processes occurring dynamically during the deformation, limiting conditions to dislocation/dislocation interaction. It is possible that in the 4.11at%Mg sample, there is sufficient solute that an impact on these dynamic recovery processes does occur, slowing them, and in doing so, slowing the rate at which stresses in the sample are relieved.

At 78K, there are more differences in the observed rate of decrease in work hardening, though some trends are still visible. The two lowest Mg content alloys have a similar rate of decrease to that of the pure Al sample, while the two highest Mg content alloys have similar rates of decrease to each other, but decrease slower than the other samples. The Al-2.08at% Mg sample exhibits work hardening behavior that decreases at a much faster rate than other alloys, despite it having also the highest initial work hardening. It is possible that an error in measurement occurred during the test, as the work hardening characteristics of the Al-2.08at% Mg seem considerably different compared to the other alloys deformed at 78K, as well as tests performed at other temperatures. Still, the other results indicate that the relaxation behavior, and its relationship to solute content, is heavily dependent on temperature. The absence of instabilities such as the PLC effect could also play a role in affecting this behavior. The work hardening results gathered at 4.2K are extremely difficult to gather conclusions from, due to the instabilities due to adiabatic shearing that only grow in magntitude as the deformation continues. Still, it seems that the rate of work hardening decrease, aside from sharp drops due to shearing events, is relatively similar to that of pure Al throughout most of the plastic region. In general, even with the effects of adiabatic shearing, the work hardening of the alloys decreases more slowly at 78K than at 298K, and more slowly at 4.2K than at 78K, which makes sense, as the storage of dislocations is a thermally dependant process.

The stresses at which yielding occurs, relative to the Mg content of the sample and the temperature of deformation, is shown in Figure 98. Across all temperatures, an increase in alloying content corresponds to an increase in the upper yield stress observed at a fairly consistent rate, up until the Al-3.11at% Mg sample. At a higher Mg content, in the Al-4.11at% Mg sample, the same benefits to the yielding behavior of the alloy are no longer observed. At 298K, the upper yield stress decreases compared to the Al-3.11at% Mg sample, at 78K, it is roughly equivalent, and at 4.2K, there is a slight increase. This would indicate, as with maximum overall stress and work hardening, that the benefit of Mg addition, at least within the scope of this study, is limited by the solubility of the Mg within the matrix, and that the strengthening effect resulting from Mg addition takes place not only within the plastic region, but the elastic region as well. The yielding data also indicates that the potential weakening resulting from excess Mg (eg. precipitates) is mitigated more and more at lower and lower temperatures, most likely due to decreased dislocation mobility as temperature decreases,.

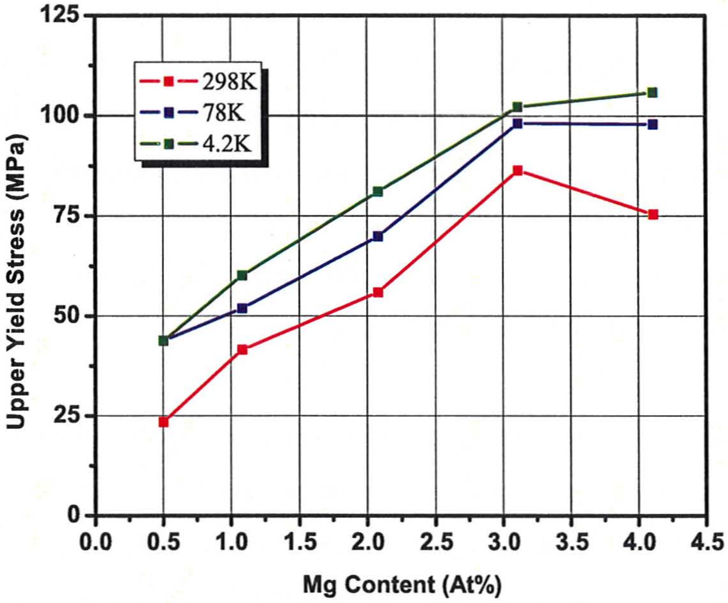

Figure 98: Al-Mg Upper Yield Stress vs. Mg Content

The strain rate sensitivity measurements for the Al-Mg alloys gathered at 78K (the only temperature where such measurements were possible, due to the aforementioned instabilities at 298K and 4.2K) were used to generate Haasen plots as seen in Figure 43. For the purposes of this figure, the strain rate cycle goes from higher stress to lower stress, resulting in rapid drops in flow stress, which form the basis of the creation of the Haasen plot. This figure plots the change in stress observed in each strain rate change "cycle", related to the temperature and the change in strain rate, against the change in stress observed. The slope of the resulting linear fit of the plot is referred to as the strain rate sensitivity (SRS) parameter of each alloy.

The SRS parameters for the alloy decrease as the Mg content increases, but remain close to each other (a spread of ~20% comparing the highest SRS parameter to the lowest). The SRS parameters relative to Mg content are shown in Figure 99, though it is difficult to quantitatively compare the alloys, due to the closeness of the parameters, and the fact that the parameters are drawn from a linear fit, which is easily affected by scattering in the data. Still, the general decrease of SRS as Mg content increases indicates that additional Mg has the effect of increasing the ability of the matrix to resist dislocation movement, at least within the scope of alloys tested in this study. This resistance effectively mitigates the effect of dislocation speed due to strain rate.

It is also possible to determine if there is a thermal component to the flow stress by observing the y-axis intercept for each Haasen plot. At 78K, all of the Al-Mg alloys in this study have negative intercepts, indicating the presence of an athermal component to their dislocation interactions. As the intercepts are roughly equivalent across all alloys (~ -0.0045 MPa/K), it would seem that at this temperature, the athermal component contributes in all observed alloys to a roughly equivalent degree. This athermal component supports the observation of a slight decrease in strain rate sensitivity of the alloys compared to Pure Al at room temperature, where the intercept is essentially zero, and a slight increase compared to Pure Al at 78K, where the intercept is slightly lower than at 298K. As the introduction of solute atoms to the Al matrix imparts a thermal component to flow stresses, the intercepts for the alloys would be expected to be higher than for Pure Al at a given temperature. The near equivalence of the alloy intercepts to pure Al and each other indicate that this thermal component of flow stress is extremely minor, however, and is nearly unaffected by the addition of Mg in or near to the single phase region.

Using the stress rise part of the strain rate cycle yields different intercepts, which are again essentially the same across all alloys (~0.003 MPa/K), but slightly higher and positive. It is likely that this is only due to data scatter, likely because the stress rises occurred after the stress drops, and thus corresponded to a point where the alloy would be slightly harder than when the stress dropped.

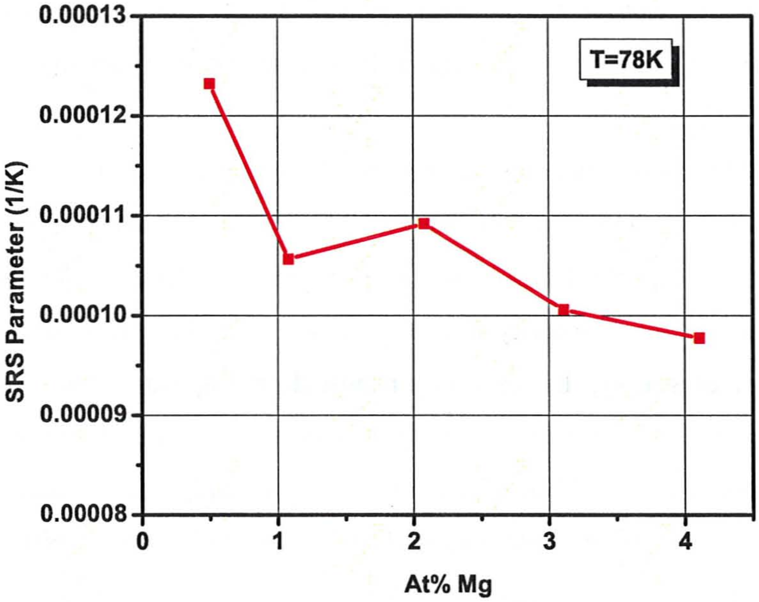

Figure 99: SRS Parameter, Al-Mg alloys, 78K tests

The measurement of electrical resistivity during deformation is a way of indirectly observing dislocation density in the alloys, as a greater density of dislocations in the alloy will provide more deviations in the structure for a current to move across, creating a longer mean free path for an electron, and thus, a higher resistance/resistivity. Relating this to the flow stresses observed at the same time is a way of analyzing the relative strength of the alloy, as higher stresses observed at the same resistivity (and thus, dislocation density) would occur in conditions of more effective dislocation pinning in the structure. For the Al-Mg alloys, excessive scattering limited resistivity data collection to tests at 4.2K only (where phonon-phonon scattering and phonon-electron scattering events were minimized). Still, it is possible to compare resistivity data at this temperature across the range of Mg content covered in this study. Across all alloys (including Pure Al), an addition of Mg results in slower increases in resistance relative to increases in stress, which would correspond to an increase in obstacle strength. Most likely, this is due to solute atoms present in the matrix increasing the dislocation storage capacity, requiring a higher dislocation density at each composition to maintain the same effective stress. At the same time, however, these increased levels of solute atoms increase the phonon scattering that occurs in the material, increasing the scattering observed in the plots of resistivity values, and in the case of the Al-4.11at% Mg alloy, creating a level of "noise" that eclipses the changes in resistivity below a certain level occurring later in the deformation. Interestingly, the resistivity results do not appear to be influenced by the effects of the adiabatic shearing observed using other measurement techniques. Though this could be because resistivity is a parameter insensitive to these macro-scale events, it could also be because the resistivity measurements were recorded less frequently than stress/deformation, and the shearing events were likely rapid enough to go un-noticed at such a scale. Still, it is also worth noting thatall alloys across the 1.08-4.11at% Mg concentration range appear to fail at around the same resistivity, if not at slightly lower resistivities as Mg content is increased. This would indicate a critical dislocation density in the sample at which failure occurs, independent of the obstacle strength of the material. It is possible that this critical density corresponds with the dislocation spacing at which the network collapses due to dislocation annihilation, but additional observation would be required to determine dislocation spacing in the samples. In the case of the Al-0.5at% Mg sample, which fails at a lower resistivity, and thus, dislocation density, it is possible that the solute strengthening effects are insufficient to allow the material to reach the critical density experienced by the other alloys before failing.

SEM observations of the fracture surfaces indicate that for all Al-Mg alloys studied across all 3 temperatures fracture is a ductile process, and is not particle stimulated, even in the highest Mg content alloy. The angled nature of most of the fracture surfaces indicates that crack formation likely begins on one side and travels to the other. This is further evidence of necking as the cause of failure nucleation, as opposed to some particle or instability event. The fracture surfaces grow finer as Mg content increases, with smaller, more numerous voids, indicating an increase in obstacle strength that impedes dislocation movement, preventing the formation of larger voids before fracture. Similarly, the dimpling across the fracture surfaces of all alloys observed becomes finer as temperature is decreased, indicating the increased ability of the structure to resist dislocation motion at lower temperatures. As voids form in areas of high dislocation density, it would seem that as Mg content is increased and/or temperature is decreased, distribution of dislocations throughout the structure is more even, with a finer substructure, providing more sites for dislocation storage, but less mobility for large voids to form. This is indicated by the finer fracture surface, and smaller, more numerous dimpling across the fracture face.

The TEM images from the Al-4.11at% Mg sample agree with the previous statement, as they clearly show a finer substructure at at 78K and then again at 4.2K. Not only does the cell size become smaller as temperature decreases, but the dislocation density (and thus, the storage capacity) also increases significantly, especially in the cell walls. This increased storage capacity and smaller cell size are further explanations for the finer fracture structure observed at cryogenic temperatures. Increased dislocation pinning strength results in more locations of higher dislocation density and a more homogenous distribution of dislocation across the entire surface (and possibly volume) of the sample, especially as the size of the cell wall increases relative to the portion inside it. The cellular substructure observed to develop is analogous to the structures in other Al-Mg alloys in other studies, as is the decrease in cell size with temperature. Like these other alloys, the substructure in the Al-4.11at% Mg alloy shows none of the development of subgrains with low misorientation sub-grain boundaries observed in Pure Al. This is possibly due to the influence of the solute atoms on the stacking fault energy in the system, resulting in the complete change in dislocation substructure.

4.2 AL-CR SYSTEM

As with the Al-Mg alloys, an increase in Cr content in the Al-Cr alloys in this study resulted in increased flow stresses during deformation, and increased strength at the point of failure. However, the overall benefits to the strength resulting from the addition of Cr to the alloys is less than the strength increases observed in the Al-Mg alloys. It is likely that the low solubility of Cr in Al is responsible for this, as it is only possible to introduce a much lower number of Cr atoms into the Al matrix in order to resist dislocation movement. However, in comparing the performance of Cr and Mg as solute strengthening agents, it appears that Cr is as effective as Mg, if not more effective. Comparing the true stress behavior of the highest Cr alloy to that of the lowest Mg alloy (Al-0.36at% Cr compared to Al-0.5at% Mg) at room temperature, the Mg alloy is considerably stronger than the Cr alloy, though this is understandable, as there is still a 25% greater alloying content in the Mg alloy. At the lower temperatures, however, the Cr alloy is as strong, and in the case of the 78K case is stronger than the closest Mg composition alloy. Comparing the change in yield strength relative to the increase in solute levels across the linear regions shown in Figure 98 and Figure 101, shown in it again becomes apparent that Cr is as effective, if not more effective a solute strengthening agent as Mg, especially at 78K. The range across which Cr solute strengthening can be applied, however, is much more limited, and so the overall gains to strength through solute strengthening are much greater in the Al-Mg system.

Table 3: Changes In Yield Strength per at% Solute

Solute	**Temperature**	**Yield Strength Increase / at% (MPa)**
Mg	**298K**	24.11
	78K	15.00
	4.2K	17.17
Cr	**298K**	28.97
	78K	66.34
	4.2K	34.72

As previously mentioned, increasing Cr content leads to increased strength, but the effect seems to diminish as the Cr content increases. Again, once the solubility limit is reached, there appear to be little to no additional benefits in terms of strength from further increases in Cr content, and slight decreases in strength can be observed at lower temperatures. These relative strength benefits in comparison to the Cr added can be seen more clearly in Figure 18, by comparing the maximum true stress observed in each test. As with the Al-Mg system, it is likely that this effect is entirely due to the solute atoms present in the matrix. Precipitation strengthening is negligible in these Al-Cr alloys, as no such precipitates were observed in the recrystallized samples of the Al-0.36at% Cr alloy (the highest Cr content studied), either during SEM analysis of the fracture surface, or during TEM analysis.

All fully recrystallized Al-Cr alloys have higher ductility than pure Al, measured as the amount of elongation before fracture, excepts in samples deformed at 4.2K. At room temperature, ductility increases are observed until the Al-0.08at% Cr composition is reached. At higher Cr contents, ductility decreases, though it remains higher than the pure Al. At 78K, ductility increases as %Cr increases, as with strength, and at 4.2K, aside from the Al-0.05at% Cr sample, ductility never reaches that of pure Al, and decreases once Cr content exceeds 0.18at%.

It is difficult to determine an optimal Cr content in terms of ductility, as the results from different temperatures are inconsistent, as can be seen in the plot of elongation before fracture and Cr content in Figure 100. At room temperature, the optimal composition would be before the solubility limit, somewhere between 0.08-0.18at% Cr, though at 78K, no point is observed where ductility decreases with increasing Cr content. Furthermore, at 4.2K the optimal composition would be somewhere between 0.05-0.08at% Cr. The ductility behavior at 4.2K may tie into the incidence of adiabatic shearing instabilities, which could have led to premature fracture of the alloys compared to pure Al. This would explain why Al-Cr alloy ductility drops below that of pure Al, except for the Al-0.05at% Cr alloy, which showed the least instabilities, and remained more ductile than the pure Al. Comparing the ductility to that of the Al-Mg alloys at room temperature, the Al-Cr alloys all perform better, though this may be in some part due to the absence of PLC effect instabilities in the Al-Cr alloys, but the Al-Cr alloys remain more ductile than the Al-Mg system at 78K, where no such instabilities occur. Even in the non-recrystallized samples, Cr alloys often exhibit similar, or greater ductility than pure Al, except at 4.2K.

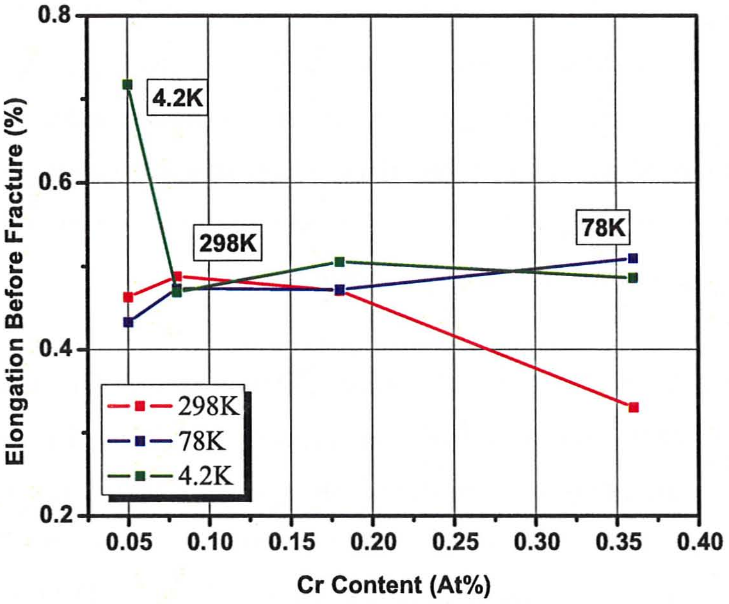

Figure 100: Elongation Before Fracture vs. Cr Content for Recrystallized Alloys

Though instabilities are observed in the Al-Cr samples during testing at 4.2K, no instabilities are observed at room temperature, unlike the PLC effects observed in the Al-Mg system. It is possible that this is to the result of a decreased mobility of the Cr solute atoms due at least in part to their larger size, resulting in an inability to segregate sufficiently to cause resistance to the movement of dislocations. It is also likely that the low levels of Cr content contribute to this inability to effectively restrict the movements of dislocation clusters below the "breakaway" stress, resulting in a more homogenous deformation where the oscillations corresponding to PLC effects are not apparent.

At 4.2K, however, it appears that the instabilities are, indicative of adiabatic shearing, as in the Al-Mg system. The same types of oscillations are observed, as is the acoustic "pinging" that accompanies each load drop. As this process is dependent on the dissipation of heat, rather than solute mobility, it makes sense why similar shearing behavior is observed in both systems, where increased solute content corresponds to earlier shearing, with greater oscillation. As in the Al-Mg system, this is due to decreases in thermal conductivity at 4.2K compared to pure Al as the Cr content rises, which affects the ability of the alloy to dissipate thermal energy released by the dislocation movement and facilitates localized heating followed by adiabatic shearing.

For the Al-Cr alloys, the Considere criterion is met for all tests at all temperatures, meaning the work hardening capacity is exhausted before fracture occurs. This would point to, as in the Al-Mg system, a failure due to necking, corroborated by observations of the fracture surfaces and by the absence of precipitates observed in annealed samples during SEM and TEM analysis. At room temperature, an increase in Cr content corresponds to a steady increase in initial work hardening rate, however at 78K the Al-0.05at% Cr shows a decrease in initial work hardening compared to pure Al, and the highest initial work hardening is exhibited by the Al-0.18at% Cr sample, not the Al-0.36at% Cr sample. At 4.2K, it becomes more difficult to analyze the work hardening results due to the influence of instabilities, but the general trend of increased initial work hardening with increased Cr content is again apparent, with the exception of the Al-0.08at% Cr having lower initial work hardening than the Al-0.05at% Cr sample. As with the Al-Mg system, this trend is likely due to the increased resistance to dislocation movement at the initial deformation caused by the increased solute in the matrix, and again, at 78K it is likely that the solute in excess of the solution point in the Al-0.36at%Cr sample led to some kind of weakening. The remaining results outside of the trends are unlike those observed in the Al-Mg system, but it is possible that the lower initial work hardening in the Al-0.05at% Cr 78K test is due to its large grain size compared to the pure Al, as the work hardening rates of the non-recrystallized Al-0.05at% Cr sample at 78K are far above those of the pure Al. For the Al-0.08at% Cr 4.2K sample, the lower than expected initial work hardening could be due to its larger incidence of adiabatic shearing during deformation compared to the Al-0.05at%Cr sample at 4.2K, and these instabilities could have affected the initial work hardening during the smoothing of the data.

At room temperature, the work hardening values of the Al-Cr alloys (both in the recrystallized and the non-recrystallized cases) appear to decrease at a similar rate to each other during the early deformation of the samples, which is slower than the rate of decrease of pure Al. However, as the Cr alloying content increases, the point at which the rate of change becomes visibly slower (that is, the "peak" of the curve) occurs later and later, and in the case of the Al-0.36at% Cr sample, the work hardening at which the curve suddenly drops at the end of the deformation is higher than observed in previous samples. This situation is indicative of one where the addition of Cr has an effect on the dynamic recovery processes during deformation (unlike the Al-Mg system), and that although the addition of Cr results in higher initial work hardening and work hardening capacity (due to solute strengthening effects), the more alloyed samples are unable to withstand the additional dislocation/dislocation interactions incurred during additional deformation as effectively as the less alloyed samples.

At 78K, the decrease in work hardening occurs more slowly and at a more constant rate across the entire observed deformation as Cr is increased, although the work hardening at which the curve drops to zero increases with Cr content, as at room temperature. Still, this means dynamic recovery is slowed by the addition of Cr at 78K, though the sample "strength" at which lattice collapse occurs becomes higher by this addition. Comparing the rates of decrease at 4.2K is difficult due to the erratic nature of the data, but in general, it appears that, either due to the effects of the solute, or more likely due to the subsequent effects of the adiabatic shearing that occurs, that work hardening decreases more quickly in alloys with increased Cr content. This, as mentioned, can be explained due to the increased levels of adiabatic shearing that occur as Cr content rises. As with the Al-Mg system, work hardening rates decrease more slowly as temperature decreases, due to increased dislocation storage capacity and suppressed dynamic recovery.

Figure 101 shows the upper yield stress for tensile tests performed on the recrystallized samples at each temperature, as a function of the Cr content in each alloy. As with the Al-Mg alloys studied, there is a clear increase in yield stress at all temperatures as Cr content increases (with the only exception being the Al-0.05at% Cr sample at 78K). At all three temperatures, the increase in yield stress is more or less linear, with the 0.05at% Cr sample showing a lower yield strength than the trend at 78K, and a much higher yield strength than the trend at 4.2K. At each temperature, no clear limit to yield stress in terms of Cr content is observed, at least within or around the single phase solubility limit. At 298K, there appears to be a slight decrease in the rate of yield strength increase after the 0.18at% Cr sample, but further testing in this region would be required to make a conclusive statement. Thus, it is difficult to conclusively determine if an optimal composition in terms of yield stress occurs within the scope of this study, but solute strengthening does occur in the elastic region (before the Young's Modulus is observed), as well as the plastic region. As yielding in the Al-Cr alloys is a more gradual process than the discrete yielding observed in the Al-Mg alloys, it is possible that the use of an exact yield stress, rather than a range, carries a potential inaccuracy, especially at 78K, but the general trends described here should still hold true.

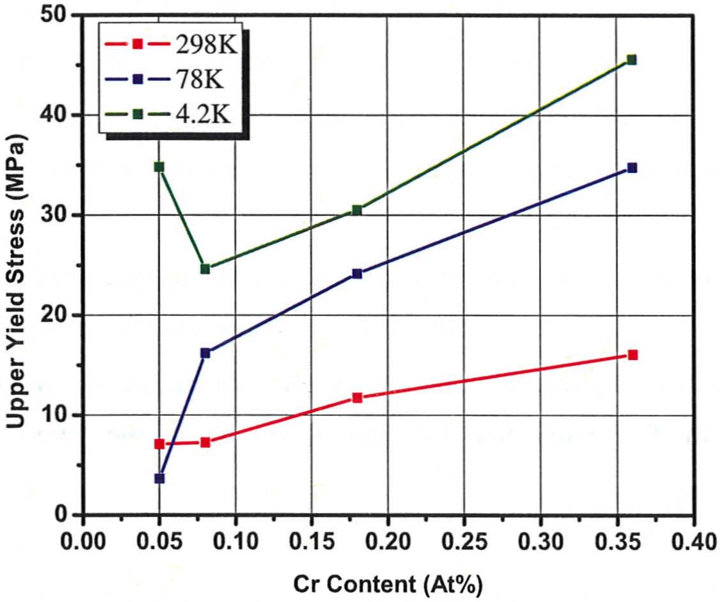

Figure 101: Al-Cr Upper Yield Stress vs. Cr Content For Recrystallized Samples

As the PLC effect instabilities observed at room temperature in the Al-Mg system are not present in the Al-Cr alloys tested in this study, measuring strain rate sensitivity for the Al-Cr alloys was possible at 298K and 78K. Again using the "drop" part of the strain rate change cycle, this data has been collected into Haasen plots as in the Al-Mg system, seen in Figure 44-Figure 47. The collected SRS parameters, collected by temperature relative to Cr content are shown in Figure 102. The results at 78K remain within the same rough range as observed in the Al-Mg alloys, and though a drop in SRS is seen initially as Cr content increases (as in the Al-Mg case), the results differ from the Al-Mg system in that after this initial drop, the SRS steadily increases across the remaining range of samples to levels beyond that of the Al-0.05at% Cr alloy. This trend is reversed at 298K, where an extremely small initial increase is followed by a steady drop in SRS for the remaining two samples.

These trends indicate that in the Al-Cr system at 298K, the addition of Cr to the system can mitigate the effects on stress resulting from a change in strain rate, likely due to the strengthening of the matrix. At 78K, however, the addition of Cr appears to make the alloy more sensitive to changes in strain rate, meaning the matrix may have more difficulty resisting the movement of dislocations as their speed increases. It is likely this is related to a thermally dependent condition, such as solute mobility, as the SRS parameters for all alloys are significantly higher at 78K than at 298K, with the aforementioned change in trend causing the gap between the SRS parameters for each alloy at each temperature to widen as Cr content increases.

The Haasen intercepts of the SRS lines and the resulting correlation to the athermal stress components present in the alloy are all negative at room temperature, but extremely close to 0. This indicates a negligible or athermal component of flow stress due to the addition of Cr compared to pure Al, and this contribution becomes even smaller as Cr content increases. At 78K, however, the intercepts are negative and significantly lower than that of pure Al, decreasing as Cr content increases. This would indicate that the addition of Cr effectively increases the athermal component of flow stress present in the system at that temperature. This is strange, however, as the addition of solute to the Al system should do the opposite, increasing the thermal component of flow stress and, thus, the intercept of the SRS line. More work is required to understand this effect.

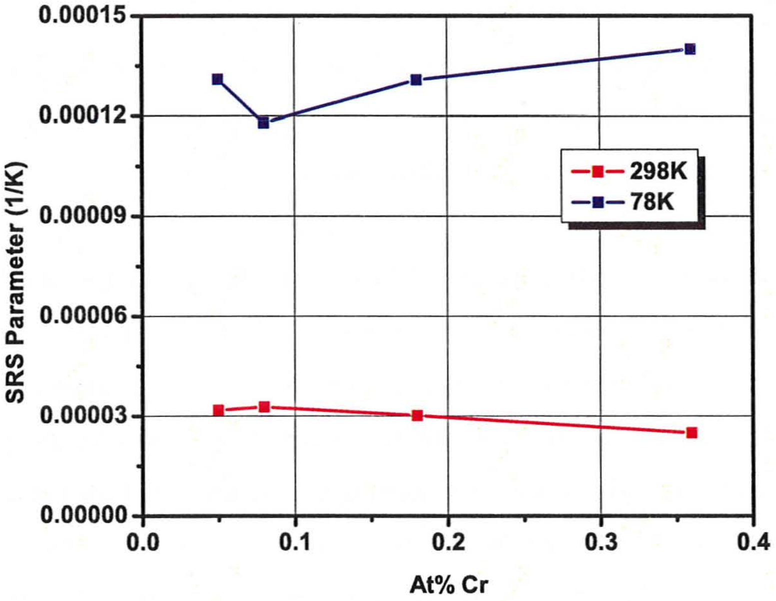

Figure 102: SRS Parameters, Al-Cr tests, 298K & 78K

As in the Al-Mg system, excessive scattering limited the collection of useful resistivity data for the Al-Cr alloys to tests at 4.2K, though additional resistivity measurements were taken during the cooling process of the undeformed samples before the tensile tests for verification. As in the Al-Mg alloys, an increase in alloying content in the Al-Cr system corresponds to a decrease in the rate at which resistance increases relative to stress, and is indicative of an increase in obstacle strength and dislocation storage capacity in the Al-Cr alloys the same way as in the Al-Mg alloys mentioned in previous sections. Unlike the Al-Mg alloys, however, the recrystallized Al-Cr alloys appear to fail at lower and lower resistivity levels as Cr content is increased. This behavior is not observed in the non-recrystallized samples, however, which makes it conceivable that failure is occurring at some critical dislocation density (which would be reflected in the resistivity observed at failure) in the non-recrystallized samples that is dependent on alloying content, though it is difficult to base such a conclusion on only the two alloys where analysis was possible. The complete overshadowing of resistivity change data by scattering "noise" in the two higher Cr alloys of the partially recrystallized sample set could be due to the effects of smaller grain size on the scattering in the material, as solute scattering does not completely eclipse the results in the equivalent fully recrystallized samples.

Fracture surfaces analyzed using SEM point to ductile fracture modes for all Al-Cr alloys across all temperatures, as would be expected in a low-alloyed Al system. Fracture surfaces are angled, often more than in the Al-Mg alloys studied, indicating the crack most likely grows from a wider nucleation site, though the nature of the crack nucleation could be studied using the texture of the material. A tendency towards localization could lead to a build-up of dislocations, and the eventual formation of a larger voids. The dimpling, and lack of particles observed using SEM on the fracture surface, combined with the fracture appearing to originate from the side, point towards failure being due to localized necking, rather than originating from any particle or other feature. Also similar to the Al-Mg samples, finer dimpling is observed as temperature decreases in the Al-Cr alloys. The spacing between dimples shows the increased capacity for dislocation storage as well as the decreased dislocation motion as temperature is lowered. Though the dimpling is seen to grow slightly finer in the higher Cr samples compared to the lower, this difference is not as dramatic as in the Al-Mg samples, most likely due to the much smaller range of Cr content in the Al-Cr samples. The dimpling is also much finer in the non-recrystallized samples compared to the fully recrystallized samples, but this is likely a product of grain structure.

The TEM results for the Al-0.36at% Cr sample show that the substructure is finer as temperature is decreased. Dislocation density increases, as in the Al-4.11at% Mg sample, and dislocations are more evenly distributed across the substructure, though still concentrated at grain boundaries, which are effective obstacles for dislocation movement. In the Al-Cr alloy, however, this more homogenous dislocation distribution appears to be related to subgrain boundaries, rather than the recovered portions of the grain and subgrain interiors. Furthermore, the substructure developed through deformation of the Al-0.36at% Cr alloy differs from that of the Al-Mg alloys. Rather than being defined by a homogenous network of cells, the Al-Cr alloy exhibits a well-developed substructure with highly misoriented, well defined grains, filled with visibly separated, but low misorientation sub-grains, much more closely related to structures observed in pure Al. Whether this similarity to pure Al in terms of substructure is due to the low alloying content of the Al-Cr alloys studied or the effect on stacking fault energy due to the solute atoms, however, is unclear.

5 SUMMARY AND CONCLUSIONS

Solute strengthening is seen to occur in both the Al-Mg and Al-Cr alloys considered in this study. For the Al-Mg alloys, an optimal solution point in terms of mechanical performance is found to occur roughly around the solubility limit of Mg in Al. This is reflected in terms of tensile stresses, elongation before fracture, maximum work hardening and work hardening capacity. For the Al-Cr alloys, such an optimal point is more difficult to determine, and additional testing is required, though mechanical performance does improve with Cr addition through the range of alloys studied, and Cr is observed to be as effective a solution strengthening agent as Mg, though it is only applicable to a much smaller degree due to its low solubility in Al. Adiabatic shearing is seen to occur in both systems when deformed at 4.2K, and these shearing effects are seen to become greater with additional alloying content. Similarly, deformation for alloys in both system at 78K is seen to be homogenous, however at room temperature, the Al-Mg alloys alone exhibit Portevin-LeChatelier type flow instabilities, which also increase in magnitude as Mg content increases.

Electrical resistivity measurements at 4.2K show a decrease in resistivity at a given stress as alloying content is increased, indicating increased contributions to strength from obstacles and lower dislocation density at a given stress. In the Al-Mg alloys, it is possible that failure occurs at a constant critical dislocation density across all alloys, though in the Al-Cr alloys this criticial density may decrease as Cr is added.

TEM observations show a substructure developed through deformation in the Al-Mg alloys that is similar to those observed in previous studies of Al-Mg alloys, and that this substructure is observed to grow finer and distribute dislocations across the substructure more homogenously at lower temperatures. The substructure observed in the Al-Cr alloy, however, is closer to that observed in pure Al, and also grows finer with more evenly distributed dislocations at lower temperatures, though dislocations are stored at subgrain boundaries instead of the recovered interiors of the grains.

BIBLIOGRAPHY

[1] Costlow, Terry. (2008) *Automotive Engineering International.* **116(9)**, 49-50.

[2] Scarmans, Geoff, and Forrest, Helen. (2006) *SAE/UK Vehicle Technology Magazine*. **Summer 2006**, 6-7.

[3] Sakurai, Takeo. (2008) *Kobelco Technology Review*. **28**, 22-28.

[4] Singh, V., Prasad, K.S., Gokhale, A.A. (2004) *J. Mat. Sci*. **39**, 2861-2864.

[5] Nakayama, Y. and Morii, K. (1987) *Acta Metall.* **35(7)**, 1747-1755.

[6] Horvath, Gy, Chinh, N.Q., and Lendvai, J. (2004) *J. Mater. Res*. **20(2)**, 331-337.

[7] Park, Dong-Yeob and Niewczas, Marek. (2008) *Mat. Sci. & Eng A*. **491**, 88-102.

[8] Ronning, Bjorn and Ryum, Nils. (2001) *Metallurgical & Materials Transactions A*. ***32(A)***, 769-776

[9] Soer, Wouter Anthon. (2006). Interactions Between Dislocations and Grain Boundaries. (Doctoral Dissertation, University of Groningen, 2006) Retrieved from http://irs.ub.rub.nl/ppn/290860679

[10] Park, Dong-Yeob. (2007). Plastic Deformation and Work Hardening of Al and AA5754 Al Alloys. (Doctoral Disseration, McMaster University, 2007)

[11] Polmear, I.J (1987) *Mat Sci Forum*. **13-14**, 195-214.

[12] ibid

[13] Vojtech, Dalibor, Michalcova, Alena, Verner, Jan, Serak, Jan, Simancik, Frantisek, Balog, Martin, and Nagy, Juraj. (2008) *Mat Sci Forum*. **567-568**, 197-200.

[14] Polmear, I.J (1987) *Mat Sci Forum*. **13-14**, 195-214.

[15] Datta, S., and Banerjee, M.K. (2000) *Canadian Metallurgical Quarterly*. **39(1)**, 65-72.

[16] Bartels, A., Dimitrov, C., Dimitrov, O., and Dworschak, F. (1982) *J. Phys. F:*

Met. Phys. **12**, 2483-97

[17] Ronning, Bjorn and Ryum, Nils. (2001) *Metallurgical & Materials Transactions A*. ***32(A)***, 769-776

[18] Picu, R.C., Vincze, G., Ozturk, F., Gracio, J.J., Barlat, F., and Maniatty, A.M. (2005) *Mat. Sci & Eng A*. **390**, 334-343.

[19] Casarotto, L., Dierke, H., Tutsch, R., and Neuhauser, H. (2009) *Mat. Sci & Eng A*. **537(1-2)**, 132-140.

[20] Casarotto, L., Dierke, H., Tutsch, R., and Neuhauser, H. (2009) *Mat. Sci & Eng A*. **537(1-2)**, 132-140.

[21] Picu, R.C., Vincze, G., Ozturk, F., Gracio, J.J., Barlat, F., and Maniatty, A.M. (2005) *Mat. Sci & Eng A*. **390**, 334-343.

[22] Wang, S.C., Zhu, Z., and Starink, M.J. (2005) *Journal of Microscopy*. **217(2)**, 174-178

[23] Park, Dong-Yeob. (2007). Plastic Deformation and Work Hardening of Al and AA5754 Al Alloys. (Doctoral Disseration, McMaster University, 2007)

[24] Park, Dong-Yeob. (2007). Plastic Deformation and Work Hardening of Al and AA5754 Al Alloys. (Doctoral Disseration, McMaster University, 2007)

[25] Verdier, M., Brechet, Y. and Guyot, P. (1998) *Acta Mater*. **47(1)**, 127-134.

[26] Picu, R.C., Vincze, G., Ozturk, F., Gracio, J.J., Barlat, F., and Maniatty, A.M. (2005) *Mat. Sci & Eng A*. **390**, 334-343.

[27] Jin, H. and Lloyd, D.J. (2006) *Materials Science Forum*. **519-521**, 161-168.

[28] Park, Dong-Yeob and Niewczas, Marek. (2008) *Materials Science and Engineering A*. **497**, 65-73.

[29] Verdier, M., Breche, Y. and Guyot, P. (1998) *Acta Mater*. **47(1)**, 127-134.

[30] Ioannidis, E.K. and Sheppard, T. (1990) *J. Mat. Sci*. **25**, 2965-3975

[31] Bartels, A., Dimitrov, C., Dimitrov, O., and Dworschak, F. (1982) *J. Phys. F: Met. Phys*. **12**, 2483-2497

[32] Saimoto, S. & Diak, B.J. (2002) *Mater. Sci. Eng.* **A322**, 228-232.

[33] Bull, M.J. & Saimoto, S. *Solute-defect Interactions: Theory and Experiment*, eds. S. Saimoto, G.R. Purdy and G.V. Kidson (Pergamon, Canada 1986) p. 375-381

[34] Saimoto, S., Cao, S. & Mishra, R.K. (2005) *Matls. Sci. Forum.* **475-479**, 421-424.

[35] Diak, B.J., Upadhyaya, K.R., and Saimoto, S. (1998) *Prog. Mat. Sci.* **43**, 223-363.

[36] Park, Dong-Yeob. (2007). Plastic Deformation and Work Hardening of Al and AA5754 Al Alloys. (Doctoral Disseration, McMaster University, 2007)

[37] Park, Dong-Yeob and Niewczas, Marek. (2008) *Materials Science and Engineering A.* **497**, 65-73.

[38] Park, Dong-Yeob. (2007). Plastic Deformation and Work Hardening of Al and AA5754 Al Alloys. (Doctoral Disseration, McMaster University, 2007)

[39] Picu, R.C., Vincze, G., Ozturk, F., Gracio, J.J., Barlat, F., and Maniatty, A.M. (2005) *Mat. Sci & Eng A.* **390**, 334-343.

[40] Park, Dong-Yeob. (2007). Plastic Deformation and Work Hardening of Al and AA5754 Al Alloys. (Doctoral Disseration, McMaster University, 2007)

APPENDIX A – COMPOSITION ANALYSIS RESULTS

Table 4: Al-Mg Alloy Compositional Results

Al-Mg Composition Results					
Alloy Name	**AM1**	**AM2**	**AM3**	**AM4**	**AM5**
Solute Type	Mg	Mg	Mg	Mg	Mg
Approximate Solute Concentration (at%)	0.5	1.08	2.08	3.11	4.11
GDOS Analysis Concentrations (wt%)					
Elements					
Al	99.387	98.8316	97.94	96.9982	96.119
Mg	0.4505	0.972	1.883	2.8087	3.723
Cr	0.003259	0.002986	0.003461	0.003741	0.003127
Si	0	0	0	0	0
Fe	0.058	0.06	0.06361	0.07238	0.05882
Mn	0.00925	0.00932	0.00956	0.01162	0.01011
Sn	0.02344	0.0544	0.0347	0.0232	0.0251
Cu	0.003714	0.004098	0.00378	0.00432	0.00339
Ni	0.0063	0.006712	0.0076	0.00868	0.00678
Ti	0.00711	0.00705	0.00609	0.00626	0.00511
Sr	0.03362	0.02884	0.034153	0.037201	0.0331
Zn	0.0178	0.023	0.014	0.0257	0.0125

Table 5: Al-Cr Alloy Composition Results

Al-Cr Composition Results				
Alloy Name	AC1	AC2	AC3	AC4
Solute Type	Cr	Cr	Cr	Cr
Approximate Solute Concentration (at%)	0.18	0.05	0.08	0.36
ICP Analysis Concentrations (wt%)				
Elements				
Cr	0.358	0.093	0.161	0.653
Si	0.064	0.011	0.015	0.072

APPENDIX B – AL-CR ALLOY ANNEALING AVERAGE GRAIN SIZE MEASUREMENTS

Table 6: Al-Cr Alloy Average Grain Sizes

Average Al-Cr Alloy Grain Size After 10 mins Annealing (in Microns)				
Alloy	AC1	AC2	AC3	AC4
Cr Content (at%)	**0.18**	**0.05**	**0.08**	**0.36**
Temperature (deg C)				
250	8.037	25.785	26.3	22.435
300	43.244	60.733	58.867	23.005
340	100.397	125.996	159.665	107.293
360	135.528	101.771	92.857	198.707
380	68.615	93.74	110.724	105.428
400	118.305	124.278	117.616	87.772
420	116.148	113.119	104.273	130.283

APPENDIX C – COMPLETE TENSILE RESULTS

The following section shows graphs of the tensile results for every alloy tested. Some of these results are also included in the body of this report, but are included here again for completeness. Results are ordered by increasing alloying content, with single-alloy figures before multiple alloy figures, and stress/strain behavior before stress levels, work hardening behavior, strain rate sensitivity, resistance, and resistivity. Al-Mg alloys are placed before Al-Cr alloys, and fully recrystallized Al-Cr alloys are placed before partially recrystallized Al-Cr alloys.

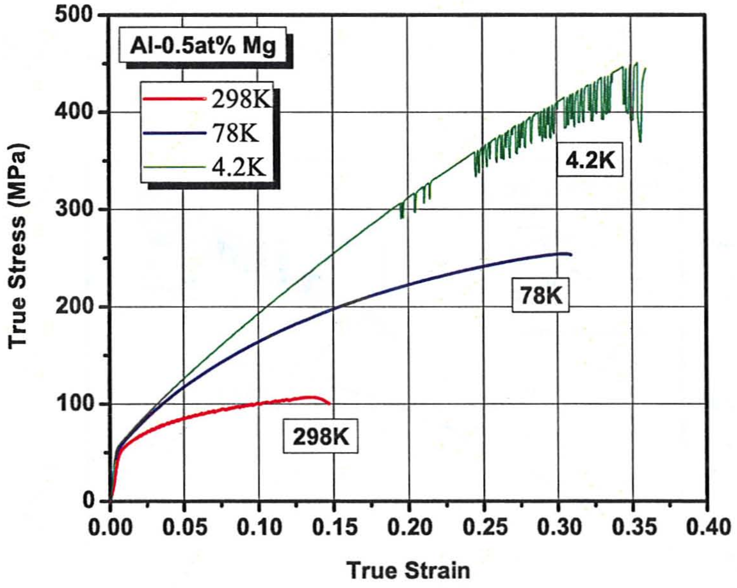

Figure 103: True Stress / True Strain behavior of Al-0.5at% Mg alloy

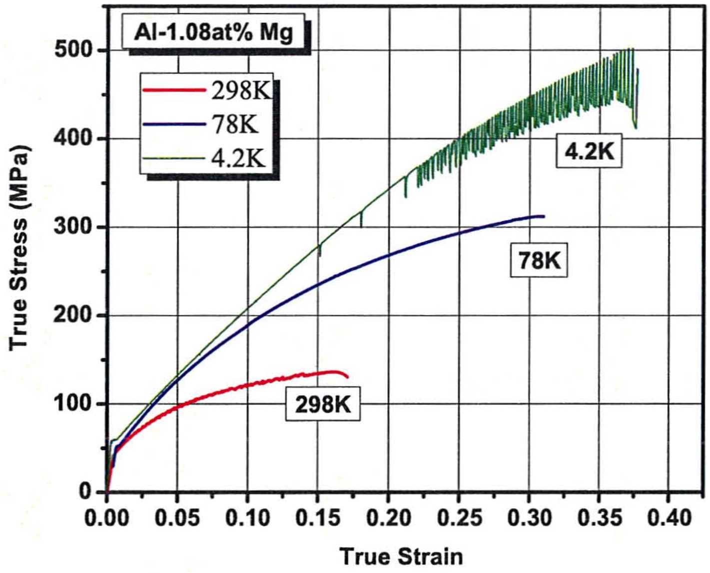

Figure 104: True Stress / True Strain behavior of Al-1.08at% Mg alloy

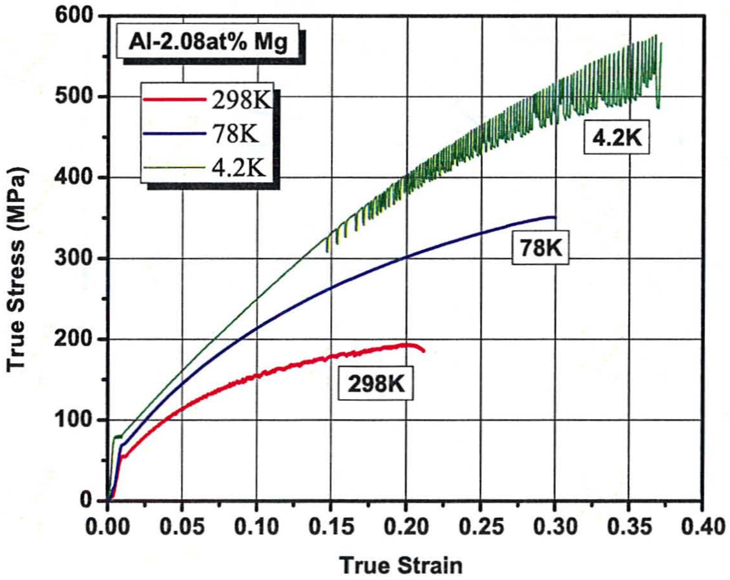

Figure 105: True Stress / True Strain behavior of Al-2.08at% Mg alloy

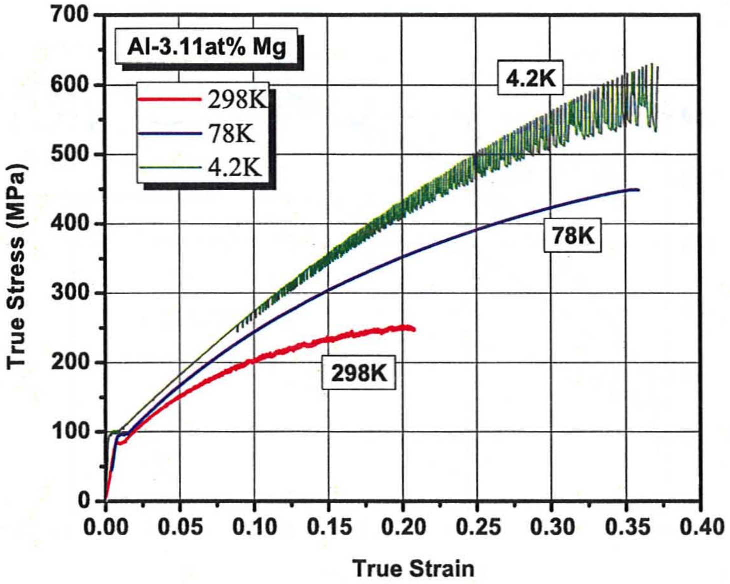

Figure 106: True Stress / True Strain behavior of Al-3.11at% Mg alloy

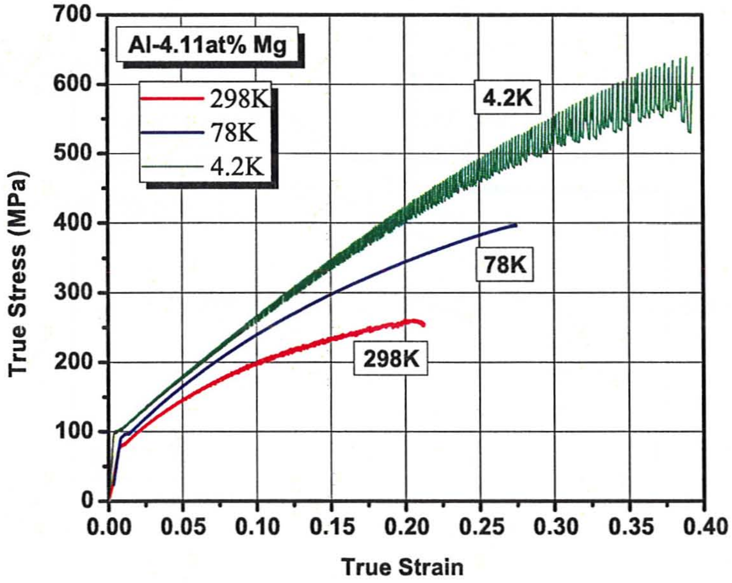

Figure 107: True Stress / True Strain behavior of Al-4.11at% Mg alloy

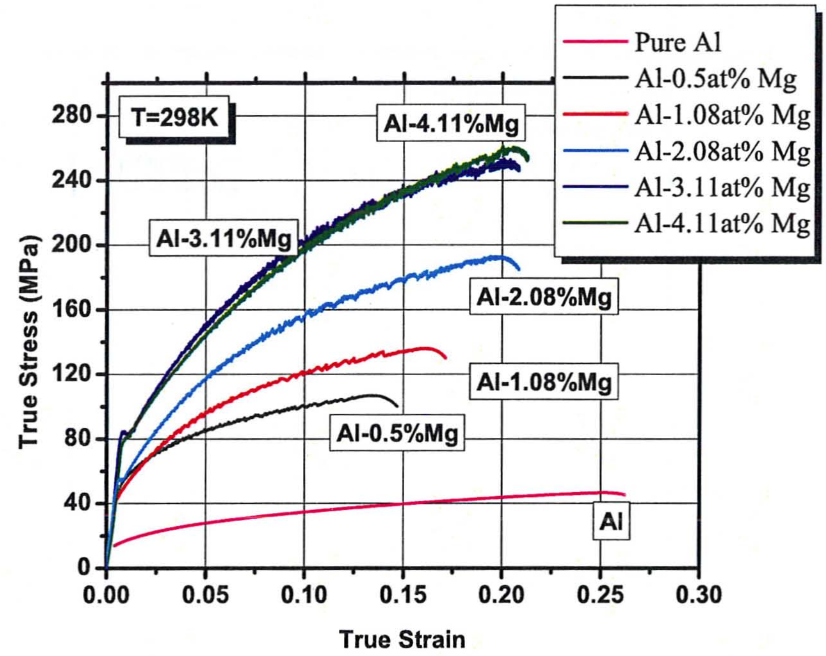

Figure 108: True Stress / True Strain behavior of Al-Mg alloys at 298K

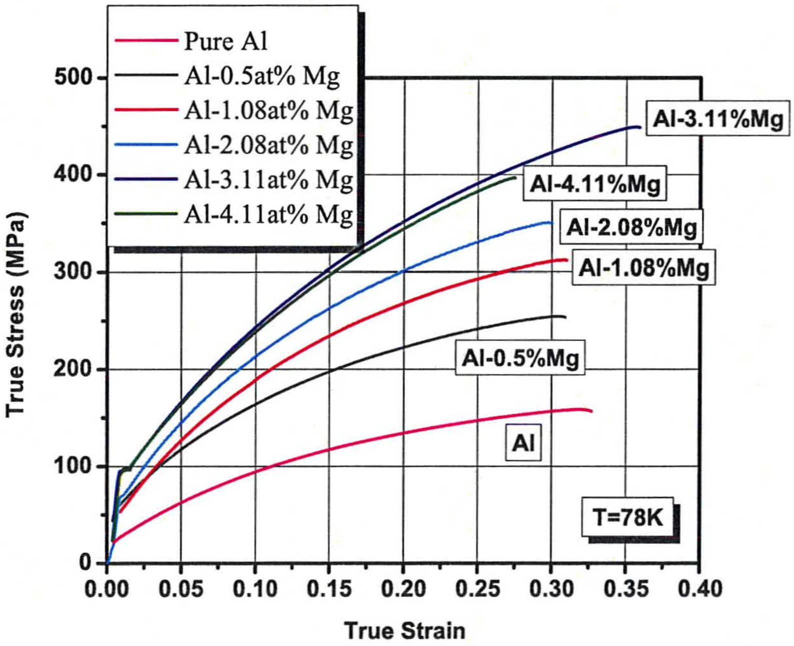

Figure 109: True Stress / True Strain behavior of Al-Mg alloys at 78K

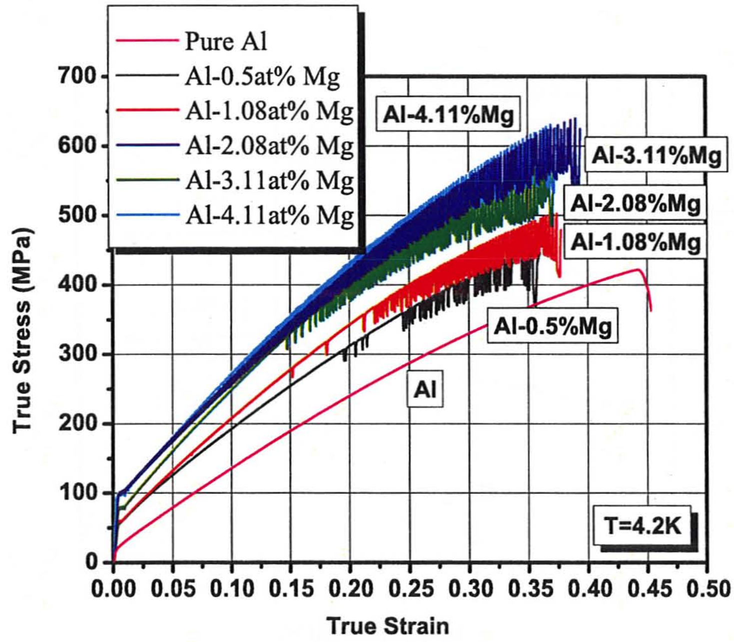

Figure 110: True Stress / True Strain behavior of Al-Mg alloys at 4.2K

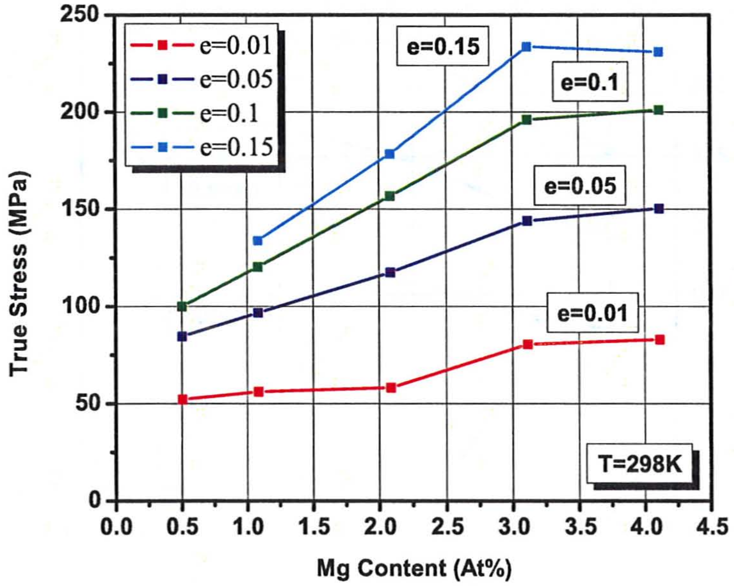

Figure 111: Stress Levels of Al-Mg Alloys vs. Mg Content by Strain Level at 298K

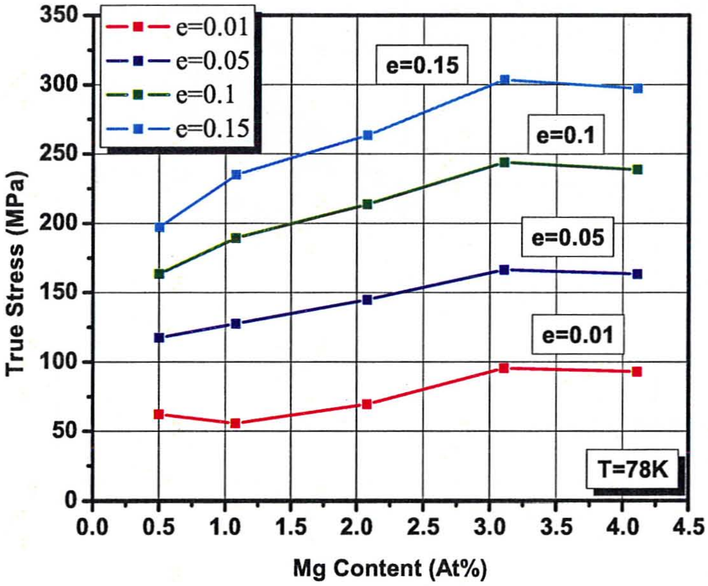

Figure 112: Stress Levels of Al-Mg Alloys vs. Mg Content by Strain Level at 78K

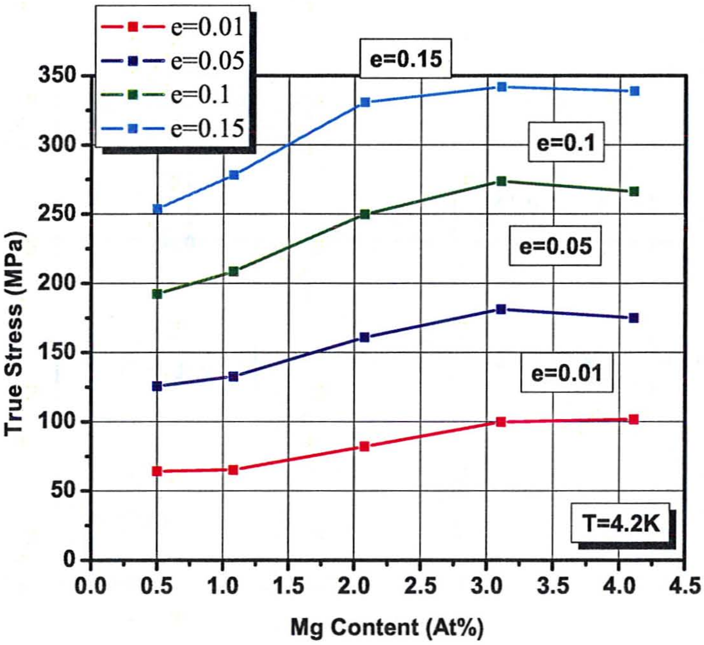

Figure 113: Stress Levels of Al-Mg Alloys vs. Mg Content by Strain Level at 4.2K

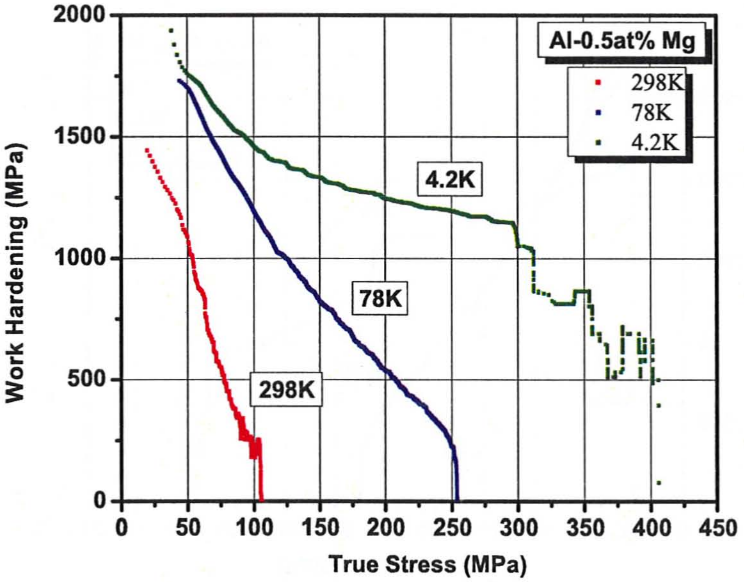

Figure 114: Work Hardening Rate vs. True Stress for Al-0.05at% Mg alloy

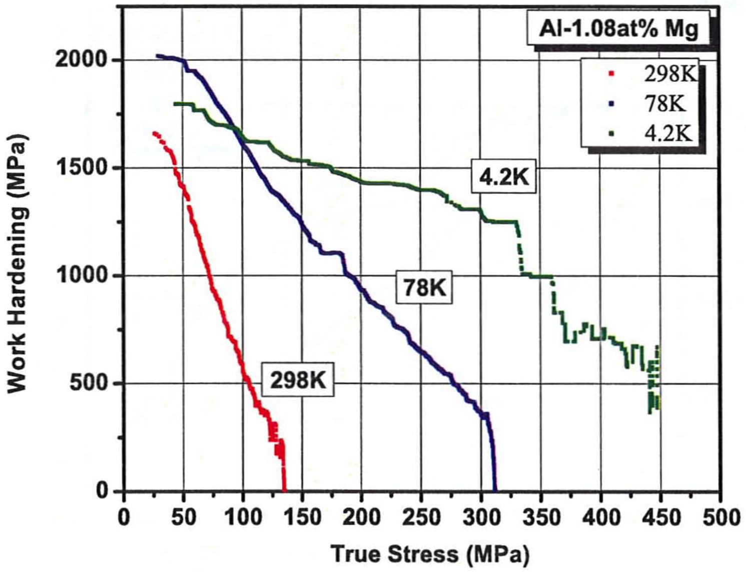

Figure 115: Work Hardening Rate vs. True Stress for Al-1.08at% Mg alloy

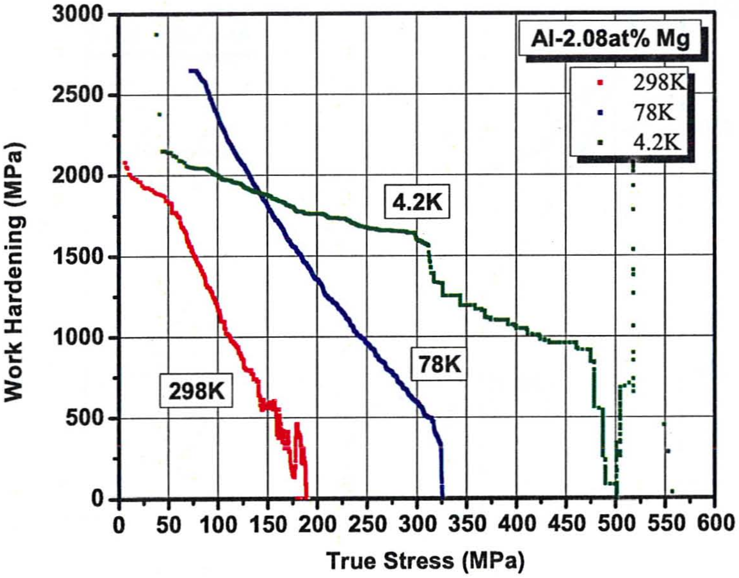

Figure 116: Work Hardening Rate vs. True Stress for Al-2.08at% Mg alloy

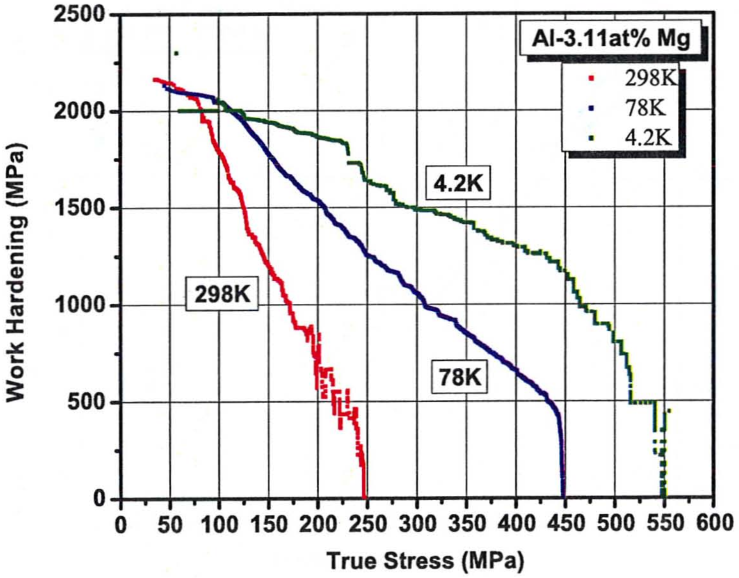

Figure 117: Work Hardening Rate vs. True Stress for Al-3.11at% Mg alloy

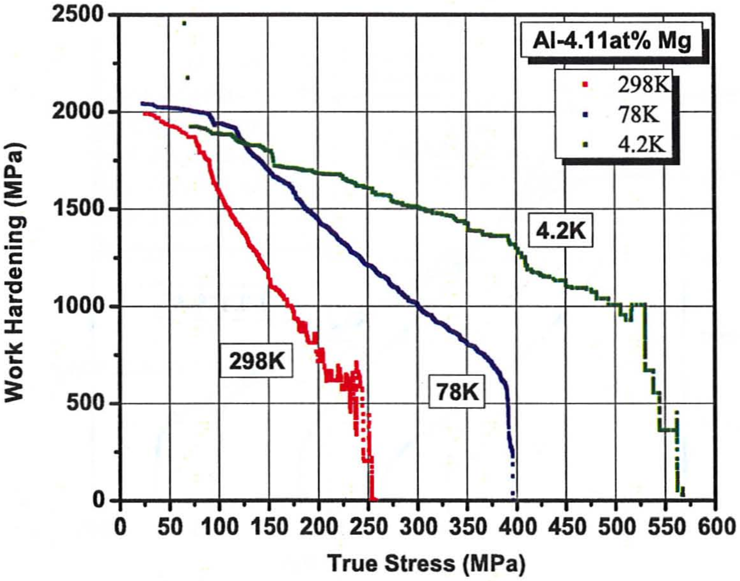

Figure 118: Work Hardening Rate vs. True Stress for Al-4.11at% Mg alloy

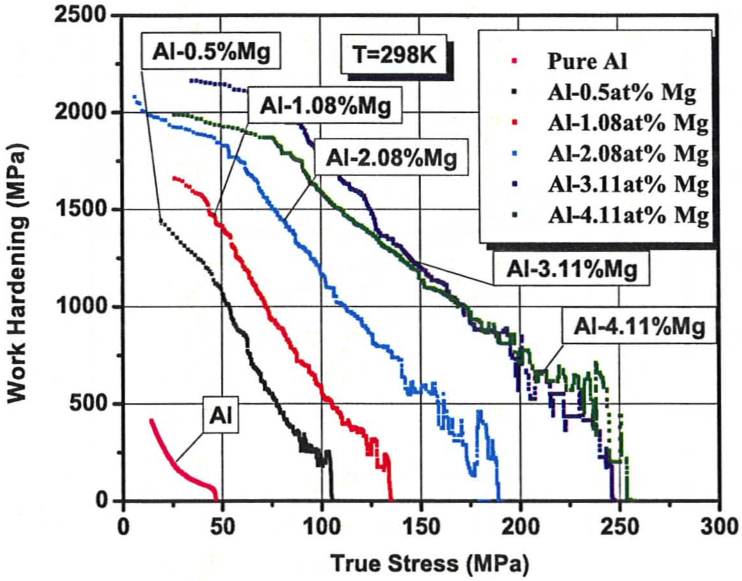

Figure 119: Work Hardening rate vs. True Stress for Al-Mg alloys at 298K

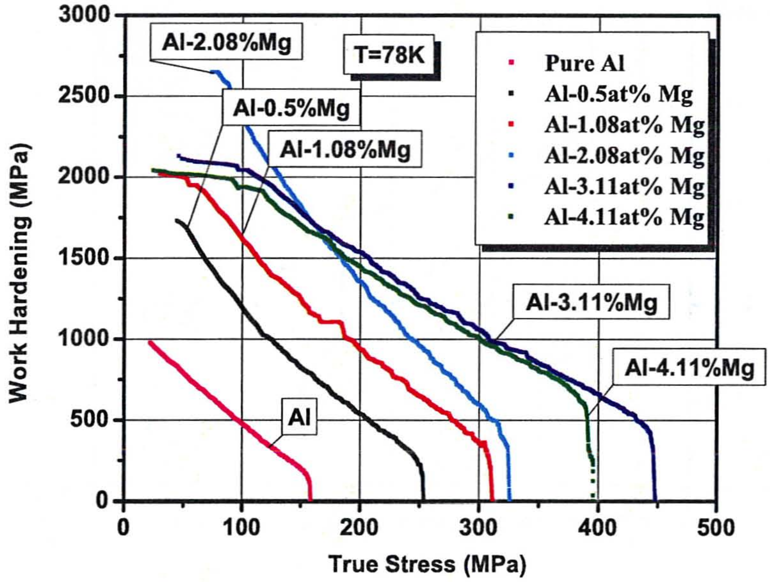

Figure 120: Work Hardening rate vs. True Stress for Al-Mg alloys at 78K

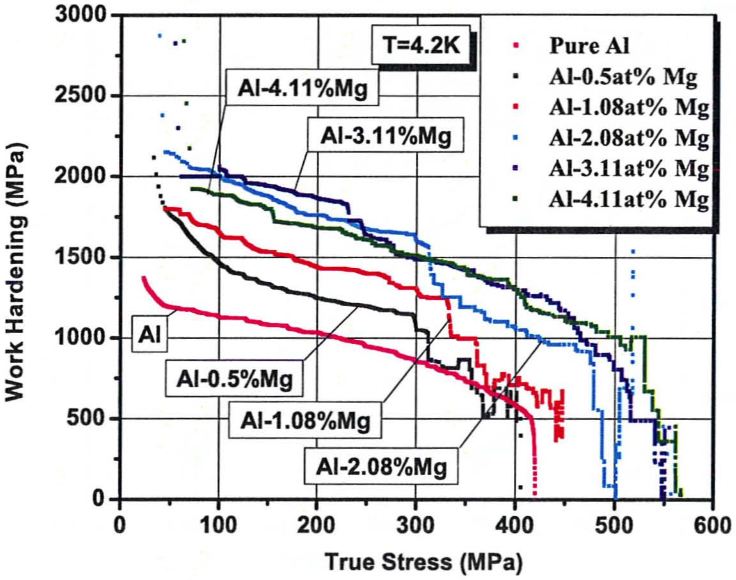

Figure 121: Work Hardening rate vs. True Stress for Al-Mg alloys at 4.2K

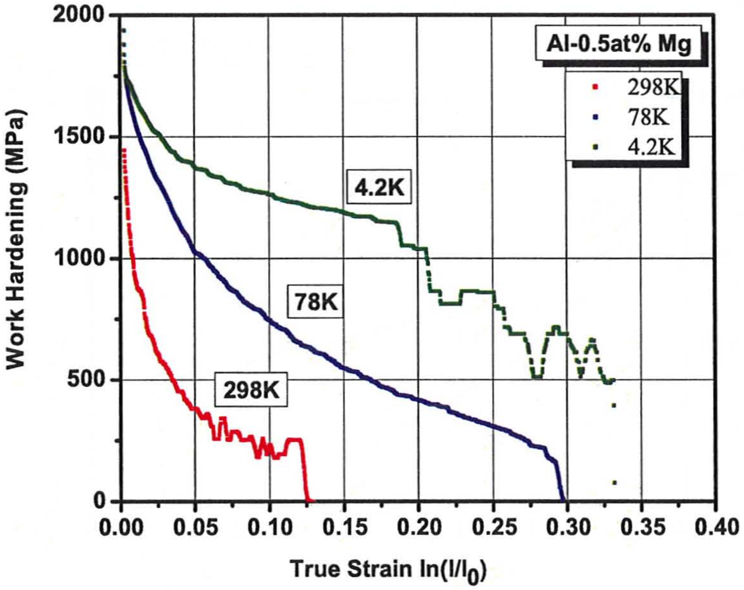

Figure 122: Work Hardening Rate vs. True Strain for Al-0.05at% Mg alloy

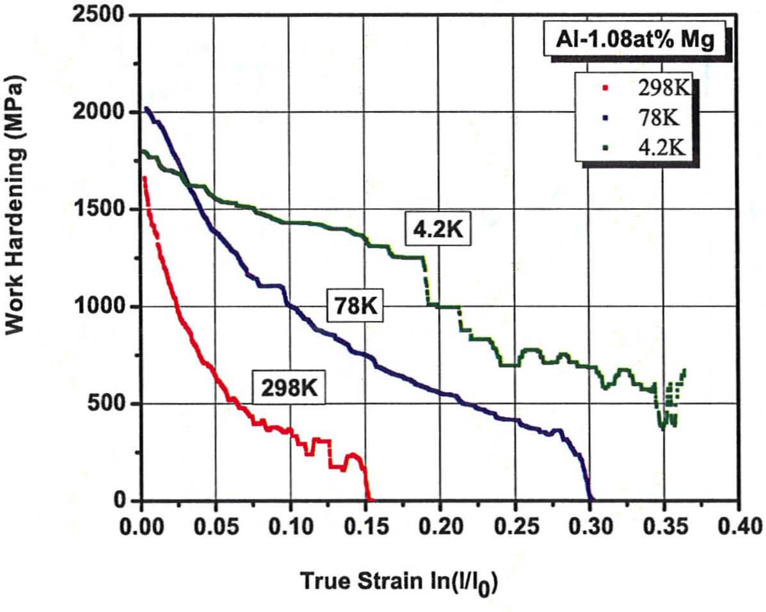

Figure 123: Work Hardening Rate vs. True Strain for Al-1.08at% Mg alloy

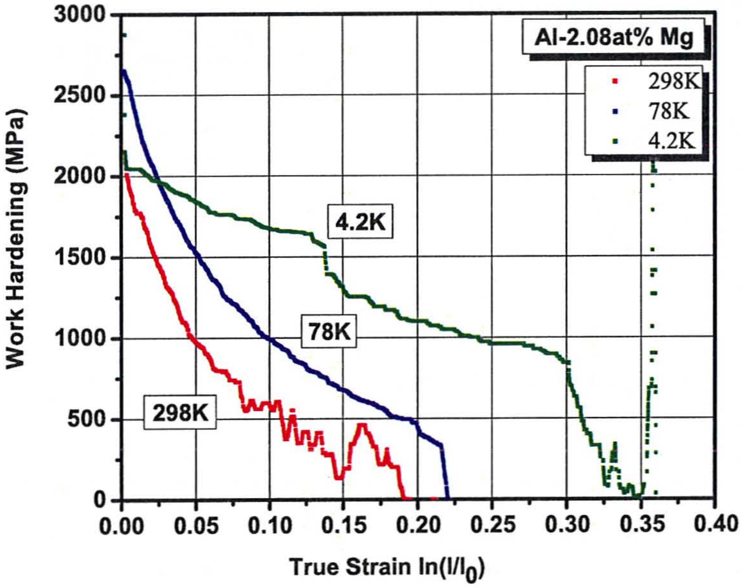

Figure 124: Work Hardening Rate vs. True Strain for Al-2.08at% Mg alloy

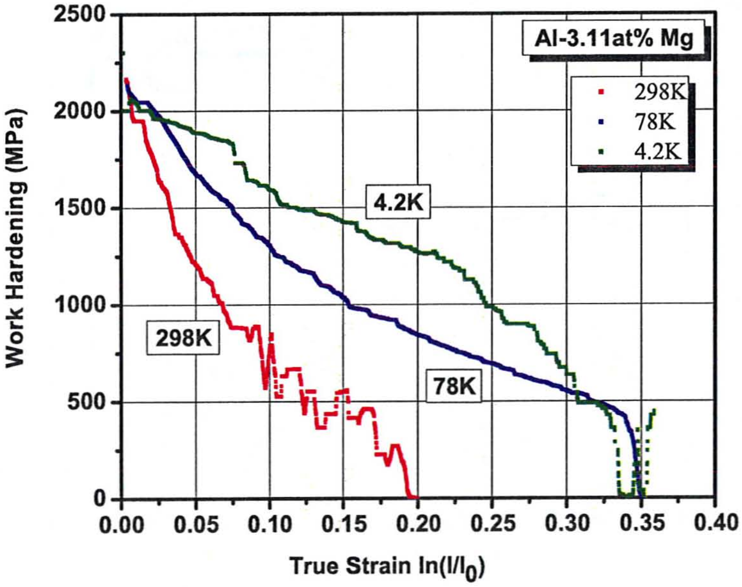

Figure 125: Work Hardening Rate vs. True Strain for Al-3.11at% Mg alloy

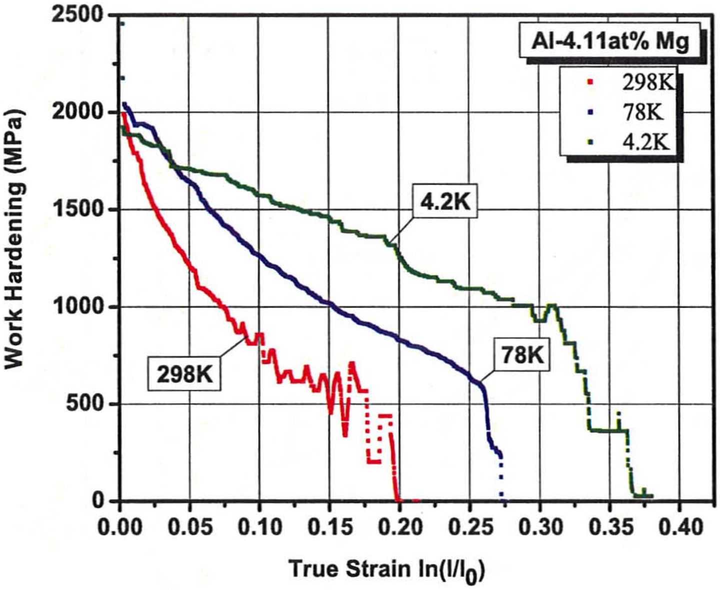

Figure 126: Work Hardening Rate vs. True Strain for Al-4.11at% Mg alloy

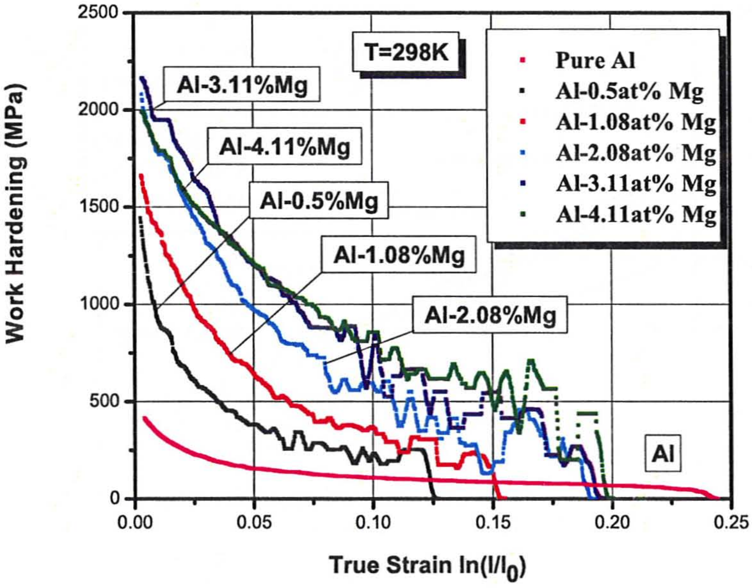

Figure 127: Work Hardening rate vs. True Strain for Al-Mg alloys at 298K

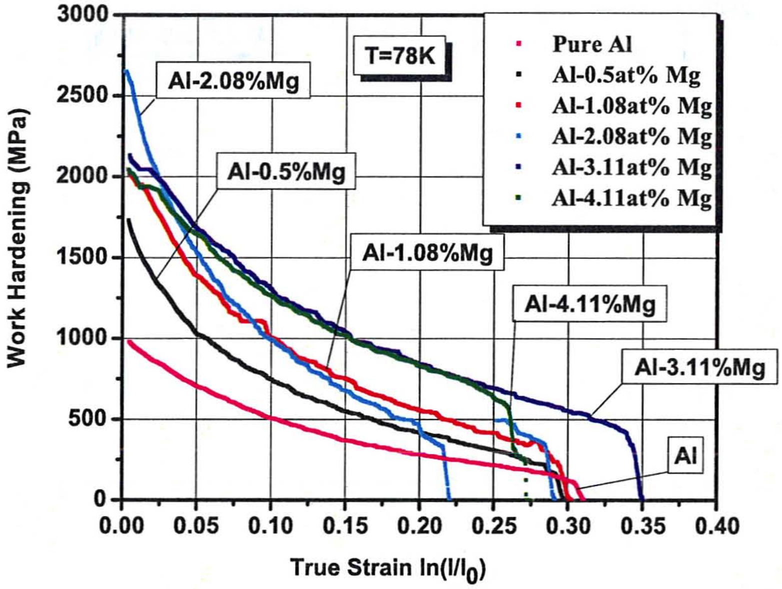

Figure 128: Work Hardening rate vs. True Strain for Al-Mg alloys at 78K

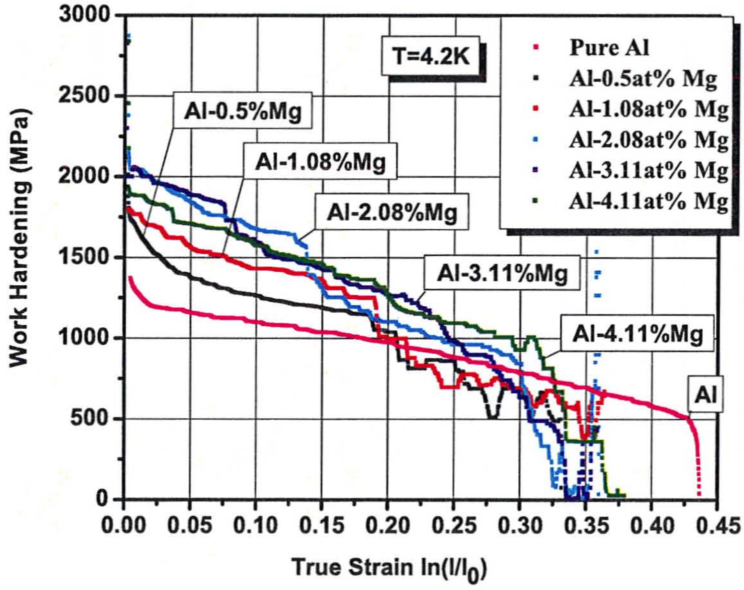

Figure 129: Work Hardening rate vs. True Strain for Al-Mg alloys at 4.2K

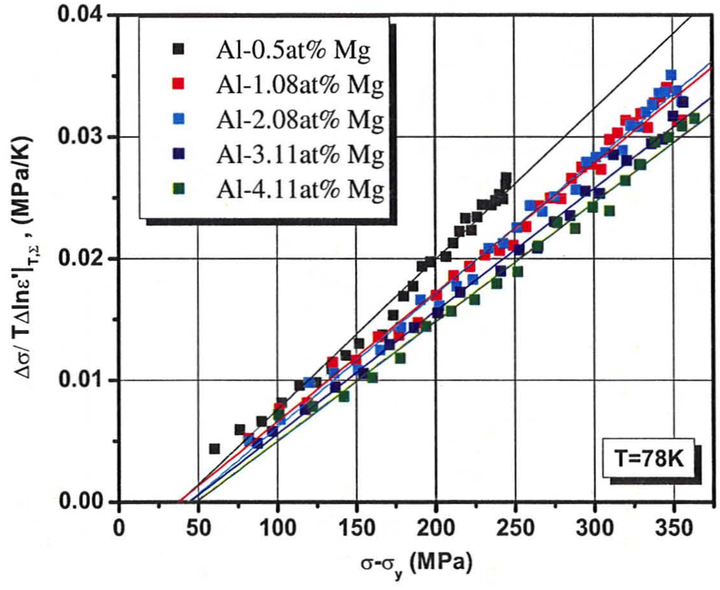

Figure 130: Haasen Plot for Al-Mg Alloys, 78K test

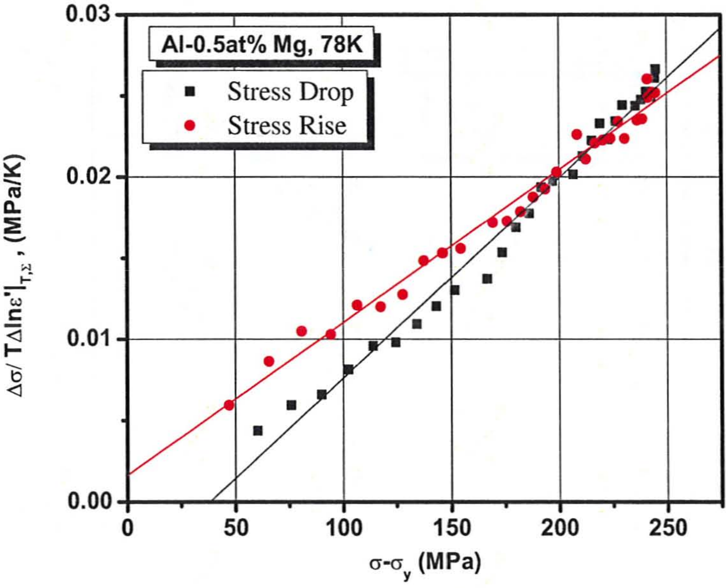

Figure 131: Haasen Plot for Al-0.5at% Mg alloy, 78K test

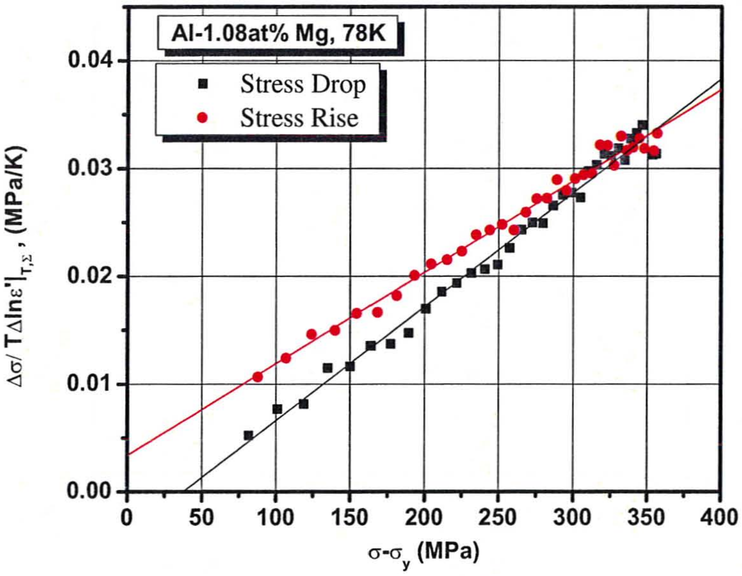

Figure 132: Haasen Plot for Al-1.08at% Mg alloy, 78K test

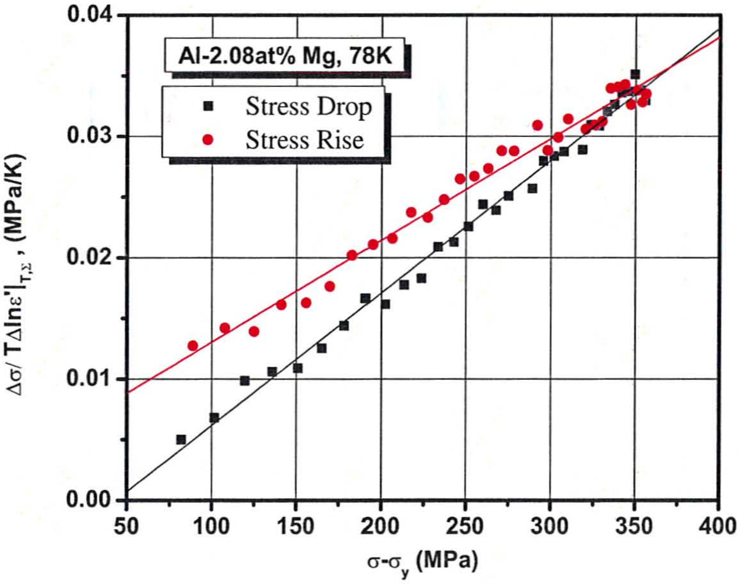

Figure 133: Haasen Plot for Al-2.08at% Mg alloy, 78K test

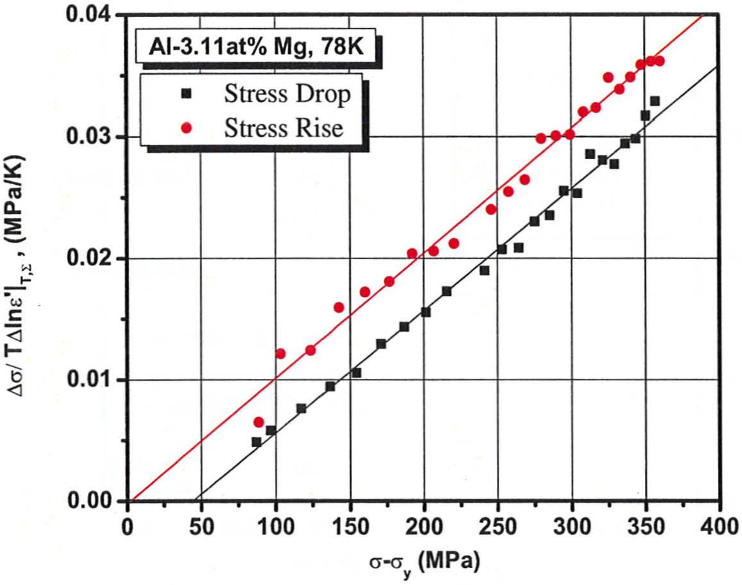

Figure 134: Haasen Plot for Al-3.11at% Mg alloy, 78K test

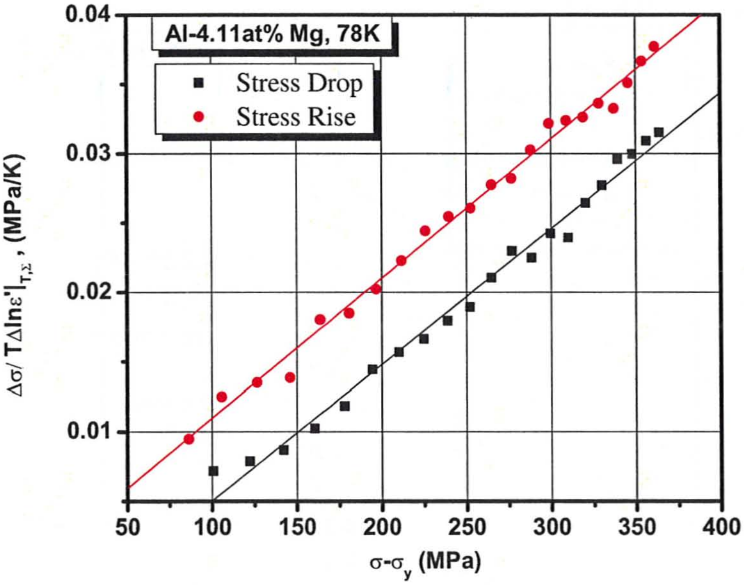

Figure 135: Haasen Plot for Al-4.11at% Mg alloy, 78K test

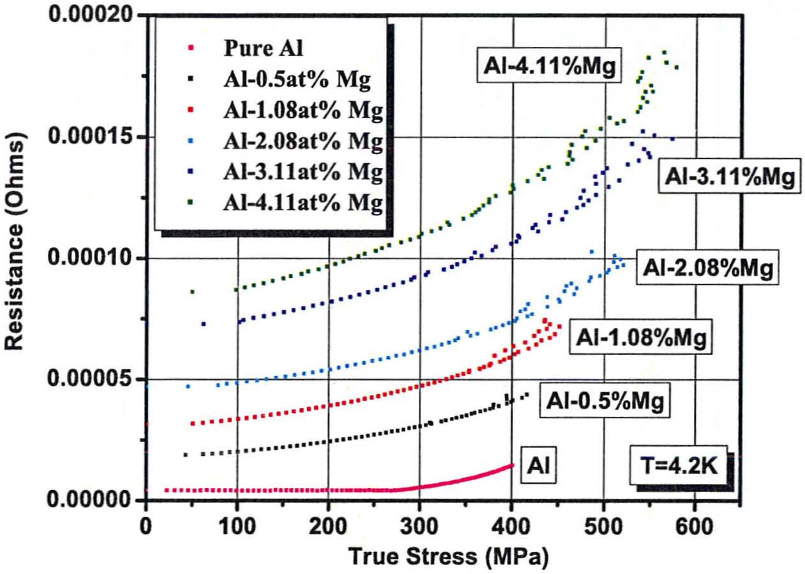

Figure 136: Resistance vs. Stress Data for Al-Mg Alloys

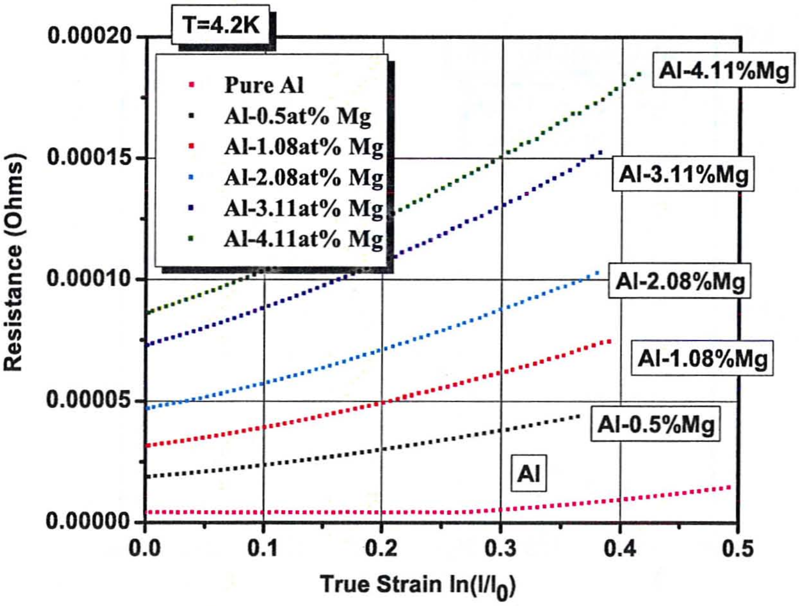

Figure 137: Resistance vs. Strain Data for Al-Mg Alloys

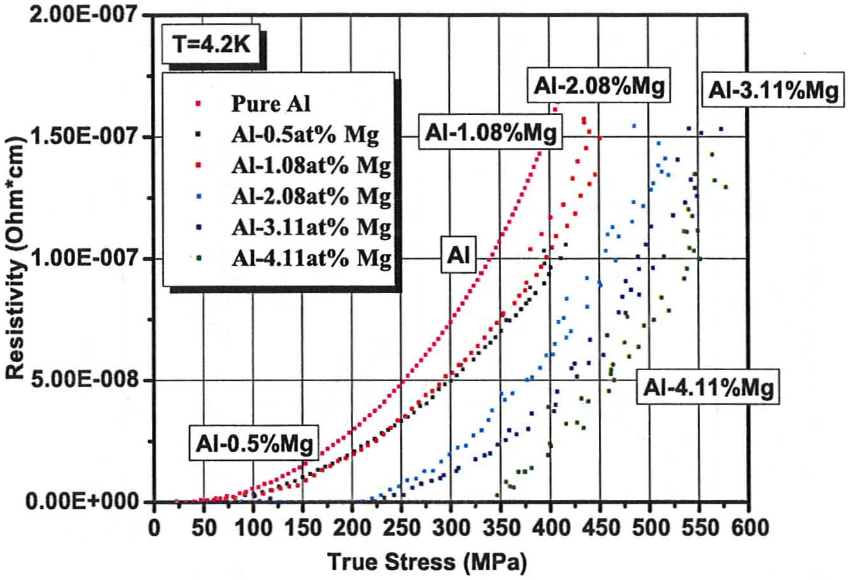

Figure 138: Resistivity vs. Stress Data for Al-Mg Alloys

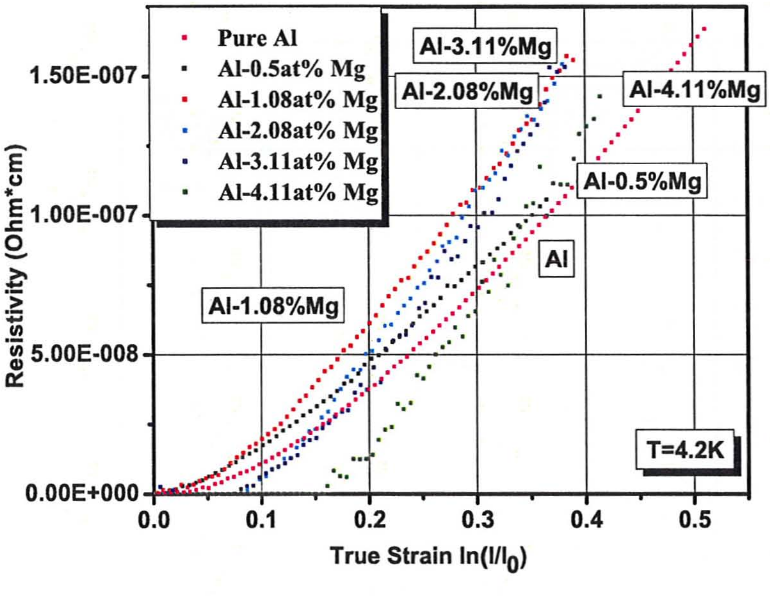

Figure 139: Resistivity vs. Strain Data for Al-Mg Alloys

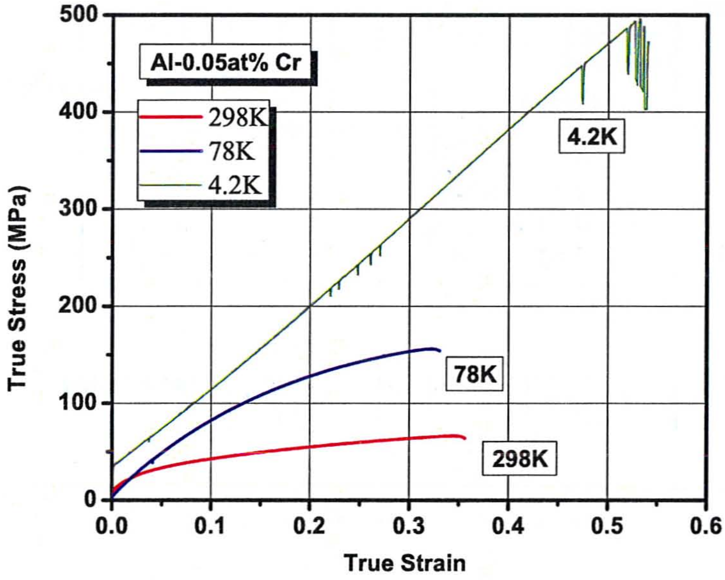

Figure 140: True Stress / True Strain Behavior for Recrystallized Al-0.05at% Cr Alloy

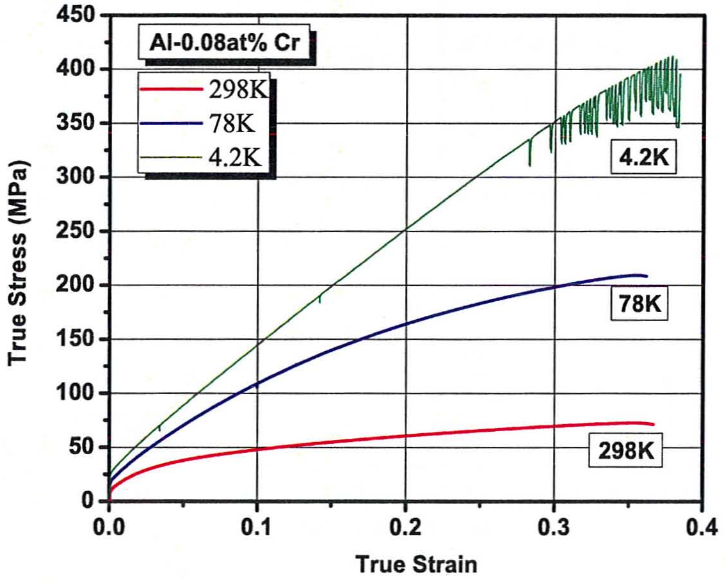

Figure 141: True Stress / True Strain Behavior for Recrystallized Al-0.08at% Cr Alloy

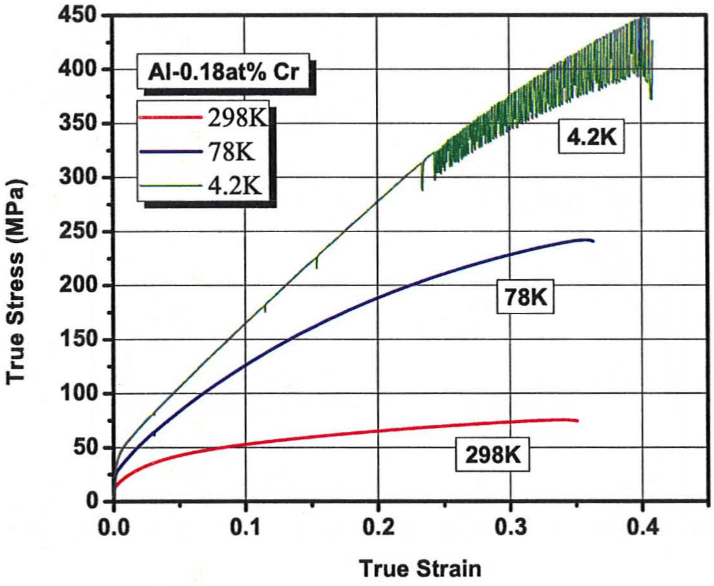

Figure 142: True Stress / True Strain Behavior for Recrystallized Al-0.18at% Cr Alloy

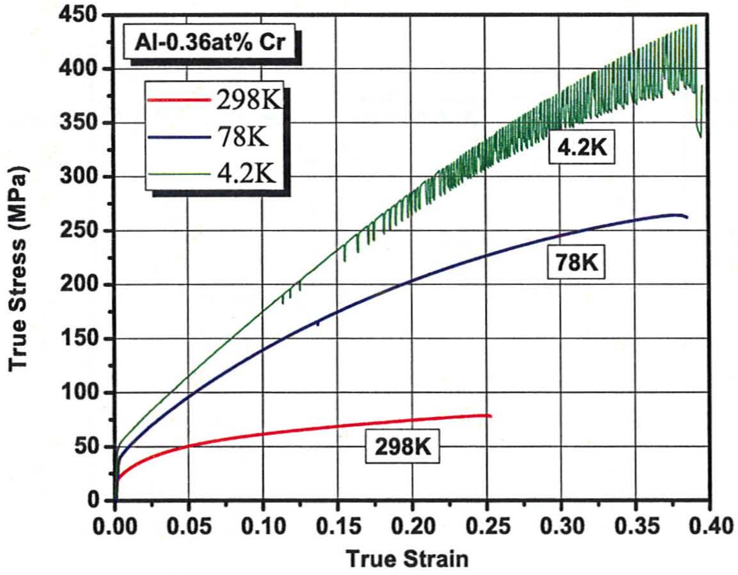

Figure 143: True Stress / True Strain Behavior for Recrystallized Al-0.36at% Cr Alloy

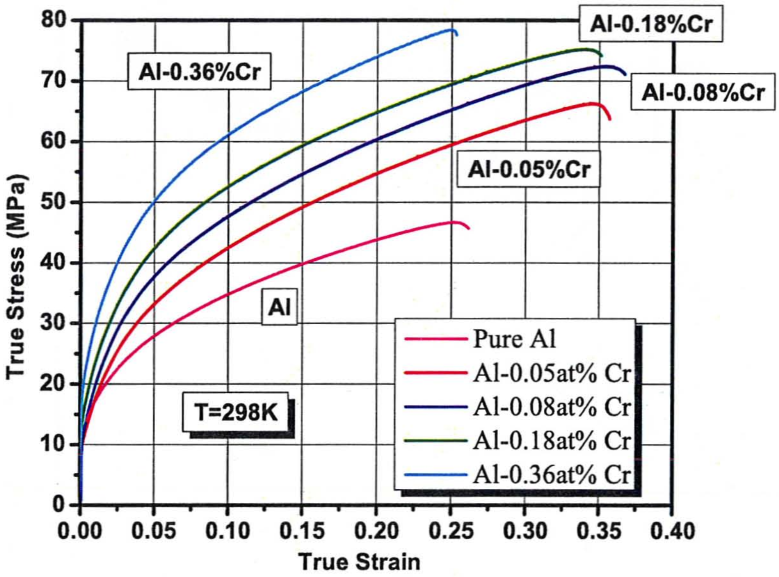

Figure 144: True Stress / True Strain behavior for Recrystallized Al-Cr alloys at 298K

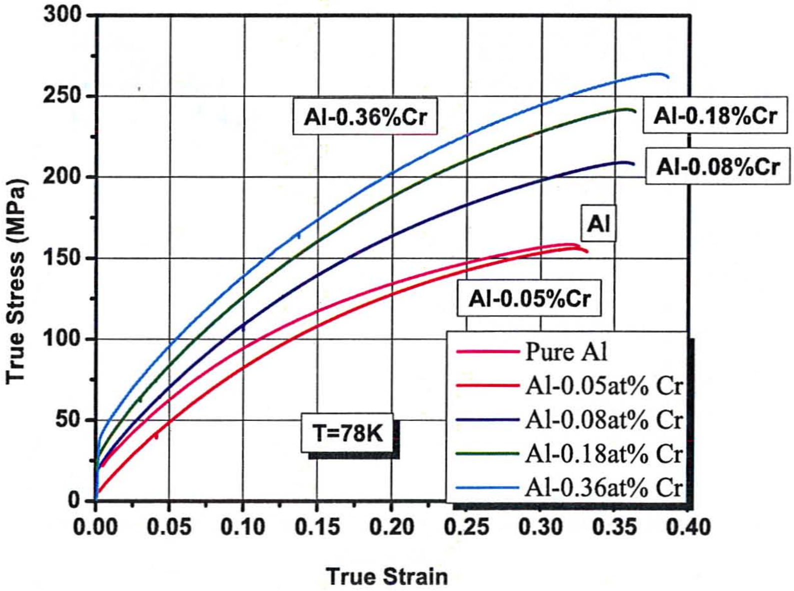

Figure 145: True Stress / True Strain behavior for Recrystallized Al-Cr alloys at 78K

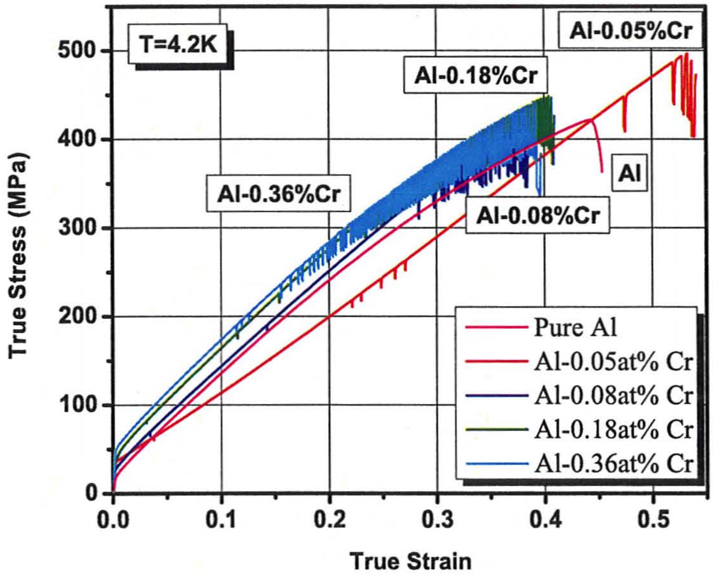

Figure 146: True Stress / True Strain behavior for Recrystallized Al-Cr alloys at 4.2K

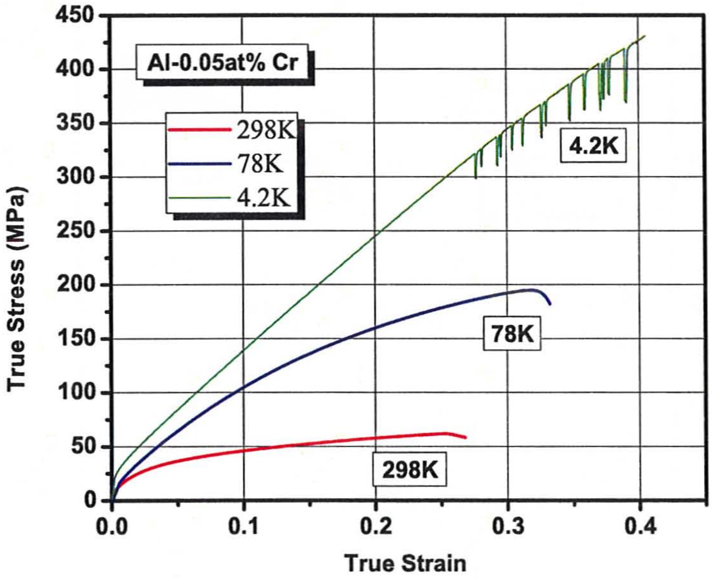

Figure 147: True Stress / True Strain Behavior for Non-Recrystallized Al-0.05at% Cr Alloy

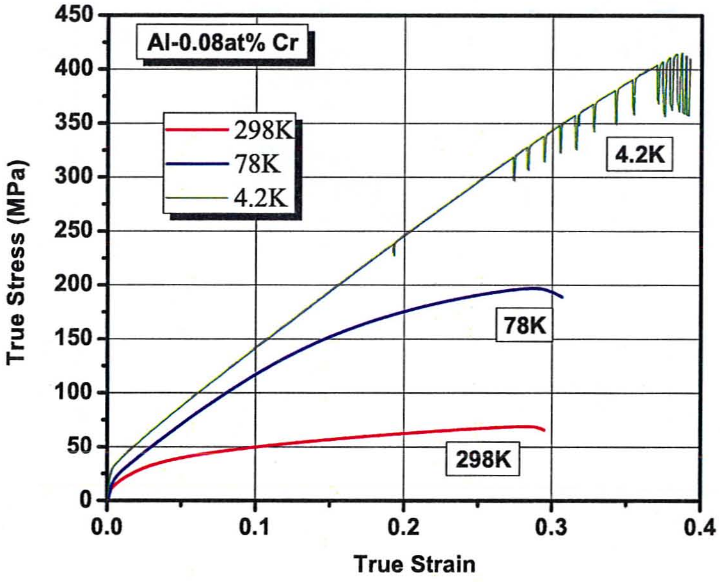

Figure 148: True Stress / True Strain Behavior for Non-Recrystallized Al-0.08at% Cr Alloy

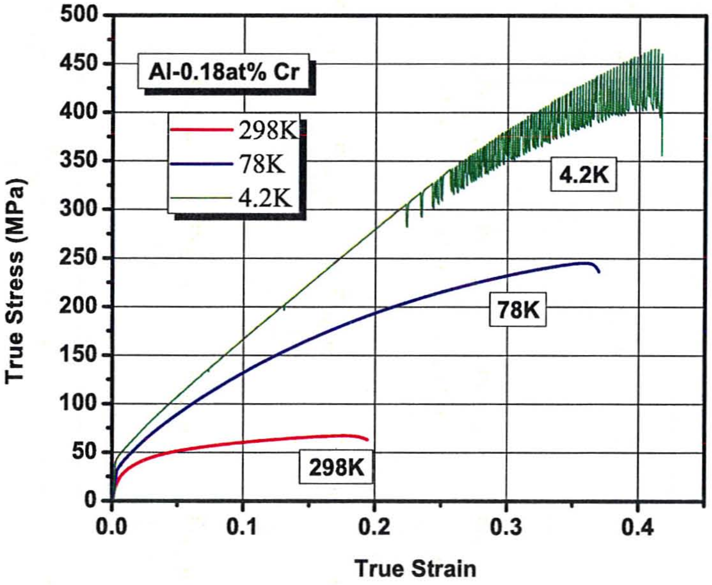

Figure 149: True Stress / True Strain Behavior for Non-Recrystallized Al-0.18at% Cr Alloy

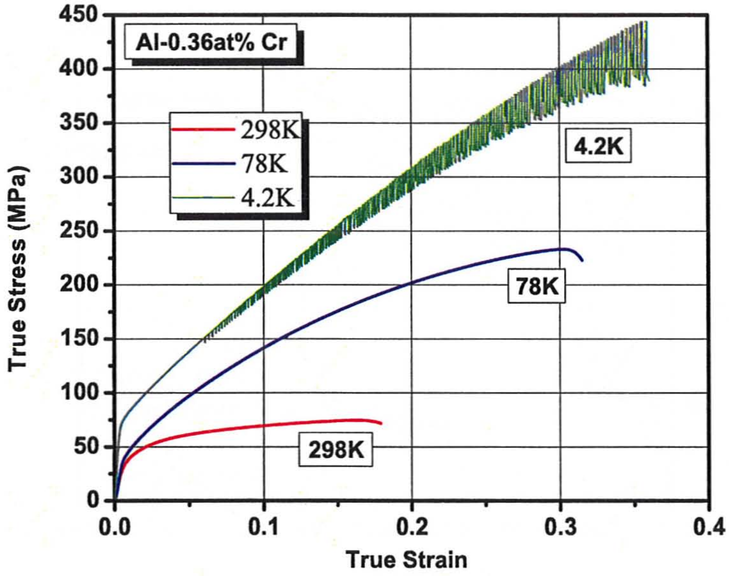

Figure 150: True Stress / True Strain Behavior for Non-Recrystallized Al-0.36at% Cr Alloy

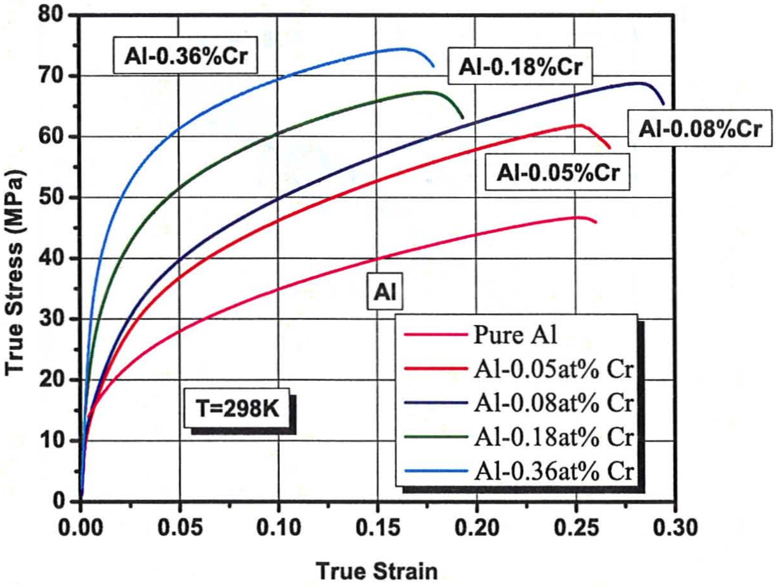

Figure 151: True Stress / True Strain behavior for Non-Recrystallized Al-Cr alloys at 298K

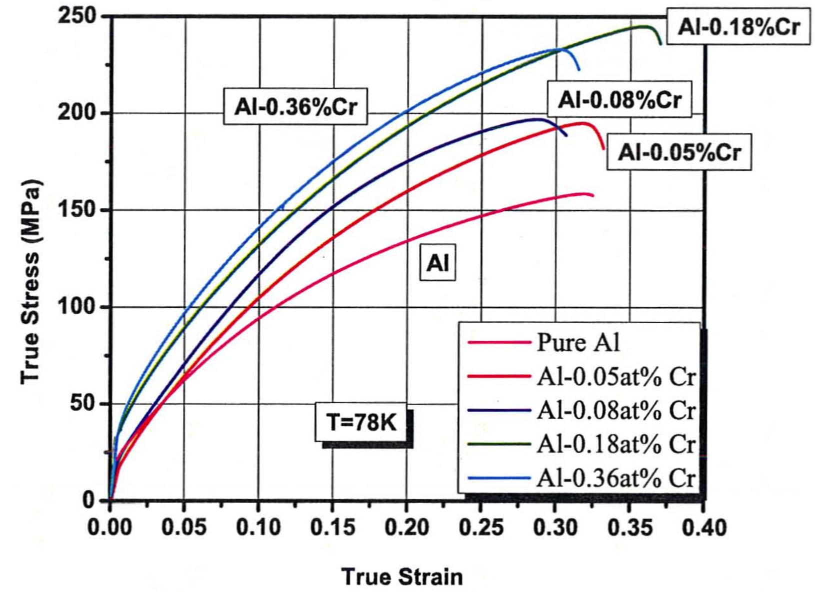

Figure 152: True Stress / True Strain behavior for Non-Recrystallized Al-Cr alloys at 78K

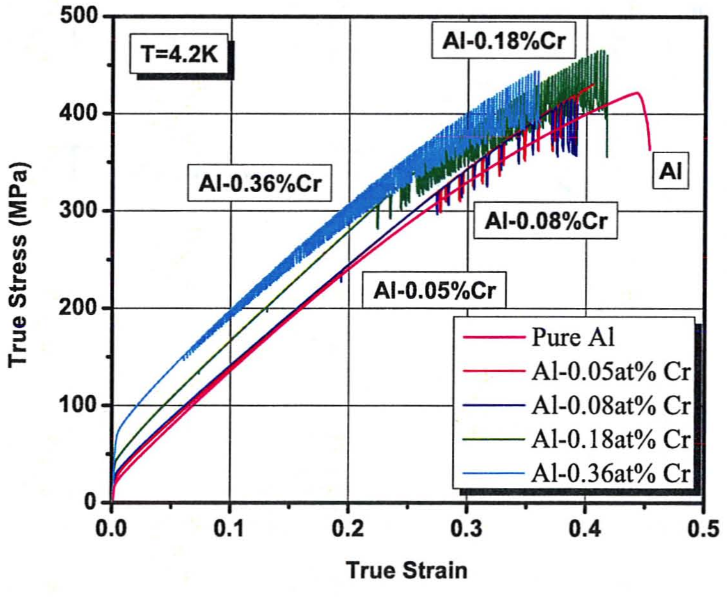

Figure 153: True Stress / True Strain behavior for Recrystallized Al-Cr alloys at 4.2K

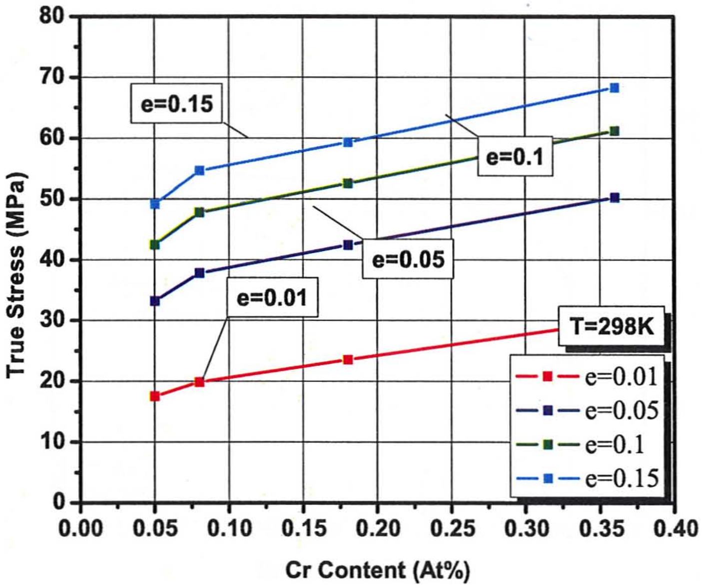

Figure 154: Stress Levels of Recrystallized Al-Cr Alloys vs. Mg Content by Strain Level at 298K

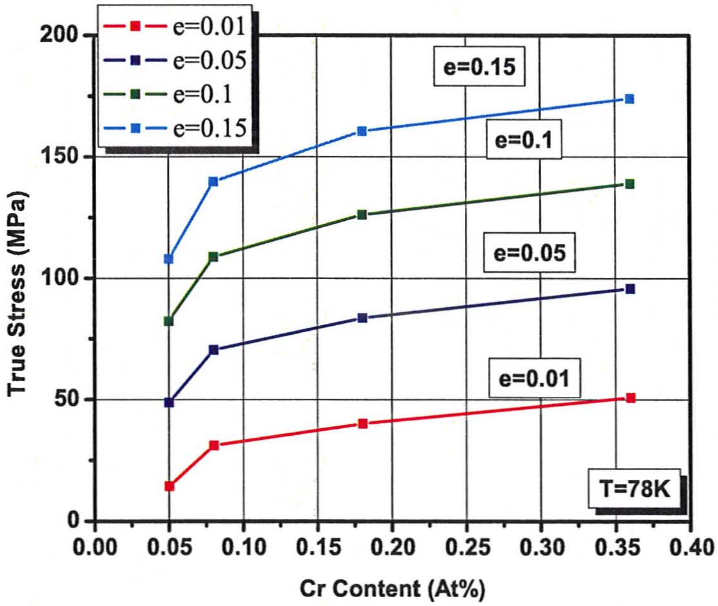

Figure 155: Stress Levels of Recrystallized Al-Cr Alloys vs. Mg Content by Strain Level at 78K

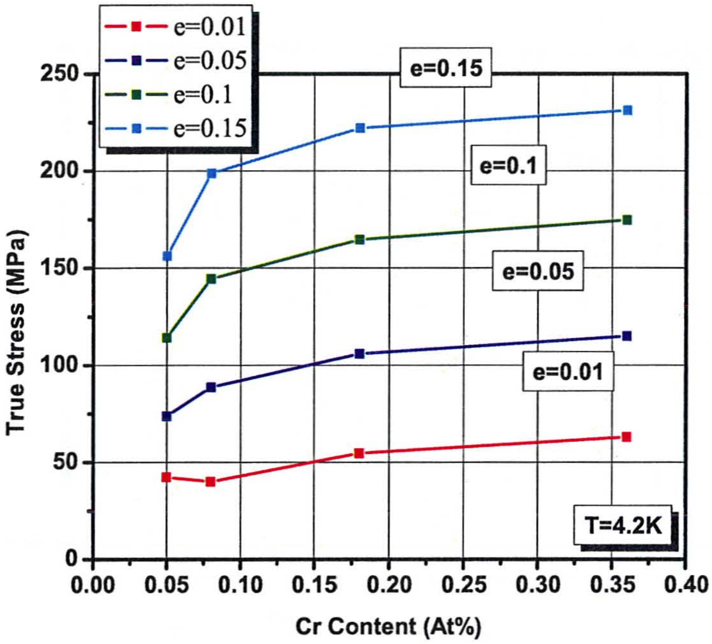

Figure 156: Stress Levels of Recrystallized Al-Cr Alloys vs. Mg Content by Strain Level at 4.2K

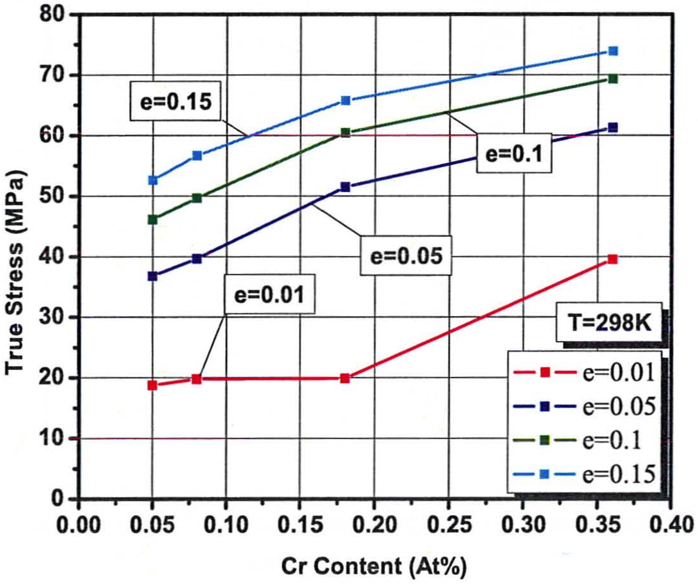

Figure 157: Stress Levels of Non-Recrystallized Al-Cr Alloys vs. Mg Content by Strain Level at 298K

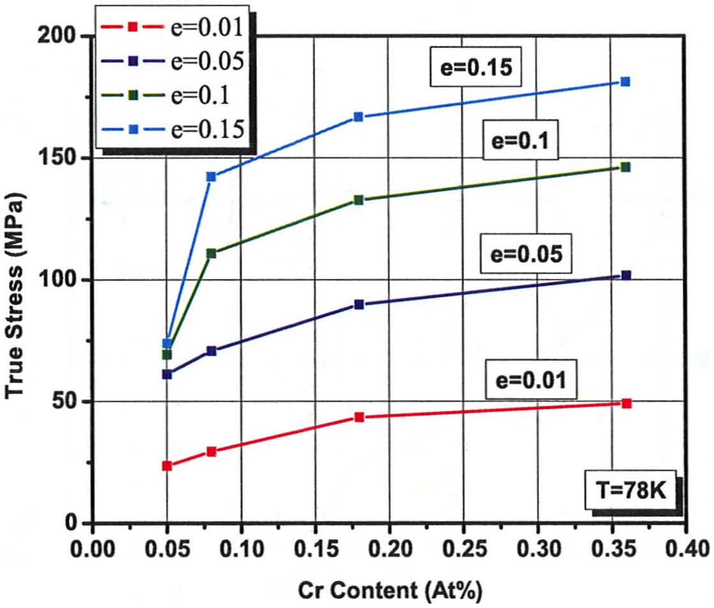

Figure 158: Stress Levels of Non-Recrystallized Al-Cr Alloys vs. Mg Content by Strain Level at 78K

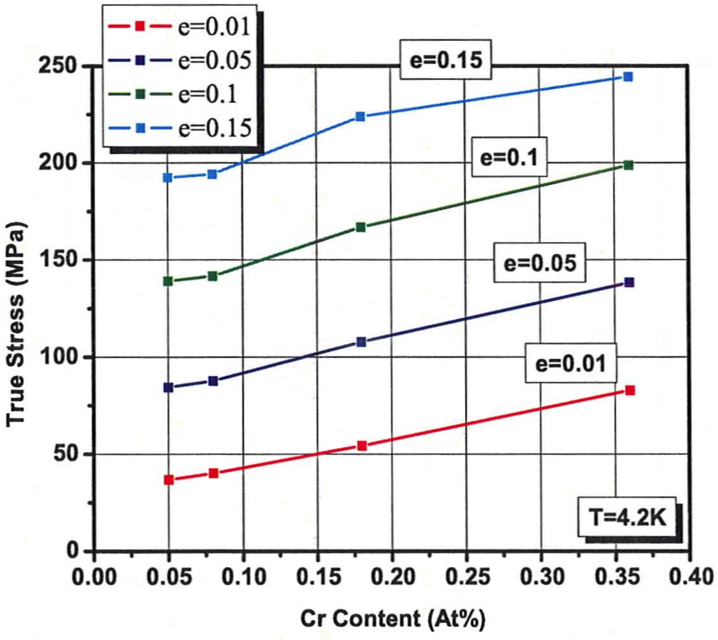

Figure 159: Stress Levels of Non-Recrystallized Al-Cr Alloys vs. Mg Content by Strain Level at 4.2K

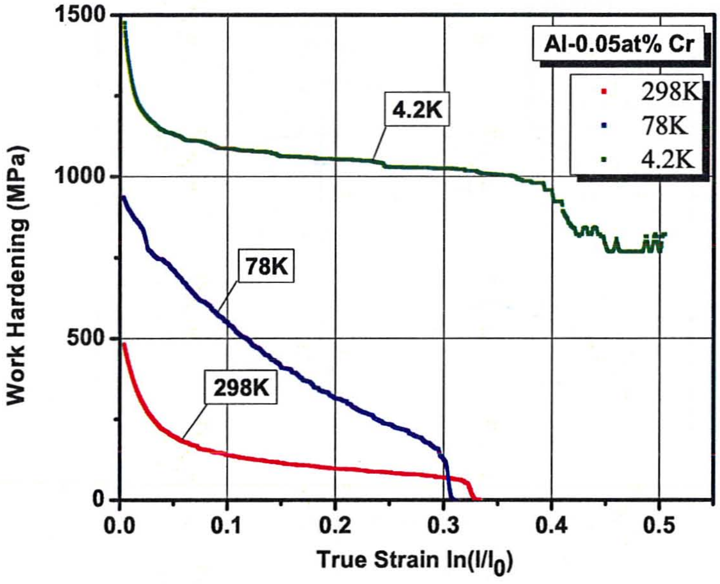

Figure 160: Work Hardening Rate vs. True Stress for Recrystallized Al-0.05at% Cr alloy

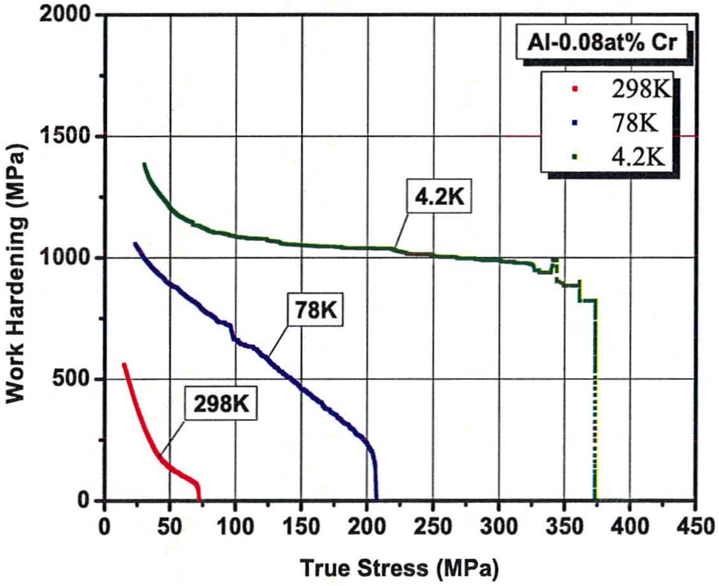

Figure 161: Work Hardening Rate vs. True Stress for Recrystallized Al-0.08at% Cr alloy

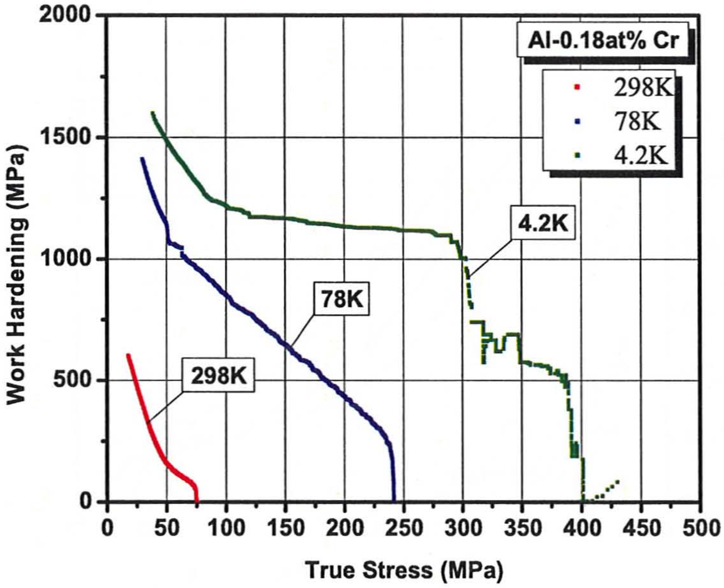

Figure 162: Work Hardening Rate vs. True Stress for Recrystallized Al-0.18at% Cr alloy

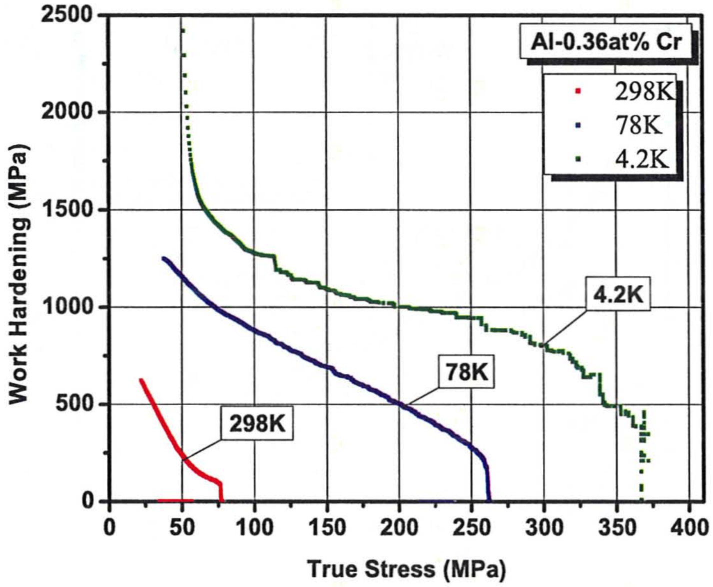

Figure 163: Work Hardening Rate vs. True Stress for Recrystallized Al-0.36at% Cr alloy

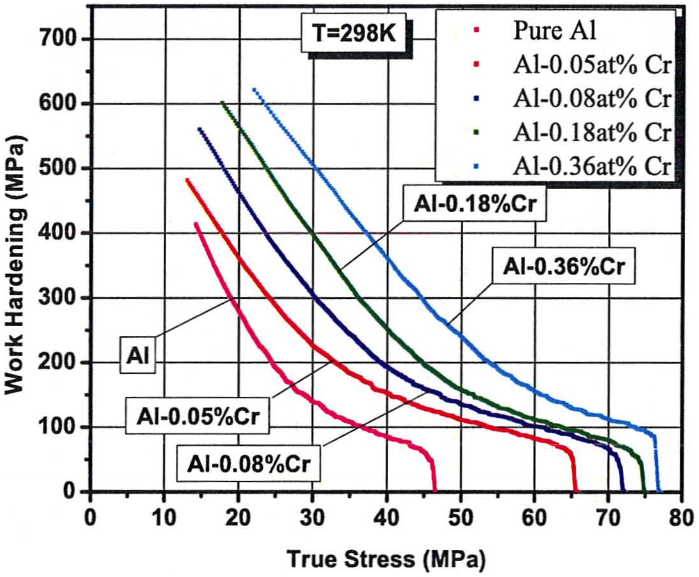

Figure 164: Work Hardening rate vs. True Stress for Recrystallized Al-Cr alloys at 298K

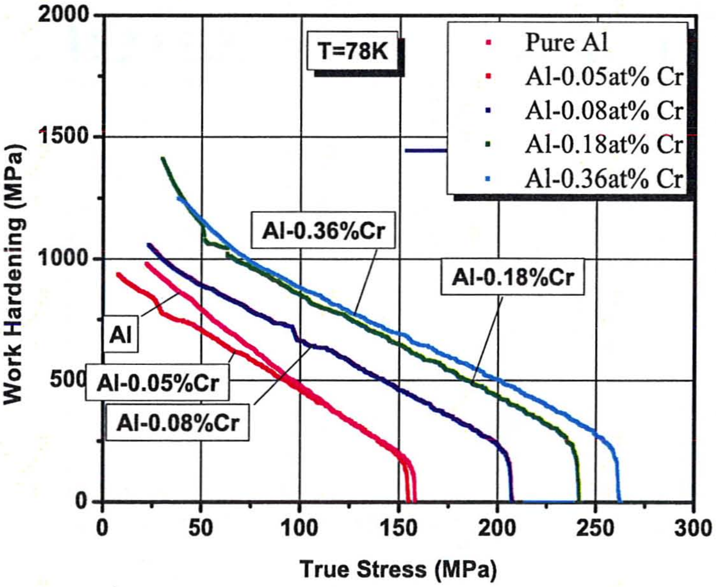

Figure 165: Work Hardening rate vs. True Stress for Recrystallized Al-Cr alloys at 78K

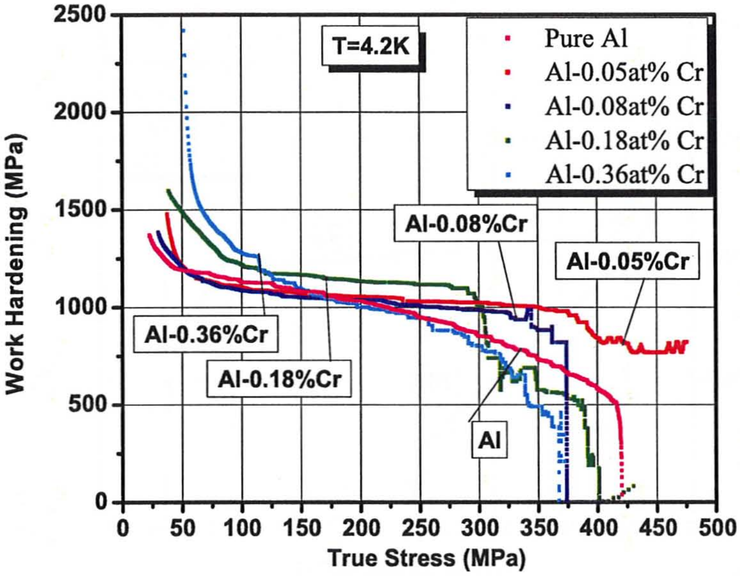

Figure 166: Work Hardening rate vs. True Stress for Recrystallized Al-Cr alloys at 4.2K

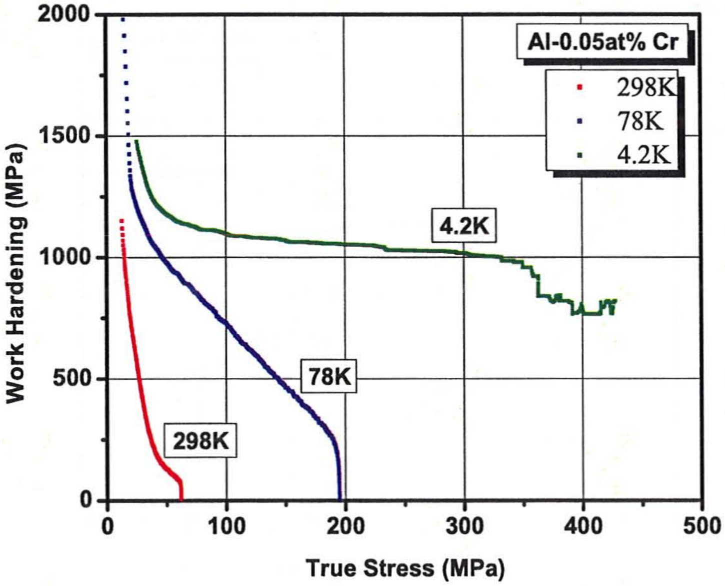

Figure 167: Work Hardening Rate vs. True Stress for Non-Recrystallized Al-0.05at% Cr alloy

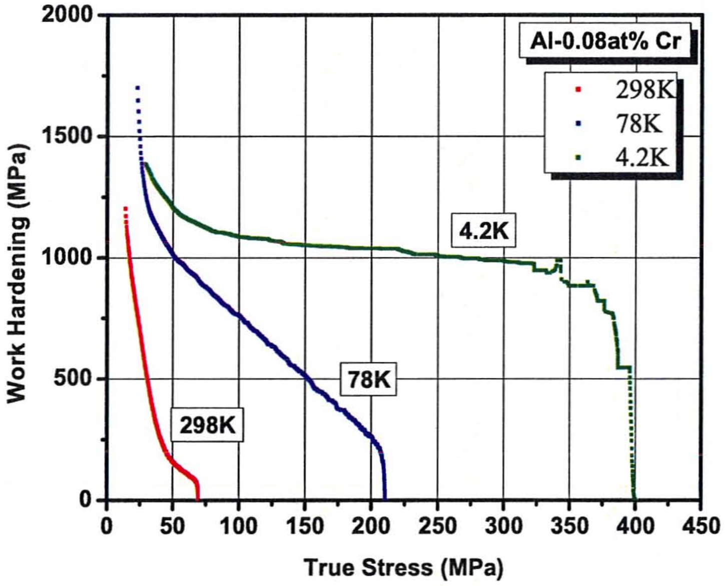

Figure 168: Work Hardening Rate vs. True Stress for Non-Recrystallized Al-0.08at% Cr alloy

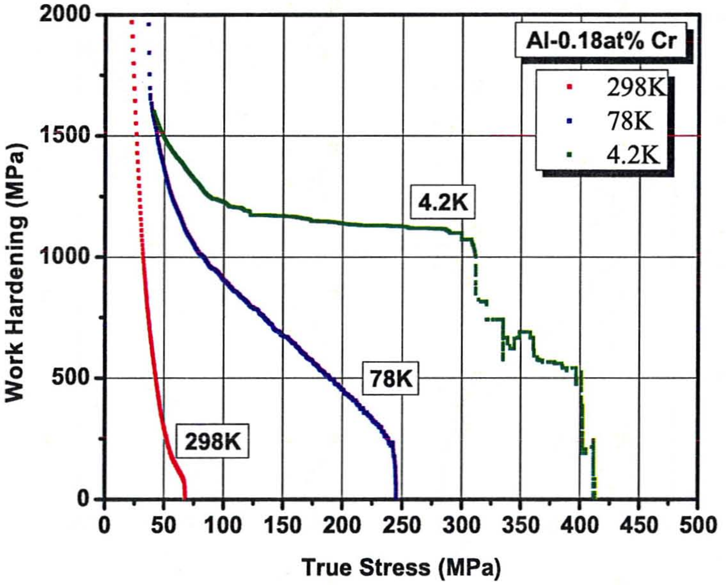

Figure 169: Work Hardening Rate vs. True Stress for Non-Recrystallized Al-0.16at% Cr alloy

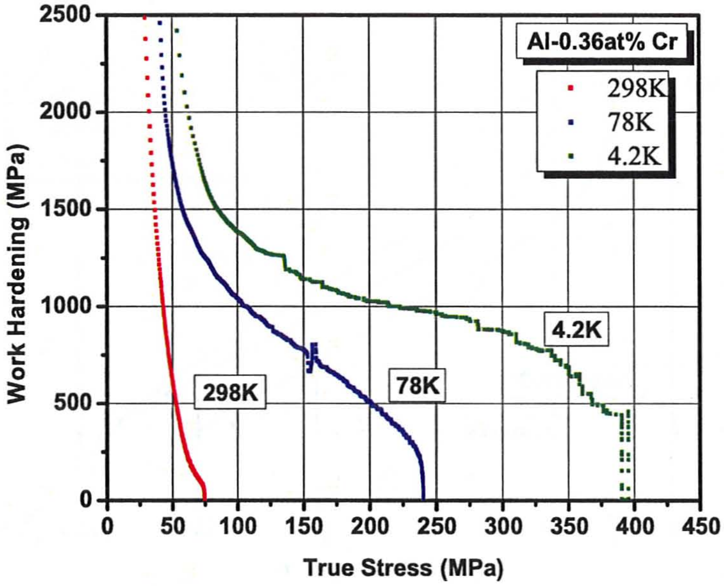

Figure 170: Work Hardening Rate vs. True Stress for Non-Recrystallized Al-0.36at% Cr alloy

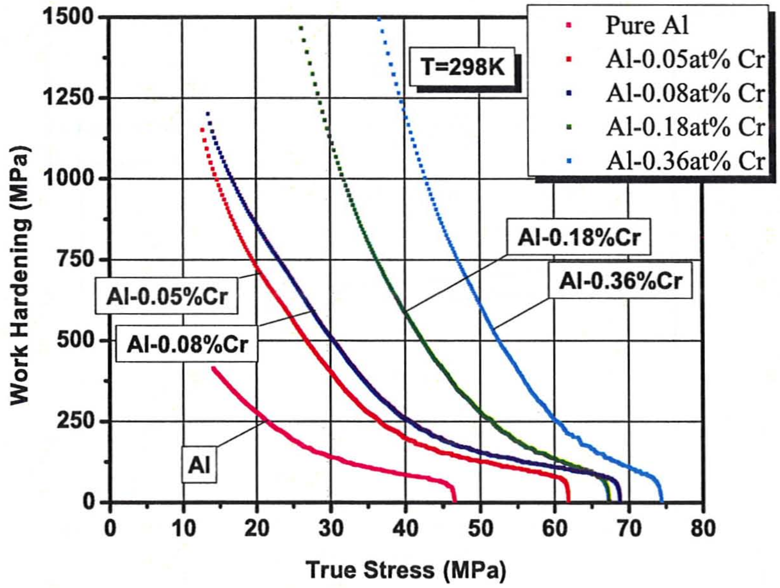

Figure 171: Work Hardening rate vs. True Stress for Non-Recrystallized Al-Cr alloys at 298K

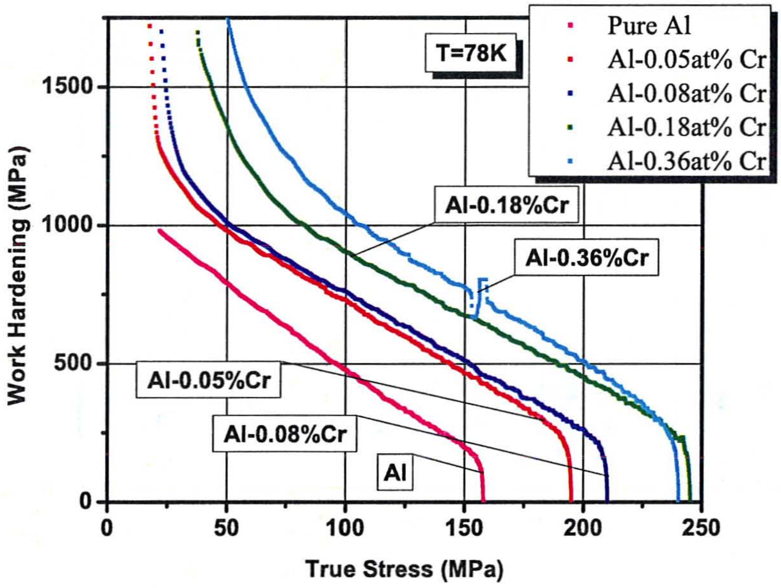

Figure 172: Work Hardening rate vs. True Stress for Non-Recrystallized Al-Cr alloys at 78K

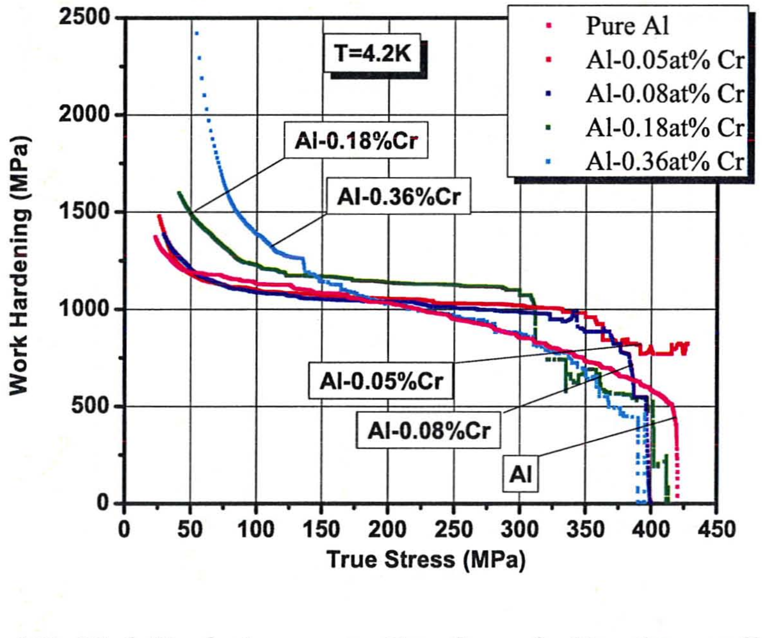

Figure 173: Work Hardening rate vs. True Stress for Non-Recrystallized Al-Cr alloys at 4.2K

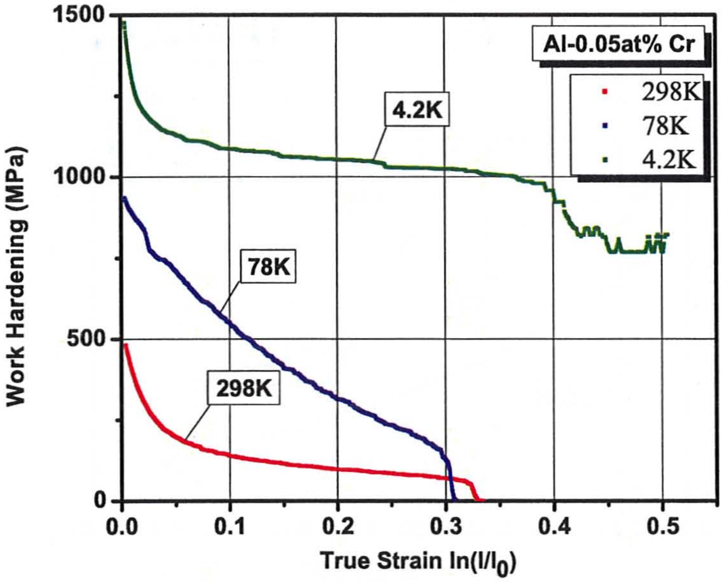

Figure 174: Work Hardening Rate vs. True Strain for Recrystallized Al-0.05at% Cr alloy

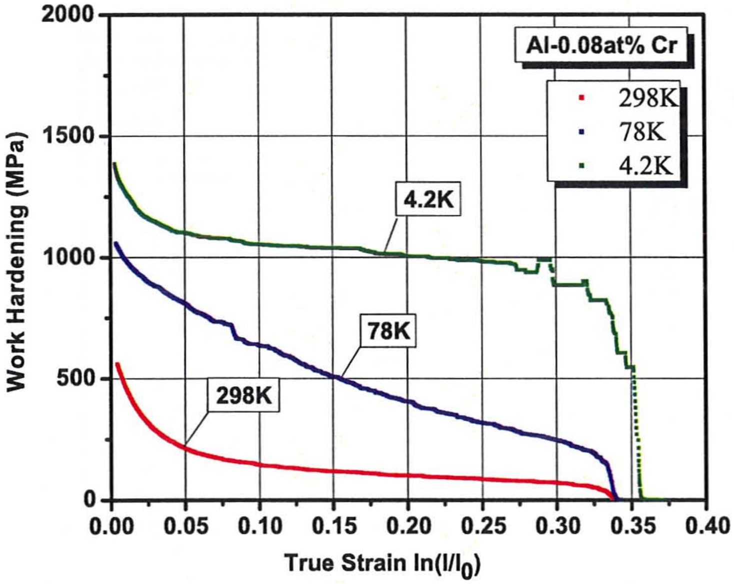

Figure 175: Work Hardening Rate vs. True Strain for Recrystallized Al-0.08at% Cr alloy

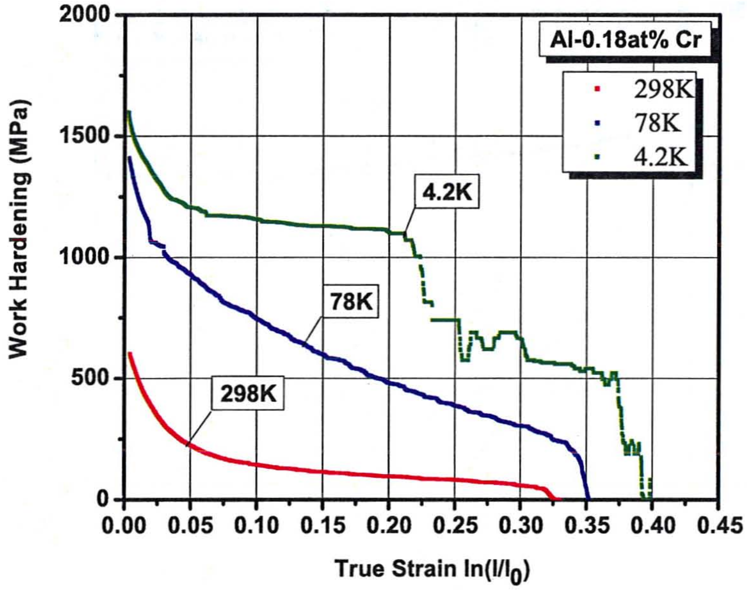

Figure 176: Work Hardening Rate vs. True Strain for Recrystallized Al-0.18at% Cr alloy

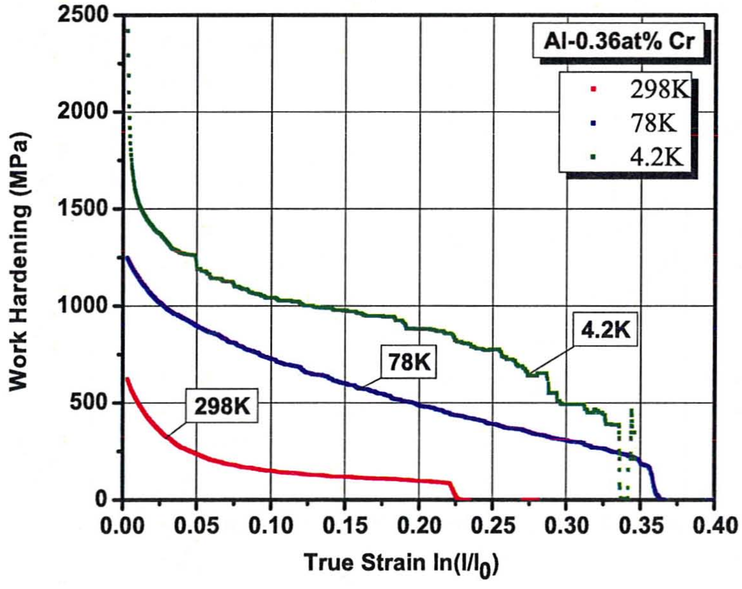

Figure 177: Work Hardening Rate vs. True Strain for Recrystallized Al-0.36at% Cr alloy

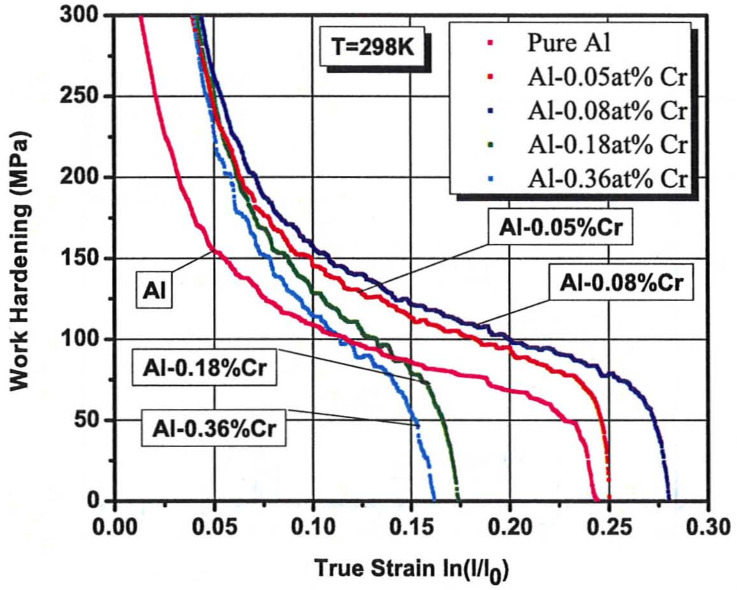

Figure 178: Work Hardening rate vs. True Strain for Recrystallized Al-Cr alloys at 298K

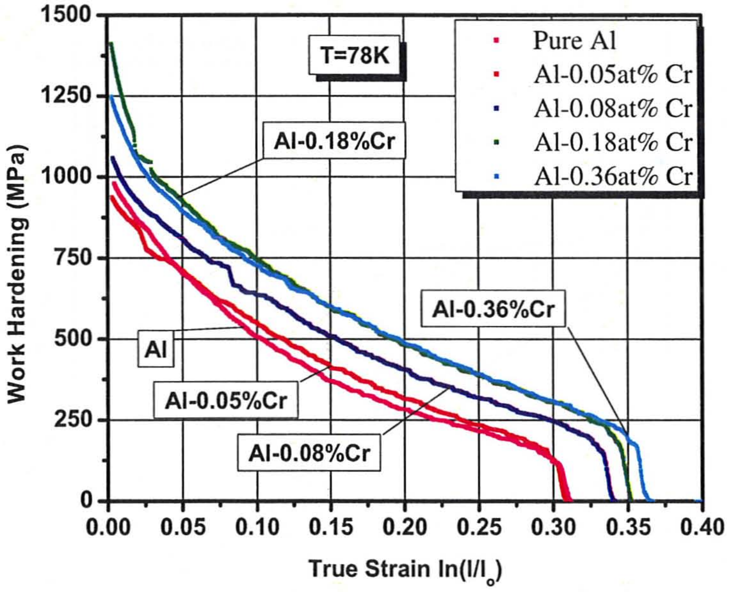

Figure 179: Work Hardening rate vs. True Strain for Recrystallized Al-Cr alloys at 78K

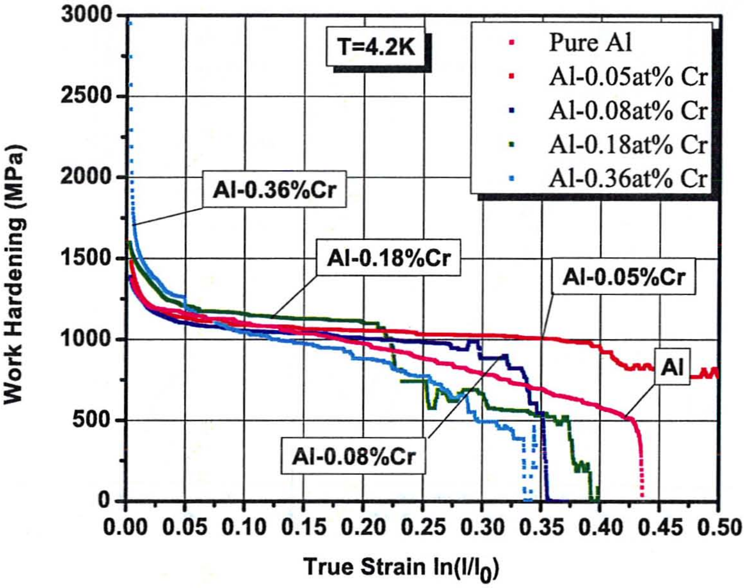

Figure 180: Work Hardening rate vs. True Strain for Recrystallized Al-Cr alloys at 4.2K

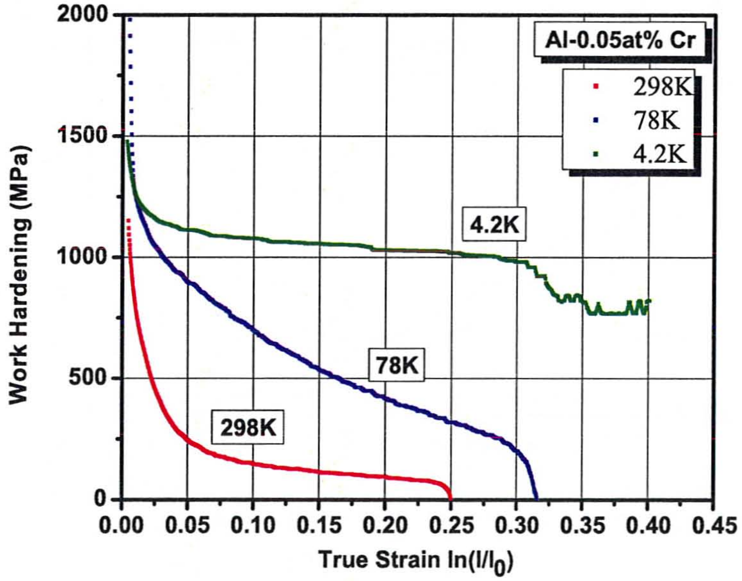

Figure 181: Work Hardening Rate vs. True Strain for Non-Recrystallized Al-0.05at% Cr alloy

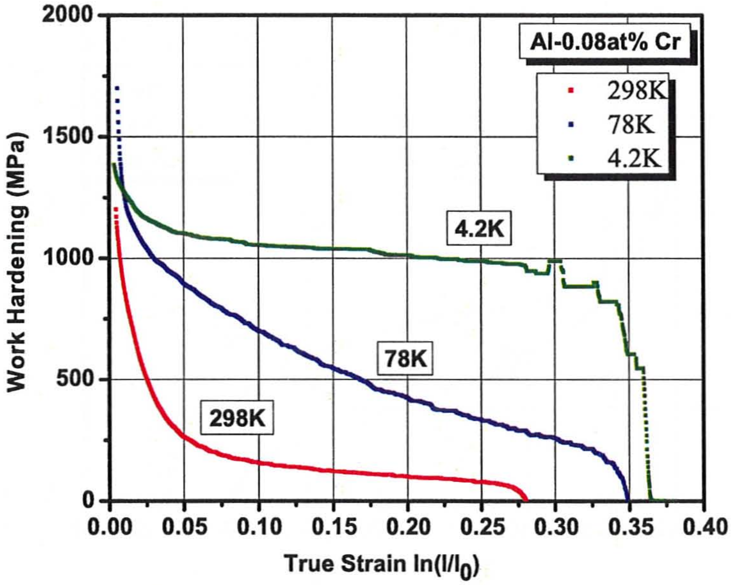

Figure 182: Work Hardening Rate vs. True Strain for Non-Recrystallized Al-0.08at% Cr alloy

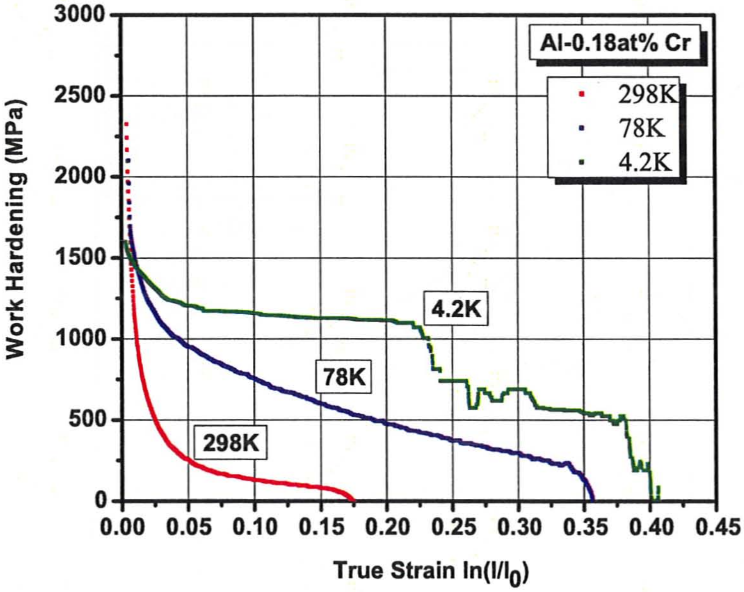

Figure 183: Work Hardening Rate vs. True Strain for Non-Recrystallized Al-0.18at% Cr alloy

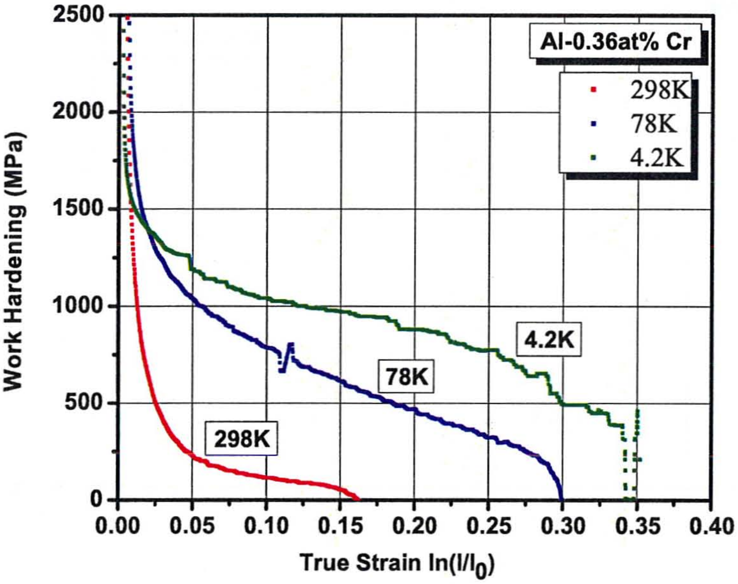

Figure 184: Work Hardening Rate vs. True Strain for Non-Recrystallized Al-0.36at% Cr alloy

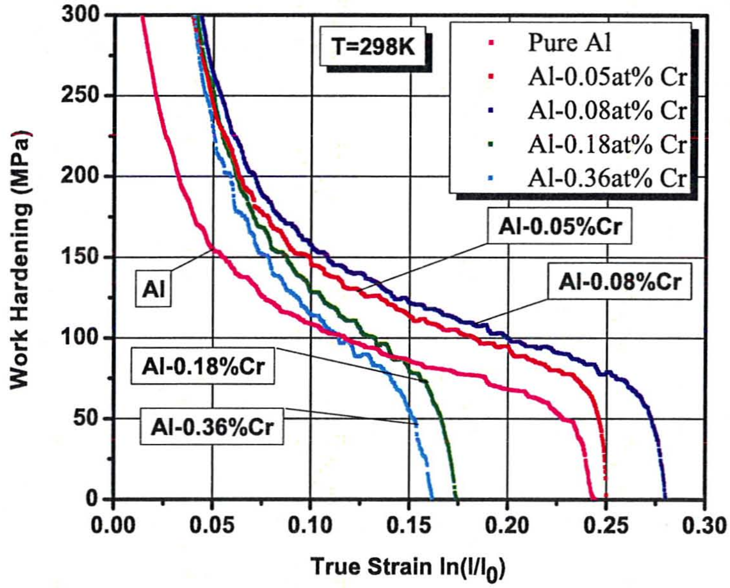

Figure 185: Work Hardening rate vs. True Strain for Non-Recrystallized Al-Cr alloys at 298K

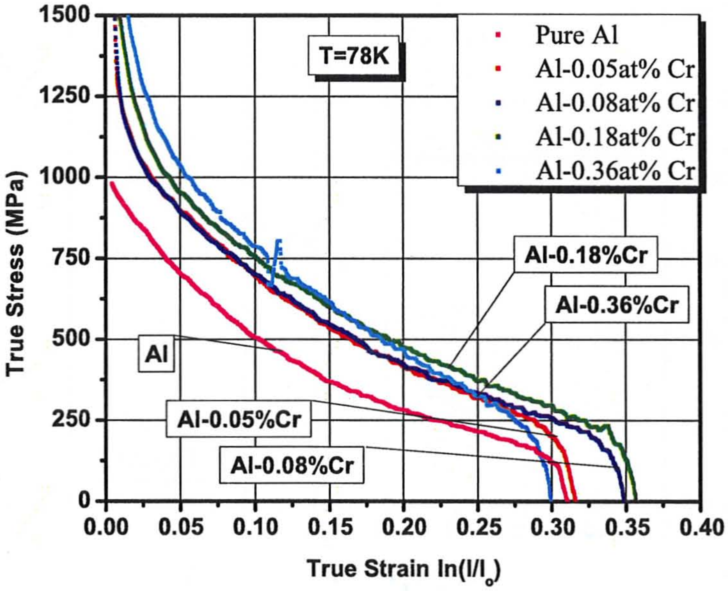

Figure 186: Work Hardening rate vs. True Strain for Non-Recrystallized Al-Cr alloys at 78K

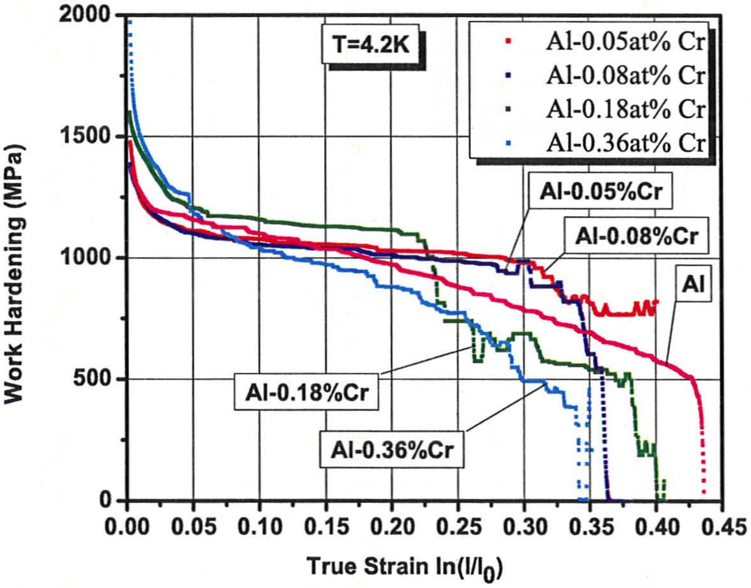

Figure 187: Work Hardening rate vs. True Strain for Non-Recrystallized Al-Cr alloys at 4.2K

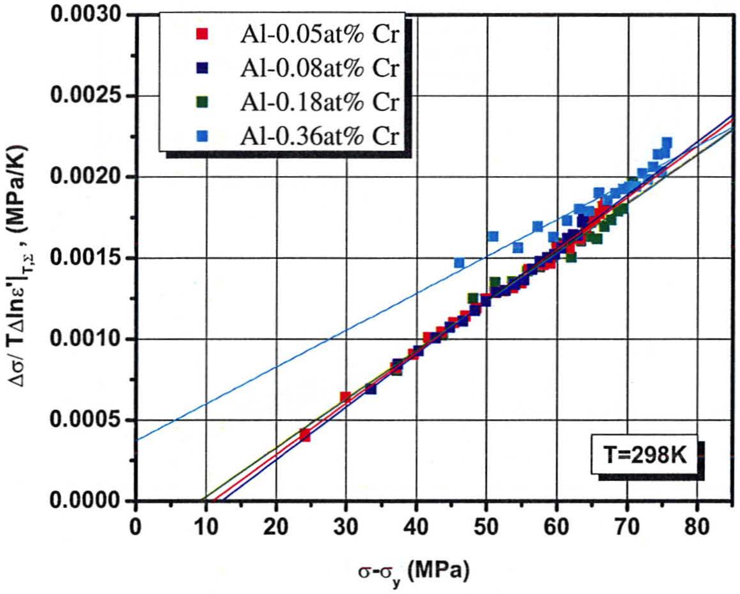

Figure 188: Haasen Plot for Al-Cr Alloys, 298K test

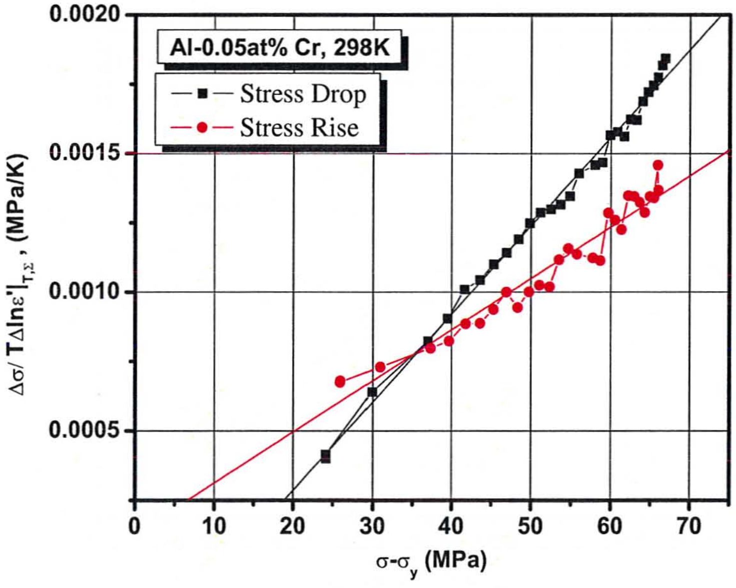

Figure 189: Haasen Plot for Al-0.05at% Cr alloy, 298K test

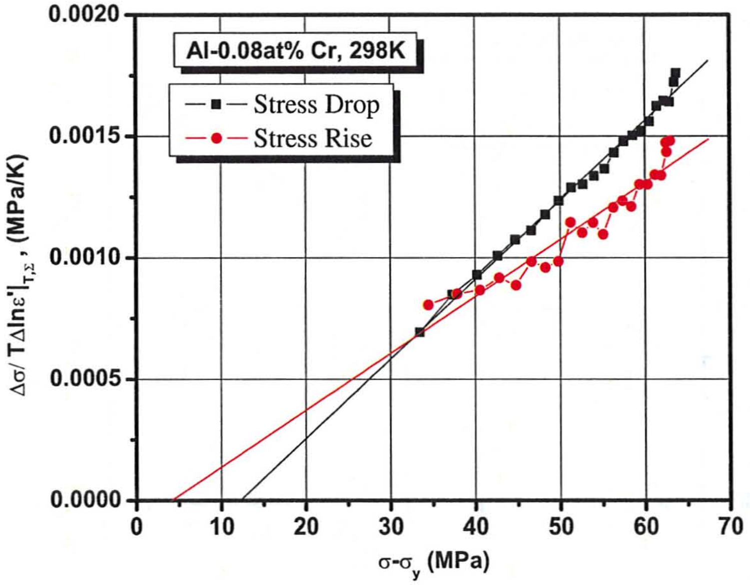

Figure 190: Haasen Plot for Al-0.08at% Cr alloy, 298K test

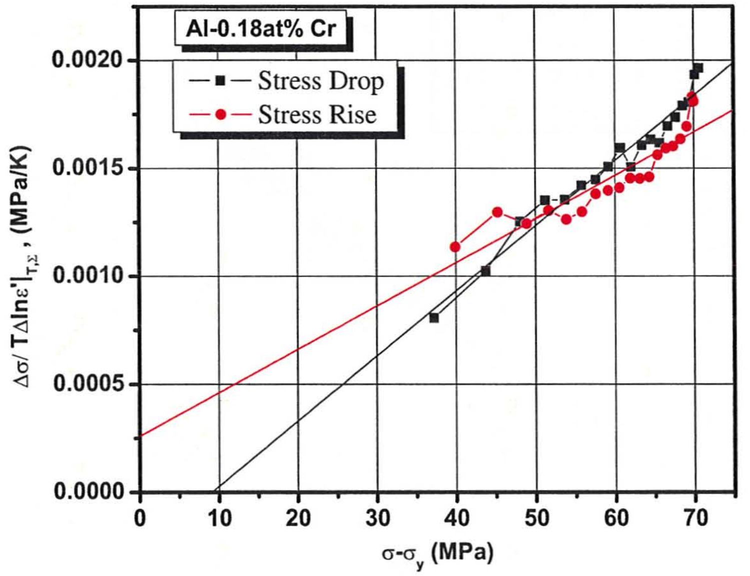

Figure 191: Haasen Plot for Al-0.18at% Cr alloy, 298K test

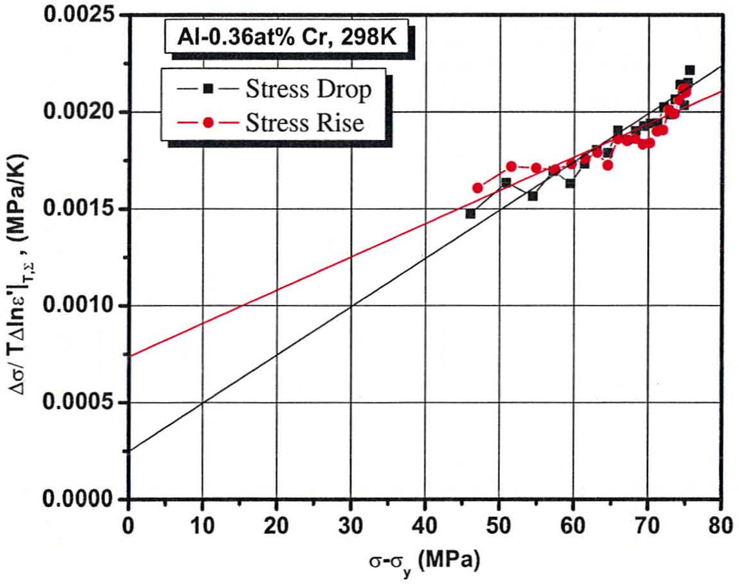

Figure 192: Haasen Plot for Al-0.36at% Cr alloy, 298K test

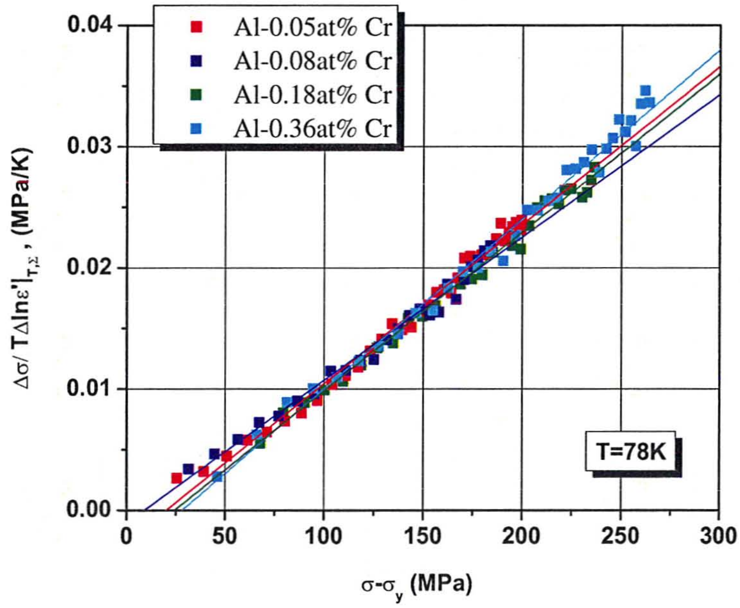

Figure 193: Haasen Plot for Al-Cr Alloys, 78K test

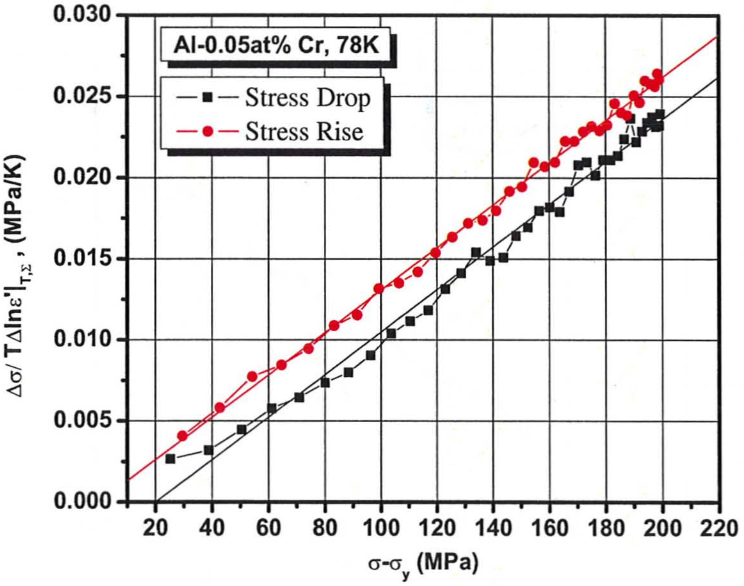

Figure 194: Haasen Plot for Al-0.05at% Cr alloy, 78K test

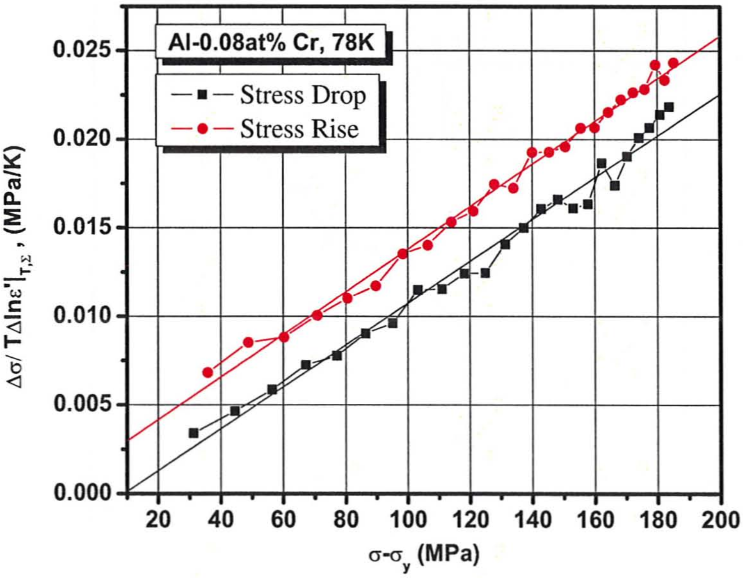

Figure 195: Haasen Plot for Al-0.08at% Cr alloy, 78K test

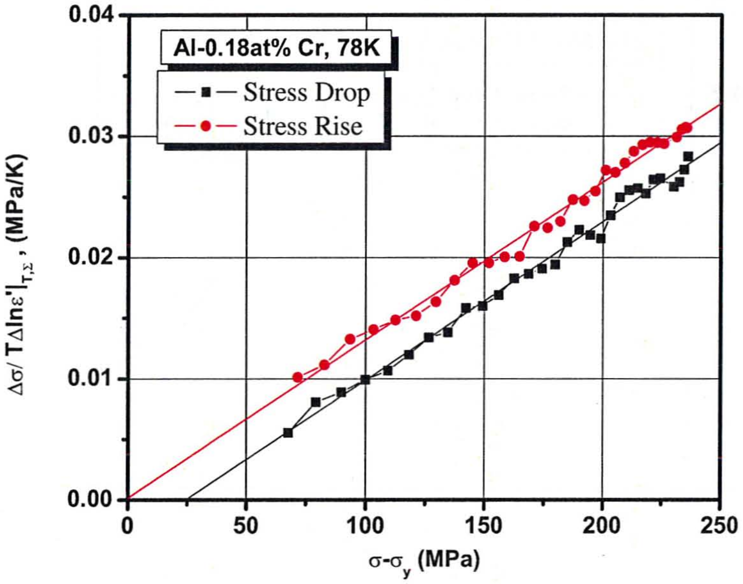

Figure 196: Haasen Plot for Al-0.18at% Cr alloy, 78K test

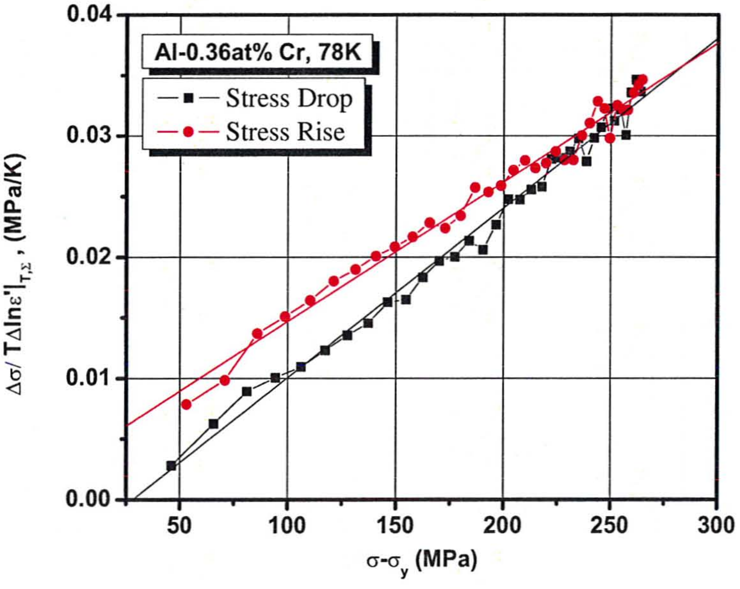

Figure 197: Haasen Plot for Al-0.36at% Cr alloy, 78K test

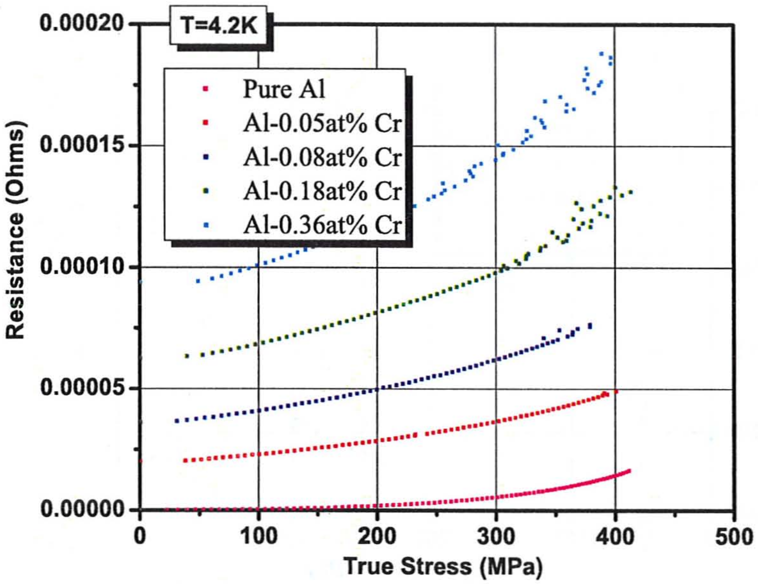

Figure 198: Resistance vs. Stress Data for Recrystallized Al-Cr Alloys

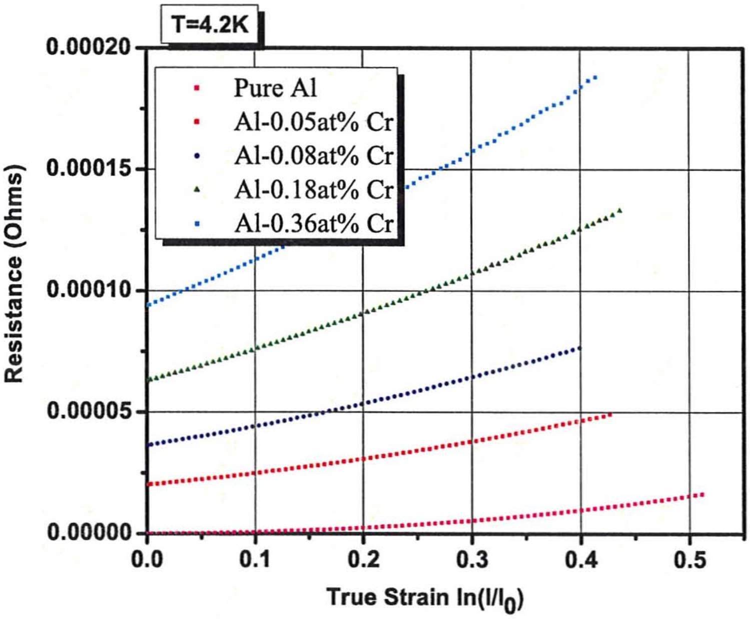

Figure 199: Resistance vs. Strain Data for Recrystallized Al-Cr Alloys

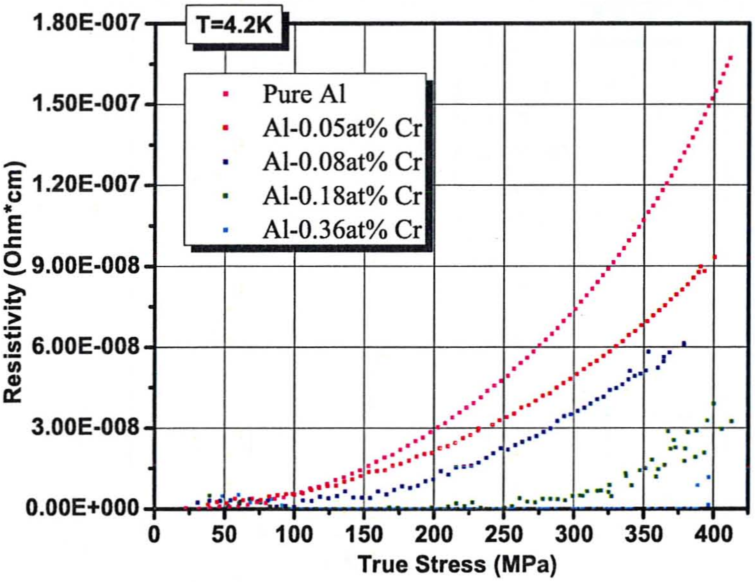

Figure 200: Resistivity vs. Stress Data for Recrystallized Al-Cr Alloys

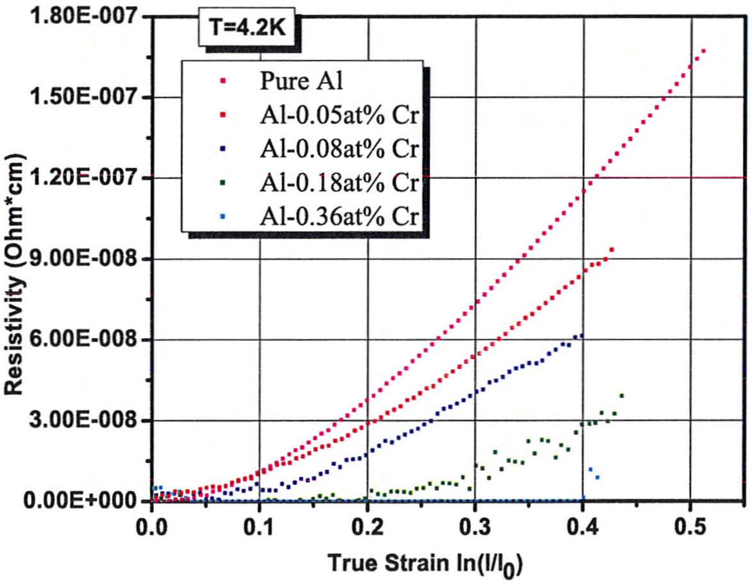

Figure 201: Resistivity vs. Strain Data for Recrystallized Al-Cr Alloys

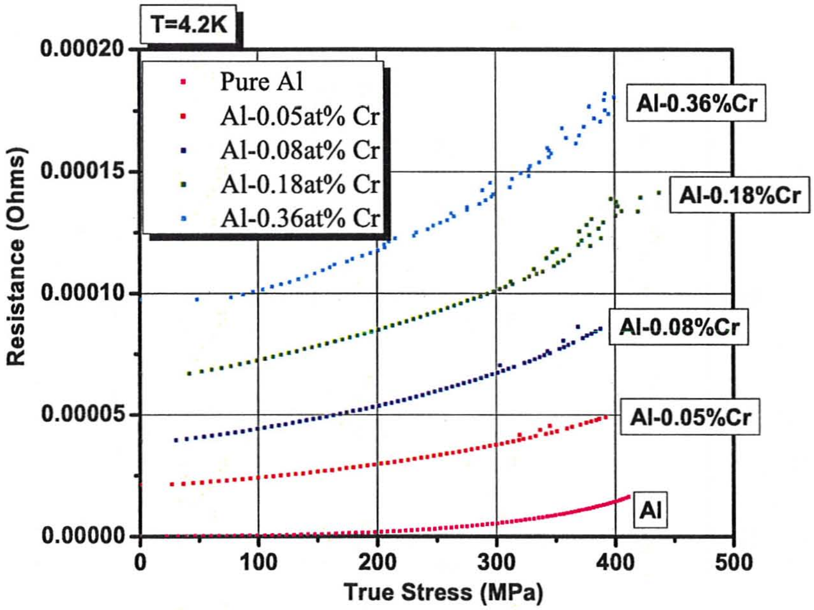

Figure 202: Resistance vs. Stress Data for Non-Recrystallized Al-Cr Alloys

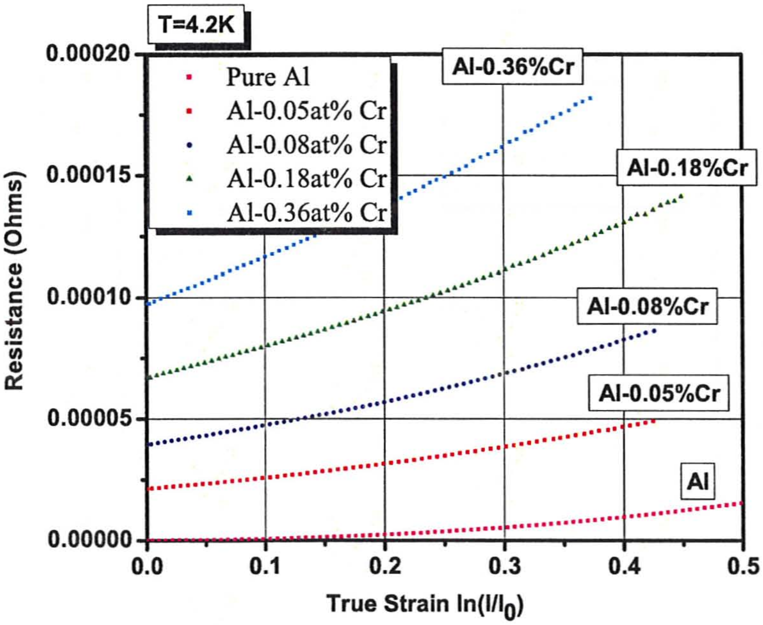

Figure 203: Resistance vs. Strain Data for Non-Recrystallized Al-Cr Alloys

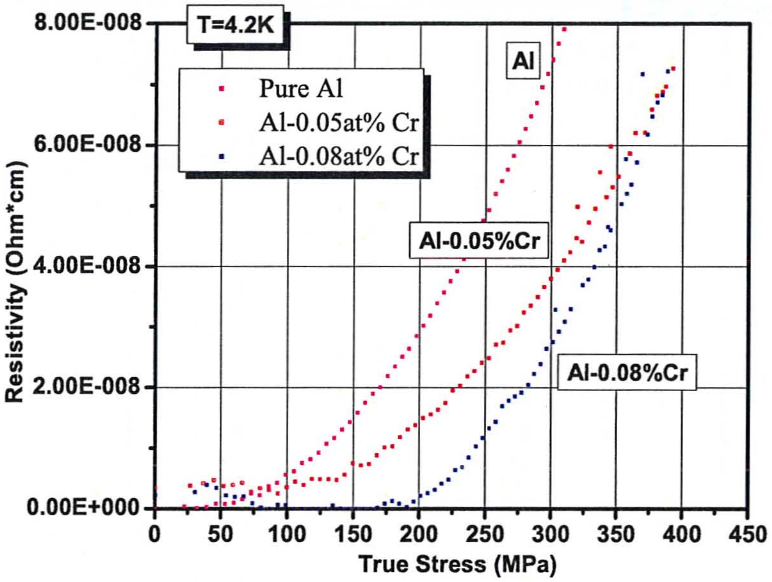

Figure 204: Resistivity vs. Stress Data for Non-Recrystallized Al-Cr Alloys

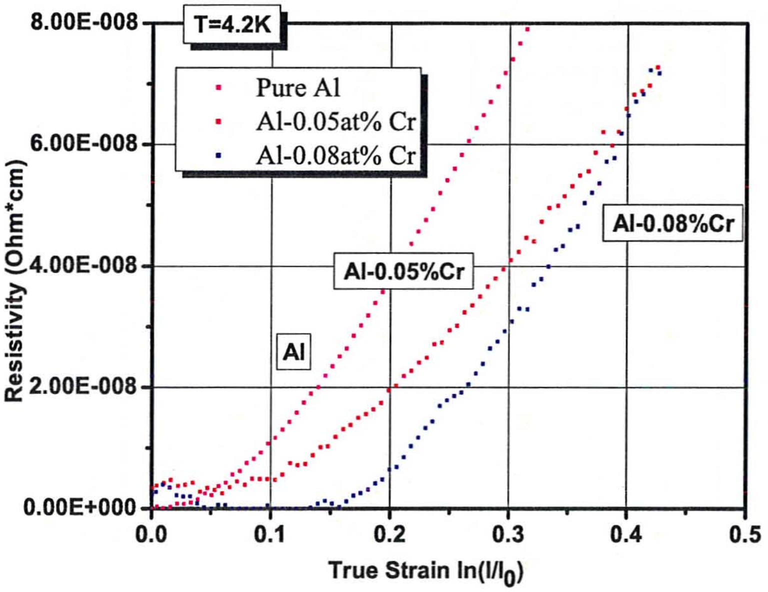

Figure 205: Resistivity vs. Stress Data for Non-Recrystallized Al-Cr Alloys

13120